

5-1-2019

# SIMULATION OF A NOVEL MEDIATED OXYCOMBUSTION SYSTEM

Hussein M. Al Mrayatee

*Southern Illinois University Carbondale*, [husseinxmsm@gmail.com](mailto:husseinxmsm@gmail.com)

Follow this and additional works at: <https://opensiuc.lib.siu.edu/dissertations>

---

## Recommended Citation

Al Mrayatee, Hussein M., "SIMULATION OF A NOVEL MEDIATED OXYCOMBUSTION SYSTEM" (2019). *Dissertations*. 1668.  
<https://opensiuc.lib.siu.edu/dissertations/1668>

This Open Access Dissertation is brought to you for free and open access by the Theses and Dissertations at OpenSIUC. It has been accepted for inclusion in Dissertations by an authorized administrator of OpenSIUC. For more information, please contact [opensiuc@lib.siu.edu](mailto:opensiuc@lib.siu.edu).

SIMULATION OF A NOVEL MEDIATED OXYCOMBUSTION SYSTEM

By

Hussein Mohammed Sadeq Al-Mrayatee

B.Sc., University of Baghdad, Iraq, 2000

M.Sc., University of Baghdad, Iraq, 2003

A Dissertation

Submitted in Partial Fulfillment of the Requirements for the  
Doctor of Philosophy Degree

Department of Mechanical Engineering and Energy Processes  
College of Engineering  
In the Graduate School  
Southern Illinois University Carbondale  
May 2019

DISSERTATION APPROVAL

SIMULATION OF A NOVEL MEDIATED OXYCOMBUSTION SYSTEM

By

Hussein Mohammed Sadeq Al-Mrayatee

A Dissertation Submitted in Partial

Fulfillment of the Requirements

for the Degree of

Doctor of Philosophy

in the field of Engineering Science

Approved by:

Dr. Kanchan Mondal, Chair

Dr. Rasit Koc

Dr. Emmanuel C.Nsofor

Dr. James A. Mathias

Dr. Saikat Talapatra

Graduate School  
Southern Illinois University Carbondale  
March 19, 2019

## AN ABSTRACT OF THE DISSERTATION OF

HUSSEIN MOHAMMED SADEQ AL-MRAYATEE, for the Doctor of Philosophy degree in ENGINEERING SCIENCE, Presented on March 19, 2019, at Southern Illinois University Carbondale.

TITLE: SIMULATION OF A NOVEL MEDIATED OXYCOMBUSTION SYSTEM

MAJOR PROFESSOR: Dr. Kanchan Mondal

Global warming and climate change are serious problems challenging humanity. Therefore, important steps need to be taken to neutralize such a challenge. During the last century, huge amounts of carbon dioxide released into the atmosphere is causing damages to our bio-ecosphere. Technologies such as oxycombustion and chemical looping combustion had been discussed to capture and sequester carbon dioxide at lower cost. Separating air from fuel using chemical looping or separating nitrogen from the air using the oxygen transport membrane (OTM) are the main steps to capture carbon dioxide in a less expensive method. Each technology has its own drawbacks. Therefore, to overcome these drawbacks an integrated system is proposed combining oxycombustion, chemical looping and OTM technologies into one system. This work aimed to model and simulate an integrated system in a single reactor using liquid antimony and antimony trioxide as an oxygen carrier to shuttle the oxygen from the OTM to the fuel. Thermal management and materials transport is achieved using natural circulation arising from density differences between metal and metal oxide. Heat is released inside the reactor due to the exothermic oxidation reaction, and the temperature is found to increase in the absence of a sink. The temperature profile is studied in all the reactor zones with respect to oxidation and the reduction rates, operating temperature, fluid viscosity, and radiation effects. The results show that the system has a good potential to transfer the heat generated from the oxidation to other zones and thus can be used as a boiler.

## ACKNOWLEDGMENTS

I would like to start by expressing my sincere thanks to my advisor, Professor Kanchan Mondal for his guidance, support, and encouragement during the entire course of my doctoral study here at southern Illinois University. In addition to his insightful mentorship in guiding my doctoral research on the right track toward achieving the desired outcomes.

My sincere thanks and appreciation also go to Dr. Rasit Koc, Dr. Emmanuel C.Nsofor, Dr. James Mathias and Dr. Saikat Talapatra for serving in my dissertation committee. In addition to the great knowledge I gained from the graduate courses taught by them, their suggestions during my proposal and dissertation defense were very much valued. Special thanks also go to Dr. Emmanuel C.Nsofor and Dr. James Mathias for serving in my candidacy committee. The time they spent in the assessment and my oral examination is very much appreciated.

## DEDICATION

I dedicate this dissertation to

My mom the reason of what I became today.

My amazing wife with her unconditional love, everyday encouragement and nonstop support.

My children: Yousif and Lamar the joy of my life.

## TABLE OF CONTENTS

| <u>CHAPTER</u>                         | <u>PAGE</u> |
|----------------------------------------|-------------|
| ABSTRACT.....                          | i           |
| ACKNOWLEDGMENTS.....                   | ii          |
| DEDICATION.....                        | iii         |
| LIST OF TABLES.....                    | v           |
| LIST OF FIGURES.....                   | vi          |
| CHAPTERS                               |             |
| CHAPTER 1 – Introduction.....          | 1           |
| CHAPTER 2 – Literature Review .....    | 9           |
| CHAPTER 3 - Mathematical Model.....    | 38          |
| CHAPTER 4 – Result and Discussion..... | 51          |
| CHAPTER 5 – Conclusion .....           | 79          |
| REFERENCES.....                        | 82          |
| APPENDICES                             |             |
| APPENDIX A- NOMENCLATURE.....          | 98          |
| APPENDIX B -UDF.....                   | 101         |
| VITA.....                              | 106         |

## LIST OF TABLES

| <u>TABLE</u>                                                                                    | <u>PAGE</u> |
|-------------------------------------------------------------------------------------------------|-------------|
| Table 3.1: Reactor zones volume.....                                                            | 39          |
| Table 3.2: Material thermo-physical properties.....                                             | 47          |
| Table 3.3: Gas specific heat constant.....                                                      | 47          |
| Table 4.1: Properties of antimony, lead, copper and Iron oxides.....                            | 51          |
| Table 4.2: Sims experimental data.....                                                          | 56          |
| Table 4.3: Simulation data.....                                                                 | 56          |
| Table 4.4: Volumetric and ratio for gas flow.....                                               | 64          |
| Table 4.5: The viscosity values for antimony and antimony trioxide used in the simulations..... | 74          |

## LIST OF FIGURES

| <u>FIGURE</u>                                                                                                                                                                                                              | <u>PAGE</u> |
|----------------------------------------------------------------------------------------------------------------------------------------------------------------------------------------------------------------------------|-------------|
| Figure 1.1: CO <sub>2</sub> capture technologies [7].....                                                                                                                                                                  | 4           |
| Figure 1.2: Chemical looping process.....                                                                                                                                                                                  | 5           |
| Figure 2.1: Ceramic membrane types (a) electrodes (b-i) single-phase (b-ii) dual-phase [18].....                                                                                                                           | 9           |
| Figure 2.2: Schematic of oxygen permeation across the MIEC membranes [26].....                                                                                                                                             | 12          |
| Figure 2.3: Ideal fluorite structure [35].....                                                                                                                                                                             | 13          |
| Figure 2.4: The structure of perovskite ABO <sub>3</sub> . (a) corner-sharing (BO <sub>6</sub> ) octahedral with<br>A ions located in 12-coordinated interstices. (b) B-site cation at the center of<br>the cell [37]..... | 14          |
| Figure 2.5: Schematic of membrane for oxygen separation in oxyfuel processes using<br>(a) three- end concept (b) four-end concept [72].....                                                                                | 25          |
| Figure 2.6: AZEP cycle work package [77].....                                                                                                                                                                              | 26          |
| Figure 2.7: ZEITMOP power cycle with separate combustion and ITM reactor [80].....                                                                                                                                         | 27          |
| Figure 2.8: Comparison among tradition oxygen carrier [102].....                                                                                                                                                           | 32          |
| Figure 3.1: Reactor schematic diagram.....                                                                                                                                                                                 | 39          |
| Figure 3.2: Effect of grid size on (a) net gas temperature (b) net liquid temperature verses<br>reaction time.....                                                                                                         | 49          |
| Figure 3.3: Effect of time step on (a) net gas temperature (b) net liquid temperature verses<br>reaction time.....                                                                                                         | 50          |
| Figure 4.1: Gibbs free energy with operation temperature (a) oxidation (b) reduction.....                                                                                                                                  | 52          |
| Figure 4.2: Enthalpy of reaction with operation temperature (a) oxidation reaction (b)<br>reduction reaction.....                                                                                                          | 53          |

|                                                                                                                                                        |    |
|--------------------------------------------------------------------------------------------------------------------------------------------------------|----|
| Figure 4.3: Lead and lead oxide oxidation and reduction (a) Gibbs free energy (b) enthalpy of reaction with wide operation temperature.....            | 54 |
| Figure 4.4: Antimony and antimony trioxide oxidation and reduction (a) Gibbs free energy (b) enthalpy of reaction with wide operation temperature..... | 55 |
| Figure 4.5: Energy balance for antimony and antimony trioxide reaction .....                                                                           | 55 |
| Figure 4.6: Temperature distribution of gas and liquid phases in each reactor zone<br>Sims case (a) gas phase (b) liquid phase .....                   | 57 |
| Figure 4.7: Temperature contour of gas and liquid phases in the reactor zones based on experimentally validated case .....                             | 58 |
| Figure 4.8: Sb and Sb <sub>2</sub> O <sub>3</sub> molar concentration with respect to time .....                                                       | 59 |
| Figure 4.9: Gas and liquid volume fraction with respect to time .....                                                                                  | 60 |
| Figure 4.10: O <sub>2</sub> and CH <sub>4</sub> mass fraction distribution with respect to time .....                                                  | 61 |
| Figure 4.11: CO <sub>2</sub> and H <sub>2</sub> O mass fraction distribution with respect to time .....                                                | 62 |
| Figure 4.12: H <sub>2</sub> O mole value in each zone with respect to time .....                                                                       | 62 |
| Figure 4.13: Temperature distribution of gas and liquid phases in each reactor zone<br>Case1 at 950K temperature (a) gas phase (b) liquid phase .....  | 65 |
| Figure 4.14: Temperature distribution of gas and liquid phases in each reactor zone<br>Case2 at 950K temperature (a) gas phase (b) liquid phase .....  | 65 |
| Figure 4.15: Temperature distribution of gas and liquid phases in each reactor zone<br>Case 3 at 950K temperature (a) gas phase (b) liquid phase ..... | 66 |
| Figure 4.16: Temperature contour of gas and liquid of reactor zones case1 at 950K .....                                                                | 67 |
| Figure 4.17: Temperature contour of gas and liquid of reactor zones case2 at 950K .....                                                                | 67 |
| Figure 4.18: Temperature contour of gas and liquid of reactor zones case3 at 950K .....                                                                | 68 |

|                                                                                                                             |    |
|-----------------------------------------------------------------------------------------------------------------------------|----|
| Figure 4.19: The net gas and liquid temperature comparison for all simulated cases at 950K.....                             | 68 |
| Figure 4.20: The net gas and liquid temperature comparison for all simulated cases at 950K .....                            | 69 |
| Figure 4.21: Temperature distribution for each reactor zone case1 (a) liquid phase                                          |    |
| (b) gas phase.....                                                                                                          | 69 |
| Figure 4.22: The concentration ratio of Sb and Sb <sub>2</sub> O <sub>3</sub> inside the reactor during reaction time ..... | 70 |
| Figure 4.23: The temperature distribution predation in each zone inside the reactor for                                     |    |
| different operation temperature.....                                                                                        | 72 |
| Figure 4.24: The temperature distribution predation in each zone inside the reactor for                                     |    |
| different operation temperature Sims case .....                                                                             | 73 |
| Figure 4.25: The effect of viscosity on temperature profile of reactor .....                                                | 76 |
| Figure 4.26: Radiation effect in each reactor zone with different operation                                                 |    |
| temperature Case3.....                                                                                                      | 78 |

# CHAPTER 1

## INTRODUCTION

### 1.1 Background

The environmental impact of energy consumption is an important issue challenging our existence. Global warming and climate change have direct impact on our lives and other creatures that share the same planet with us. Excessive use of fossil fuel has released huge amounts of carbon dioxide, carbon monoxide and other harmful gases related to fossil fuels combustion into the atmosphere. Many solutions were proposed and tested to reduce greenhouse gases emissions, but each of them needs extensive studies and revision. Renewable energy such as wind, biofuel, solar and hydropower are attractive energy sources due to availability and environment friendly nature. However, the lower efficiency achieved and storage issues are the main drawbacks in the utilization of such resources. Extensive research needs to be conducted to improve the harvest and storage of such energy resources. Only about 10% of our current energy production comes from renewable resources. Another 8% comes from nuclear power, but due to operational safety and waste disposal concern the usage of such technology is limited. The bulk of energy production is still dependent on fossil fuels such as petroleum, natural gas and coal. Meanwhile, the fossil fuel sector employs millions of people and many countries around the world depend on such fuel to support the economy.

The best approach to overcome the environmental crisis and provide energy is to be more efficient utilizing of traditional carbon-based fuels by cleaner and more sustainable methods. As mentioned earlier, global warming issues due to the release of CO<sub>2</sub> during fossil fuel-driven electricity generation is becoming a major issue. Thus, for continued utilization of carbon-based fuels three approaches are generally considered. The first approach involves increasing the

efficiency of traditional power cycles by moving from subcritical conditions to supercritical conditions. Research has shown that based on the current efficiencies, the carbon dioxide emissions can be reduced by 30 % if the cycle efficiency is improved from 39 % at subcritical conditions to over 50 % in advanced supercritical conditions. The second approach is the pre-combustion separation enabled by gasification technologies. The resulting power cycle is a combined cycle with a topping Brayton cycle- based moist hydrogen driven gas turbine system with a bottoming Rankine cycle driven by steam generated through heat recovery from various exothermic unit operations. The last option is the post combustion/utilization carbon capture. Traditional post combustion carbon capture is inefficient, since the CO<sub>2</sub> content ranges from 9 to 15 % in a flue gas primarily composed of nitrogen. The nitrogen in the fuel and air also forms nitrous oxide which have to be removed. There are several solvents and sorbents which have been studied to enable post combustion carbon capture. The materials are more efficient when the CO<sub>2</sub> content in the flue gas is high. Thus, to improve the CO<sub>2</sub> content in the post utilization gaseous stream, advanced technologies such as oxycombustion, chemical looping combustion, and direct carbon fuel cells have been developed. In oxycombustion, oxygen is first separated from air and the fossil fuel is burnt in oxygen, thereby producing only CO<sub>2</sub> and H<sub>2</sub>O. Part of the produced CO<sub>2</sub> is recycled to dilute the oxygen but not the flue gas. In chemical looping combustion, a metal oxide is used to deliver the oxygen obviating the need for direct interaction of the fuel with air. The reduced metal oxide is then re-oxidized in air. The resultant gaseous streams are separate streams of high CO<sub>2</sub> containing flue gas and oxygen- depleted air. In direct carbon fuel cells an oxygen ion transporting membrane is used as a separator for nitrogen and oxygen. The transported oxygen ion then directly or indirectly electrochemically reacts with the carbon at the anode while a traditional cathode is used for the oxygen reduction reaction.

We have designed a new system that integrates the advantages of the above three post combustion capture technologies while mitigating the technical barriers for each. In this work, fuel is combusted by a metal oxide as in a chemical looping and the reduced metal oxide is oxidized by oxygen (and not air) as in oxycombustion and the oxygen for this operation is obtained by separation from air using an oxygen transport membrane often employed in solid oxide fuel cells. Using an integration of different technologies into one is novel and the simulation of this system is the creative input that will assist in the design of the combustion system and the thermal management aspects.

## **1.2 CO<sub>2</sub> capture technologies**

Carbon dioxide concentration in the atmosphere has been growing rapidly in the last decade. In 2013, CO<sub>2</sub> levels reached 400 ppm for the first time in recorded history. Therefore massive cuts in CO<sub>2</sub> emission are necessary to stop global warming and climate change [1]. Carbon dioxide is produced in the power generation, transportation and industry sectors. Nearly 10 billion tons of CO<sub>2</sub> per year are released from power generation [2]. Capture and sequestering such amount will help to reduce the emission of greenhouse gases. CO<sub>2</sub> can be sequestered in geological formations, in the ocean and or as mineral carbonates. It may also be used for the industrial processes. In general, there are three main technologies to capture CO<sub>2</sub> during energy production: post-combustion, pre-combustion and oxy-fuel combustion as shown in figure (1.1).

The post-combustion process starts after the complete combustion of fuel, where flue gases product is being purified from particulate matter, NO<sub>x</sub> and SO<sub>x</sub>. Many CO<sub>2</sub> capture technologies are being investigated including chemical absorption, adsorption and membrane separation. The most commonly used method commercially is chemical absorption where the

flue gases cooled and fed to the absorber where an amine solvent is employed to absorb CO<sub>2</sub>. Then, the highly concentrated CO<sub>2</sub> amino is regenerated in the stripper under high temperature to recover the CO<sub>2</sub> at low pressure [3, 4]. The post-combustion process has a high energy penalty, which is 8% and 6% for the coal and gas fired power plant respectively [5].

The pre-combustion is mainly applicable to coal-gasification plants, specifically integrated gasification combined cycle (IGCC). In the gasifier coal, is introduced to produce syngas at high temperature and pressure. The raw product contains pollutant particles such as mercury, H<sub>2</sub>S and COS which need to be removed. After pollutants are removed the product mainly contains CO and H<sub>2</sub> where CO is converted to CO<sub>2</sub> through steam reforming. H<sub>2</sub> enters the combustion chamber after CO<sub>2</sub> is removed. This process has a lower cost compared to the post-combustion technology [6].

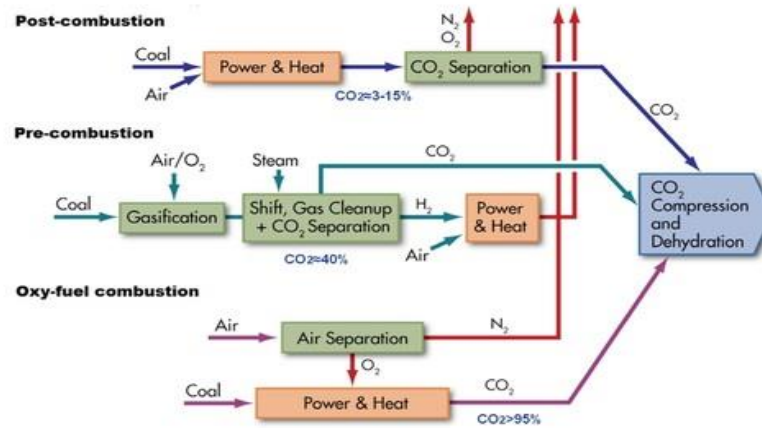


**Figure (1.1)** CO<sub>2</sub> capture technologies [7]

Oxy-fuel combustion, where fossil fuel is burned in nearly pure oxygen to produce flue gas with high CO<sub>2</sub> and H<sub>2</sub>O concentration, where it can be separated easily. This is a nitrogen free process, which prevents NO<sub>x</sub> emissions. The energy penalty is huge because oxygen supplied to the combustion chamber is produced by the cryogenic air separation process, which has a high energy consumption. The oxycombustion is promising technology if oxygen

separation can be achieved at a lower cost. Research on membrane based air separation is ongoing to achieve lowered separation costs.

Chemical looping combustion (CLC) is another concept used to capture CO<sub>2</sub> through the separation air and fuel using intermediate oxygen carrier. Air oxidize the oxygen carrier in the air reactor and then the oxygen carrier reduces to its original state inside the fuel reactor as shown in figure (1.2). Many metals, such as Ni, Fe, Mn, Cu and Mo, and their oxides were tested and explored as potential materials to serve as an oxygen carrier. One of the constraints on this technology is the risk of the agglomeration of solid oxygen carrier particles at higher temperatures. The agglomeration reduces the available specific surface resulting in a lowered observed reaction rate between the oxygen carrier and solid fuel. In addition, hot solids handling between the air and fuel reactor is complicated. Therefore, the liquid metal oxide was suggested as an oxygen carrier. Researchers studied the potential for the liquid oxygen carriers for liquid chemical looping combustion technology (LCLC). The results indicate that Pb, Cu and Sb oxides had the potential due to lower operation temperature and a good oxygen carrier [8].

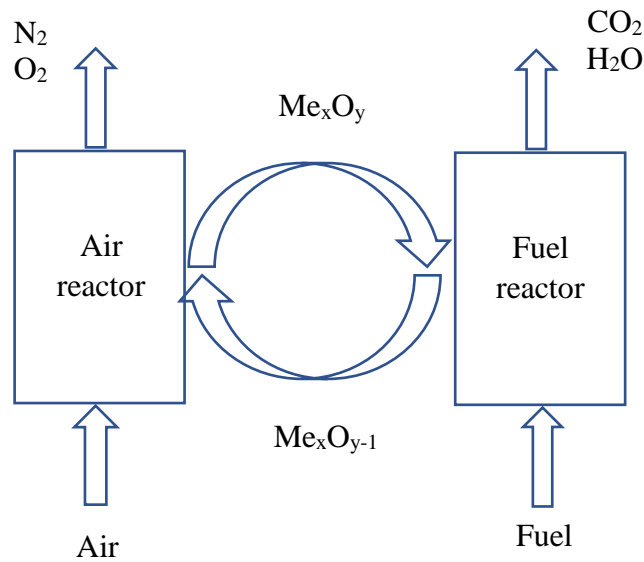


**Figure (1.2)** Chemical looping process

### **1.3 Project description**

The novel mediated oxycombustion system results from the integration of three technologies, namely oxycombustion, oxygen transport membrane (OTM) and LCLC in one reactor to overcome the limitations and cons of the individual system. Researchers have studied each system individually without combining the three systems. Integration of the three system in to one is of significance and the originality of this study. This system is proposed only by Dr. Mondal. He proposed a single reactor is used instead of two sperate reactors. using the chemical looping technology as an oxygen pickup and release mechanism from oxygen transport membrane (OTM) oxidizes the fuel. Oxygen is picked up in oxidation process where the metal is oxidized and then released to combust the fuel while reducing the metal oxide to metal[10]. Heat will be generated due to the exothermic nature for the oxidation process and the only products from fuel reduction will be carbon dioxide and water vaper. Sims [11] conducted the sub-system analysis and system integration experimentally. In this research, data from the experimental study is used to simulate the single reactor mediated oxycombustion process using ANSYS FLUENT. This study seeks to understand the system performance by evaluating the temperature distribution in the reactor with different parameters variation such as oxidation rate, reduction rate, operation temperature, liquid metal viscosity and radiation effect as well as the distribution of the products. The importance of the temperature distribution will help to optimize and design the single reactor, where we can set the heat utility equipment to extract the heat generated.

### **1.4 Motivation**

The global economic growth for the countries will put more pressure on the environment, researchers linked the national income growth with pollution and the amount of greenhouse gases emission. According to the environmental Kuznets curve (EKC), the pollution level is

higher in the early stages of development, but then pollution levels will decrease when a certain level of development has been reached, this will happen only if the societies are willing to pay for improving the quality of the environment [12]. All the facts on the ground proved that societies are not willing to pay their share to improve environmental quality with all income increase. Since the industrial revolution began about 1750, carbon dioxide levels have increased nearly 38 percent as of 2009 and methane levels have increased 148 percent, which is warming up the earth average surface temperature. Global efforts need to be made to decrease the anthropogenic greenhouse gas emissions, mainly CO<sub>2</sub> emission, and for the foreseeable future, coupling fossil fuel conversion systems with economical CO<sub>2</sub> capture and sequestration until the technologies of zero emission CO<sub>2</sub> is obtainable and applicable. The cost of CO<sub>2</sub> management that includes separation, transportation and safe sequestration from flue gases is energy intensive, therefore a process that can reduce the energy penalty will be pivotal in CO<sub>2</sub> management process [3, 13, 14].

The importance of this study is to achieve lower cost CO<sub>2</sub> separation and overcome the typical issues in the current technologies. Burning fossil fuel with pure oxygen will prevent NO<sub>x</sub> formation and easily separate the product of combustion because it is mainly CO<sub>2</sub> and H<sub>2</sub>O, in addition lower the cost of oxygen separation of integrating OTM to the system. The use of an oxygen mediator (metal-metal oxide) enhances the thermal management within the same reactor and decreases the issues of high concentrations of carbonic acids. A simulation model of the proposed system will give the advantage to optimize the system and study different effects on the total temperature and energy released from the system.

### **1.5 Significance of the Study**

The innovation in this project is the simulation of two heterogeneous reactions, oxidation and reduction in single reactant using LCLC technology as oxygen pickup and release mediate. While there have been simulations on CLCs, there had not been any study in liquid metal based CLCs. Moreover, since the design is unique, no studies have been conducted on this system. The unique properties of antimony and antimony oxides give it advantages on other materials: properties such as low melting points and density shows great potential to overcome the common problems of handling liquid metal. Integrating oxycombustion, OTM and LCLC system will mitigate the cost of CO<sub>2</sub> separation in energy production and reduce the energy penalty. The result from this study would be beneficial to study and optimize the system proposed by increasing the energy released and improve the thermal management. The results obtained from this study will enable us to identify proper locations for the steam tubes generation.

## CHAPTER 2

### LITERATURE REVIEW

#### 2.1 Ceramic-based oxygen transport membranes

The demand for pure oxygen in different industrial processes, such as power generation and chemical industry sectors has increased in the last few decades. Therefore, an efficient method needs to be found to replace the cryogenic distillation method, which is very energy intensive and old. Another method that has been used to produce oxygen is the pressure swing adsorption technique which is limited to oxygen purity of 95%. The use of a polymeric membrane is another method. However, due to very small kinetic diameters between nitrogen and oxygen, their separation in polymeric membranes is difficult [15-17]. The ceramic membranes, on the other hand, have the potential to produce high oxygen purity and to operate continuously over long periods with lower energy consumption and result in lower total cost.

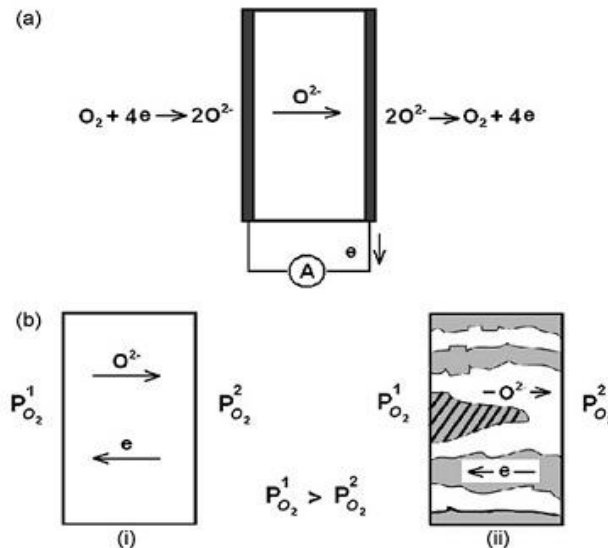


**Figure (2.1)** ceramic membrane types (a) electrodes (b-i) single-phase (b-ii) dual-phase [18]

Ceramic membrane types can be classified based on conduction mechanism: ionic (figure (2.1a)) and mixed ionic-electronic (figure (2.1b)). Mixed ionic electronic with a single phase membrane or a dual-phase membrane, requires no electrodes to operate and transport can be

achieved by the partial pressure gradient applied on both sides of the membrane as shown in figure (2.1b-i,ii) [18].

Different crystal structures, such as fluorite and perovskite, have been investigated for oxygen permeation in the past 30 years. These structures exhibit good oxygen permeation and good chemical stability compared to other structures. Other crystal structures such as Pyrochlore ( $A_2B_2O_7$ ), Brownmillerite ( $A_2B_2O_5$ ),  $Sr_4Fe_{6-x}Co_xO_{13}$  compound, Ruddlesden-Popper series ( $A_{n+1}B_nO_{3n+1}$ ) and Orthorhombic  $K_2NiF_4$ -type structure materials have also been studied. The last two types are also classified into the perovskite structure due to similar in growth microstructure. These crystal structures are promising conducting materials to show good oxygen permeation and structure stability, but require further investigations [18].

The oxygen permeation through these membranes depends on structural defects, which can occur internally or externally by interaction with the environment and the effect of impurities. In order to improve ionic conductivity, a higher concentration of anion vacancies or interstitial cations is required. This is achieved through partial substitution of ions of similar size but different valence numbers. For instance, oxygen vacancies in  $LaBO_3$  oxide can be formed as a result of the partial replacement of some  $La^{+3}$  ions by  $Sr^{+4}$  in  $La_{1-x}Sr_xBO_{3-\delta}$  [7]. Oxygen ions can be released from crystal structure lattice through a gradient in oxygen chemical potential by hopping mechanism when sufficient thermal energy is provided to overcome the energy barriers [18].

Metal oxides might show ionic conductivity due to the high concentration of oxygen vacancies or electronic conductivity due to the mixed-valence state. Electronic conductivity can be either n-type or p-type conductors, depending on material properties and oxygen/metal deficiency in the crystal structure. The n-type electron conductor is generated by the deficiency

of oxygen with excess metals, while the p-type electron holes (positive electronic defects) generated by the deficiency of metal with excess oxygen. The conductivity of an inorganic compound depends upon the products of their defect compound concentration, charge and, mobility, which, in turn, are affected by temperature and oxygen partial pressure [18, 19].

To prepare ceramic-based membranes, different technologies such as the conventional powder method, co-precipitation, sol-gel techniques, hydrothermal and spray and freezing drying have been developed and investigated [20-24]. Identical metal oxides prepared by different technologies have been reported to exhibit different oxygen permeation flux when operated under the same conditions. This occurs due to differences in microstructure obtained by each technology. The microstructure such as surface area, porosity and the grain size affect the physical and chemical properties of the ceramic membranes. Increasing the grain size enhances the ionic conductivity due to a decrease in interstitial boundaries. On the other hand, greater structural stability at higher temperature is achieved at smaller grain sizes, resulting in higher overall conductivity. The grain size distribution is often controlled by the sintering temperature applied in each technology [25].

In general, the oxygen permeation process through the mixed ionic-electronic membrane (MIEC) as shown in figure (2.2) includes the following five steps: I) oxygen molecular diffusion from the gas to the membrane surface. II) the reaction between the molecular oxygen ( $O_2$ ) and vacancy ( $V_O^{\bullet\bullet}$ ) on the oxygen higher concentration membrane surface, where the oxygen gas reduced to oxygen ions ( $O_O^x$ ) and electron holes ( $h^\bullet$ ). III) bulk diffusion of oxygen ion or vacancy through the membrane surface to the oxygen lean side membrane surface driven by the oxygen partial pressure gradient across the membrane. IV) reaction between the lattice oxygen and electron-hole to recombine to form molecular oxygen happened on the membrane surface;

and finally, V) mass transfer of oxygen from the membrane surface to the gas. Both molecular oxygen diffusion from the gas to the membrane and from the membrane to gas can be neglected. because the resistance in both steps is very small compared to the other steps. The bulk diffusion is generally the limiting step when the membrane thickness is increased, while oxygen surface reaction is the limiting step when membrane thickness is decreased [26, 27].

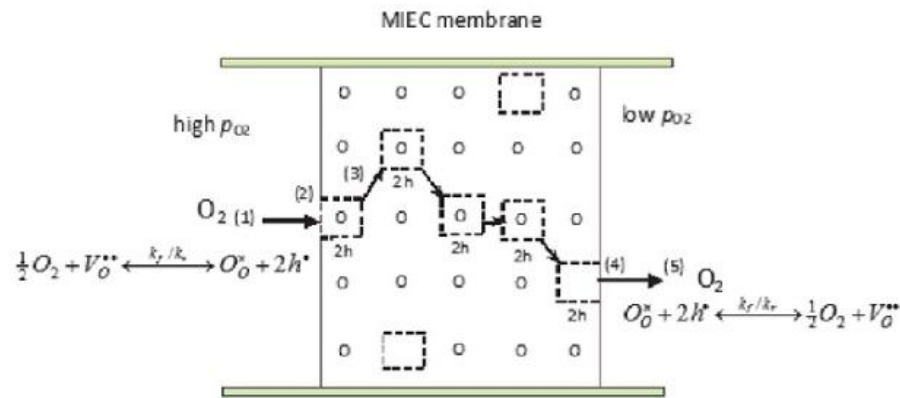


**Figure (2.2)** schematic of oxygen permeation across the MIEC membranes [26]

The oxygen permeation flux can be described by Wagner equation, which shows that the oxygen flux is a function of both ionic and electronic conductivity, thickness and pressure gradient on both sides of the membrane [28].

$$J_{O_2} = \frac{R^{-1}T}{4^2 F^2 L} \int_{P_{O_2}''}^{P_{O_2}'} \frac{\sigma_i \cdot \sigma_e}{(\sigma_i + \sigma_e)} d \ln P_{O_2} \quad (2.1)$$

Fluorite oxide cubic crystal structures (figure (2.3)) such as ceria, bismuth oxide, and zirconia, are ion conducting materials. In these materials, the ionic conductivity is two orders higher in magnitude than the electronic conductivity. To improve the electronic conductivity, a second ceramic phase with higher electronic conductivity such as  $TiO_2$ ,  $TbO_2$ , and  $CuO$  is introduced and doped to the structure. These materials not only increase the electronic conductivity but also helps to stabilize the fluorite cubic structure at high elevated temperatures. The amount needed to stabilize zirconia cubic structure is 12-13 mol%  $CaO$ , 8-9 mol%  $f Yb_2O_3$

and 8-12mol%  $\text{Sc}_2\text{O}_3$  and with other rare-earth oxides. The substitution of divalent or trivalent ions site  $\text{Y}^{3+}$ ,  $\text{Ca}^{2+}$  for  $\text{Zr}^{4+}$  sites generate oxygen vacancies that compensate for the charge loss and allow oxygen ion migration. The solid solution of zirconia with scandium oxide has the highest conductivity of  $0.32 \text{ Scm}^{-1}$  at  $1000^\circ\text{C}$  for 8 mol% of  $\text{Sc}_2\text{O}_3$  solution in  $\text{ZrO}_2$  [9, 29-33]. Fluorite structures shows lower oxygen permeability around ( $10^{-11}$ - $10^{-8} \text{ mol cm}^{-2}\text{s}^{-1}$ ) between ( $600$  to  $1527^\circ\text{C}$ ). One of the best materials is bismuth doped yttrium and samarium oxides that achieve a flux of  $7.75 \times 10^{-8} \text{ mols}^{-1}\text{cm}^{-2}$  at  $930^\circ\text{C}$  with a thickness 1.225 mm from a rich atmosphere with an oxygen partial pressure of 0.5 atmospheres to a deprived atmosphere with an oxygen partial pressure of 0.071 atmospheres [34].

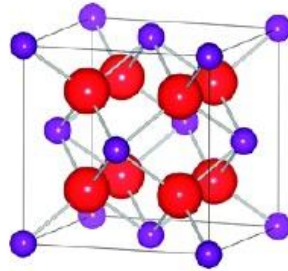


**Figure (2.3)** ideal fluorite structure. Cations are represented as blue atoms, occupying face-center positions and the corners of the unit cell [35]

Figure (2.4) shows a perovskite oxide crystal structure,  $\text{ABO}_3$ , where A and B are cations. The total valence number of A-sites and B-sites is equal to 6, but in the real-world perovskite exist with an oxygen anion deficiency or excess depending on the total valence number on both A and B sites. Oxides with perovskite structure attracted more attention due to high electronic conductivity, which is lower than ionic conductivity by more than one order of magnitude. Improving conductivity and material stability can be easily achieved on the perovskite structure by doped in A and B site position with another cation, turning the materials to wide application. The oxygen permeation fluxes for the perovskite structure membrane can reach  $10^{-10}$ - $10^{-6} \text{ mol cm}^{-2}\text{s}^{-1}$  between  $800$  and  $1000^\circ\text{C}$ .  $\text{SrCo}_{0.8}\text{Fe}_{0.2}\text{O}_{3-\delta}$  perovskite structure

exhibits an oxygen permeation flux of  $2.485 \times 10^{-6}$  mols<sup>-1</sup>cm<sup>-2</sup> at 870°C with a thickness 1mm from a rich atmosphere with oxygen partial pressure of 0.21 atmospheres to a deprived atmosphere with an oxygen partial pressure of 0.001 atmosphere [7, 9, 36].

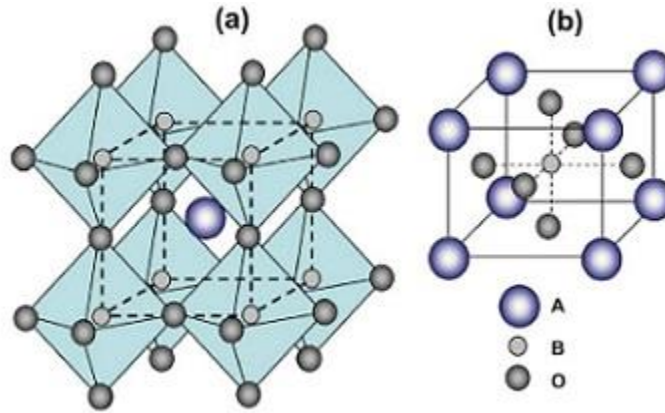


**Figure (2.4)** The structure of perovskite ABO<sub>3</sub>. (a) corner-sharing (BO<sub>6</sub>) octahedral with A ions located in 12-coordinated interstices. (b) B-site cation at the center of the cell [37]

Fluorite structure exhibit high chemical stability under harsh operating condition, but the oxygen flux rate is very depressed due to the deficiency of sufficient electronic conductivity. On the other hand, the perovskite structure exhibit high oxygen flux, but often suffers from material instability under harsh operating conditions, which make them unsuitable for industrial applications. Consequently, double-phase composite membranes consisting of fluorite with higher ionic conductivity and the second ceramic phase with higher electronic conductivity, such various oxide perovskites, ceramic- metallic based and ceramic-ceramic based have been conceived. These membranes are very promising due to stability and enough ionic and electronic conductivity that provide maximum oxygen permeation. The dual-phase membrane that contains yttria stabilized with bismuth oxides-silver is reported to achieve oxygen permeation flux about  $10^{-7}$  mols<sup>-1</sup>cm<sup>-2</sup> even at a lower temperature around 500°C. Maximizing oxygen flux and reducing operation temperature are required for industrial applications to avoid energy penalties [38, 39].

Membrane thickness plays a major role in oxygen flux permeation. According to Wanger's equation (2.1) we can increase oxygen permeation by reducing the thickness of the membrane. The bulk diffusion is the limiting step if the membrane thickness is too high. The oxygen permeation flux in such a case can also be explained by Wanger equation (2.1). When the thickness is decreased, the surface exchange reaction is the limiting step. Here, Wanger equation can be modified to include the surface reaction kinetics as shown (2.2)[40]:

$$J_{O_2} = \frac{1}{1 + \left(\frac{2L_c}{L}\right)} \frac{R^{-T}}{16F^2L} \int_{P''_{O_2}}^{P'_{O_2}} \sigma_i d \ln P_{O_2} \quad (2.2)$$

where  $L_c$  is the characteristic thickness represent the transition thickness from the dominantly bulk diffusion to the surface exchange reaction. The membrane thickness reduction will enhance oxygen permeation only when the thickness value above  $L_c$  thickness. Values lower than  $L_c$  will be useless since oxygen permeation is limited to surface reaction exchange only. Membrane configuration is also equally important in determining the membrane performance. Different membrane geometries, such as a disk, tubular and hollow fiber, have been proposed and experimented. The hollow fibers exhibit high oxygen permeation flux due to the very thin transport layer, large permission area per unit volume and less sealing area compare to other geometries [9, 18, 41].

To raise the oxygen permeation flux further, surface modification can be applied through, surface roughening vis acid etching and adding surface coating layer with superior oxygen exchange conductivity, these methods are important to enhance the oxygen permeation flux and avoid chemical and mechanical properties of the membrane [42-44]. Different coating materials are used such as LSCF ( $La_{0.6}Sr_{0.4}Co_{0.2}Fe_{0.8}O_{3-\delta}$ ), SCFe ( $SrCo_{0.8}Fe_{0.2}O_{2-\delta}$ ), BSCF ( $Ba_{0.5}Sr_{0.5}Co_{0.8}Fe_{0.2}O_{3-\delta}$ ), LSC ( $La_{0.6}Sr_{0.4}CoO_{3-\delta}$ ), STF ( $SrTi_{0.5}Fe_{0.5}O_{3-\delta}$ ) and LSM ( $La_{0.7}Sr_{0.3}MnO_{3-\delta}$ ). Young-il Kwon [45] studied the oxygen flux permeation of fluorite-rich dual

phase membrane GDC ( $\text{Ce}_{0.5}\text{Gd}_{0.1}\text{O}_{2-\delta}$ ), as a function of thickness through the adoption of various coating materials. The research reported an increase in oxygen flux for coating membranes due to, increase in the oxygen chemical potential gradient and thus the increased surface exchange kinetics coefficient. The oxygen permeation flux improved in the order of  $\text{LSC} > \text{STF} = \text{LSCF} > \text{LSM/GDC} > \text{LSM}$  for coating materials. Also, it was noted that coating materials with higher electronic conductivity is not required to significantly improve oxygen flux permeation. Research [46] on LSCF hollow fiber as the substrate membrane under surface treatment with hydrochloric acid-etching was studied.  $(\text{La}_{0.5}\text{Sr}_{0.5})_2\text{CoO}_{4+\delta}$  and  $\text{K}_2\text{NiF}_4$ -type oxide surface decoration catalyst were chosen to improve the oxygen reduction reaction. The result shows higher oxygen permeation flux for the acid-etched LSCF membrane than the bare LSCF membrane and the oxygen flux is further increased for decoration surface. The oxygen flux through an acid-etched and decoration LSCF increased from 0.036 to 1.021, 0.067 to 1.131 and 0.201 to 1.311  $\text{ml min}^{-1} \text{cm}^{-2}$ , respectively, when the operating temperature increased from 700 to 1000°C. Increasing the temperature led to bulk diffusion to dominate over the surface reaction exchange step and resulted in a decrease in the oxygen flux. The result emphasizes that surface treatment is indeed important to improve surface catalytic activity, and thus higher oxygen flux.

Operation condition such as temperature and pressure have also been reported to impact the oxygen flux permeation because the concentration of defect in the MIEC is a function of temperature and pressure [18]. Higher oxygen flux can achieve by elevating temperature, resulting in an increase in oxygen flux from 0.006 to 0.419  $\text{ml.min}^{-1}\text{cm}^{-2}$  when the temperature increases from 750 to 950°C for LSC hollow fiber. This increase has been attributed to improvement in both oxygen bulk and surface reaction exchange conductivity at higher temperature [41, 46]. Another technique to improve oxygen permeation is increasing the oxygen

partial pressure gradient on the feed side and the permeate side. This can be done by using high pressure air on the feed side between 15 to 20 bar [47] or pressure below atmospheric on the permeate side by applied vacuum condition or using different sweep inert gas flow rate. It was reported [41] that oxygen permeation flux increased about 1.4 times for different membrane materials by changing the helium gas flow rate from 100 to 300 ml min<sup>-1</sup>.

Other conditions that can affect the oxygen permeation flux values had reported by many researchers. In one report [9] different sealing materials were found to affect the oxygen flux. Typically, any membrane under investigation will be sealed into a tube with one side exposed to the air and the other to sweep inert gas. The effective sealing critical to reduce gas leakage and ensure oxygen purity. Electronic conductive sealant silver paste and non-electronic conductive ceramic paste sealant was used with three conducting materials, a) PBC with very high electronic conductivity, b) BSCF5582 with very high oxygen permeability and c) modest electrical conductivity SDC with higher ionic conductivity. The electronic conductive sealant was founded to prepare an external short circuit for electronic conductivity and as a consequence, the sealant affected oxygen flux. The SDC membrane with silver sealant showed oxygen flux improvement due to the external short circuit created from the silver paste, which increased the electrical conductivity of the membrane. There was no substantial improvement in oxygen flux for both PBC and BSCF5582 membrane because there was enough electrical conductivity.

The permeation of oxygen flux doesn't only depend on membrane thickness or operating conditions. The great variation in flux was reported on membranes with the same material composition, but with a different preparation technique. The difference in the technique affected the resulting microstructure, impurity, bulk conductivity, the surface reaction exchange and sweep flux for the inert gas on the permeate side [48, 49].

## **2.2 Application for oxygen transport membranes (OTM)**

Oxygen is an important gas used in several industrial processes, the worldwide demand increased lately due to its potential impact on energy, environmental and cost. Consequently, new oxygen production technology needs to be investigated to replace the old production technologies such as cryogenic distillation and pressure swing adsorption. Oxygen transport membrane (OTM) has drawn the attention of researchers due to the possible impact on energy and the environment and other applications. The OTM can be integrated with several industrial applications such as solid oxide fuel cell, membrane reactors, and other air separation needs.

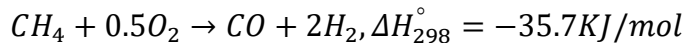
### **2.2.1 Integrated OTM in fuel cell**

The solid oxide fuel cell (SOFC) is a high temperature electrochemical device to efficiently convert chemical energy into electricity with low emission and a broad range of fuels. The (SOFC) made from two materials which are applied to make four distinct layers, the electrolyte, interconnect, the anode and the cathode layers. The electrolyte is a ceramic ionic conductor, the interconnect is ceramic electronic conductor while both cathode and anode are manufactured from a combination of ionic and electronic ceramic materials. The operation of the solid oxide fuel cell set off when the cathode reacts with incoming air and oxygen molecular is generated due to electrons transferred from the anode. Fuel is fed to the anode and oxidized by the oxygen ions that diffused from the cathode through the electrolyte, the interconnector is another important component of SOFC, because it separates the anode and the cathode into two gas chambers to avoid the direct mixing of fuel and air. The efficiency of the SOFC is higher than 80% compared to the conventional combustion power generation [50-53].

### **2.2.2 Integrated OTM in chemical reaction**

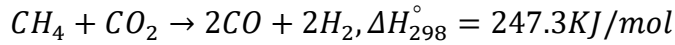
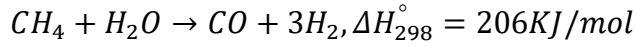
The integration of oxygen transport membranes (OTM) with the chemical reaction process in a single unit reactor has been considered, due to the huge advantages they provide. The catalytic membrane reactor (CMR) offers (i) lower air separation cost and energy consumption, (ii) chemical reaction stability and safety due to removal of one or more products through the membrane, which achieved higher conversion and yield and (iii) the gradual introduction of oxygen will provide partial oxidation and prevent further oxidation. The critical issue on such technology is to achieve high membrane stability under high temperature and pressure. There are several examples of the integrated oxygen membrane of the chemical reaction as follows:

(I) Partial oxidation of methane (POM) to produce syngas according to the following reaction [54]:



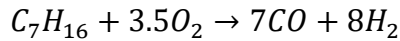
The membrane materials used in the POM process must be chemically stable for a long time at extreme operating condition under reducing hydrogen, carbon monoxide at the oxygen permeation side, show mechanical strength and design membrane reactor with the new configuration, such as multichannel hollow fiber membrane reactor, that show good mechanical strength and a high oxygen permeation flux along with excellent reaction performance. [55] investigated the reaction performance of the perovskite tubular shape  $Ba_{0.5}Sr_{0.5}Co_{0.8}Fe_{0.2}O_{3-\delta}$  with  $LiLaNiO/\gamma-Al_2O_3$  catalyst membrane as a function of temperature, air flow, and methane concentration. The results show good stability after 500h with higher than  $8ml\ cm^{-2}\ min^{-1}$  oxygen permeation flux, 94% pure methane conversion and higher than 95% carbon monoxide selectivity.

(II) Oxidation reforming of methane to syngas, that can be executed by steam reforming and carbon dioxide by the following reactions [54, 56]:



In the conventional steam reforming technology reaction required high temperature and due to the endothermic process, therefore 80% conversion of methane at 850°C is achieved. Using a membrane reactor will reduce operative conduction, increase methane conversion and higher hydrogen recovery. Carbon dioxide reforming of methane was studied with ceramic membrane SrFeCo<sub>0.5</sub>O<sub>x</sub> and powder catalyst Pt/ZrO<sub>2</sub>. The result showed a more than three times higher conversion with membrane than with any amount of co-fed oxygen [57].

(III) Oxidation reforming of liquid heptane fuel to carbon monoxide and hydrogen mixture as shown in the reaction below:

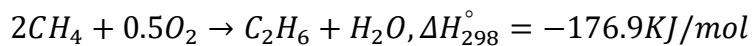
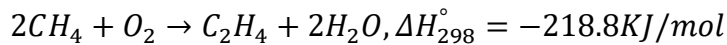


Oxidation reformation of heptane through dense oxygen permeable membrane

Ba<sub>0.5</sub>Sr<sub>0.5</sub>Co<sub>0.8</sub>Fe<sub>0.2</sub>O<sub>3</sub> was reported with catalyst LiLaNiO/γ-Al<sub>2</sub>O<sub>3</sub> [58]. The membrane exhibited an oxygen permeation flux of around 11.5 ml cm<sup>-2</sup> min<sup>-1</sup> and the reaction took place at 850°C.

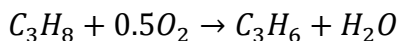
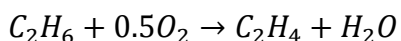
100% heptane conversion was achieved along with carbon monoxide selectivity of 91-93%.

(IV) Oxidative coupling of methane (OCM) is a process that converts natural gas, which is 95% methane over a catalyst at a higher temperature in a form C<sub>2</sub> products (ethane and ethylene) as the following reaction [54]:



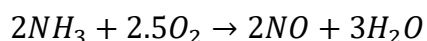
Due to failure to achieve higher C<sub>2</sub> yield through direct reaction, membrane reactors have the potential to increase the selectivity and yield, reduce power consumption, improving operational safety and cut the capital cost by minimizing the reactor system. Akin\_et\_al [59] investigated dead end tubular Bi<sub>1.5</sub>Y<sub>0.3</sub>Sm<sub>0.2</sub>O<sub>3</sub> fluorite membrane in a temperature range between 870-930°C using different feed techniques. The result indicated that yield achieved from oxidative coupling of methane was 35% at a C<sub>2</sub> selectivity of 54% at 900°C. At the same C<sub>2</sub> yield, the membrane reactor model gives C<sub>2</sub> selectivity of over 200% higher with very low methane partial pressure.

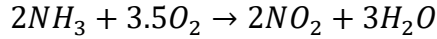
(V) Oxidative dehydrogenation (ODH) of alkanes for producing ethylene and propylene by means the oxidative dehydrogenation of ethane and propane have also been conducted using membrane technologies. ODH can be represented by the following reaction:



Ethylene is an important precursor for several industries, and it is produced by steam cracking of ethane, which is highly endothermic reaction. The use of a membrane reactor reduces the energy demand for the process. Pilar Lobera [60] studied the high ethylene production from ethane through the membrane Ba<sub>0.5</sub>Sr<sub>0.5</sub>Co<sub>0.8</sub>Fe<sub>0.2</sub>O<sub>2-δ</sub> reactor with respect to the oxygen concentration in the reaction side and using Argon and methane as inert dilutants to improved reaction stability. Higher ethylene selectivity was achieved at 850°C were 383 mLmin<sup>-1</sup>cm<sup>-2</sup> for Ar and 353 mLmin<sup>-1</sup>cm<sup>-2</sup> for CH<sub>4</sub>, with the selectivity of 80 and 90% respectively. It is believed that the use of a catalytic coating on the MIEC membrane will improve ethylene production.

(VI) Another process of significance to the use of membranes is the selective oxidation of ammonia to produce nitrogen oxides, as the following reactions:





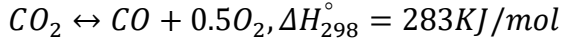
NO production is an important intermediate in the production of nitric acid. The typical reaction yields 94-96% NO and 4-6%, by-product (N<sub>2</sub>O and N<sub>2</sub>) at 1073-1223K with a platinum-based catalyst. The process is expensive due to loss of the catalyst metal and the ascendancy of the by-product gas N<sub>2</sub>O which is environmentally harmful. The use of perovskite membrane such as La<sub>1-x</sub>A<sub>x</sub>FeO<sub>3-δ</sub> (A=Ca, Sr; x=0.1-0.2) and Ba<sub>0.5</sub>Sr<sub>0.5</sub>Co<sub>0.8</sub>Fe<sub>0.2</sub>O<sub>3-δ</sub> showed higher selectivity and no N<sub>2</sub>O emission [61, 62].

(VII) The coupling reaction with water splitting is considered as an extractor reaction configuration where the membrane is utilized to selectively remove a product from the reaction zone [63-65]. As the show in the following reaction:



Hydrogen production with high purity and sustainable energy is gaining huge attention due to hydrogen used as alternative energy resources. Hydrogen production from water is still challenging due to the low equilibrium constant at 950°C. Using MIEC at a moderate temperature will shift the equilibrium constant toward dissociation by removing either oxygen or hydrogen instantaneously [50]. Li\_et\_al [66] investigated water splitting technology through the MIEC oxygen permeable membrane. The reactor was equipped with 0.5-mm-thick Ba<sub>0.98</sub>Ce<sub>0.05</sub>Fe<sub>0.95</sub>O<sub>3-δ</sub> membrane. When steam is fed to one side and a low purity hydrogen gas fed to the other side. Oxygen from the steam side permeates through the membrane to react with low hydrogen purity, leaving the steam side after condensation and drying with higher hydrogen purity only. A higher hydrogen separation rate achieved 13.5 mLcm<sup>-2</sup>min<sup>-1</sup> at 950°C.

(IIX) Thermal decomposition of carbon dioxide coupling with partial oxidation of methane, which also considers as extractor type membrane reaction is shown below:



One of the technologies is decomposing carbon dioxide to oxygen which is used in several industries and carbon monoxide which also consider a raw material in the synthesis of a chemical product. One drawback of such technology is a highly endothermic reaction with a huge energy penalty. Jin\_et\_al [67] proposed coupling thermal decomposition of carbon dioxide with partial oxidation of methane into syngas through a dense mixed-conducting membrane reactor. The membrane used is  $SrCo_{0.4}Fe_{0.5}Zr_{0.1}O_{3-\delta}$  at 1173K and the effect of temperature and feed flow of  $CO_2$  and  $CH_4$  were considered. The reaction of  $CO_2$  decomposition took place on one side of the membrane and the POM reaction occurred on the other side of the membrane simultaneously. The results indicate a  $CO_2$  conversion about 11/1% and  $CH_4$  conversion, CO selectivity, and the ration of  $H_2/CO$  were 84.5%, 93% and 1.8 respectively.

(IX) Coupling the reaction with  $NO_x$  decomposition into nitrogen and oxygen as shown in the reaction below:



The nitrogen oxides are considered major air pollutants generated from any combustion processes. The direct decomposition of NO on perovskite is suffering from inhibited and thus, decreases NO conversion. To overcome such problem oxygen can be adsorbed by the membrane and removed from the reaction. Jaiang [68] developed a novel perovskite hollow fiber membrane  $BaCo_xFe_yZr_{1-x}O_{3-\delta}$  for NO decomposition, where a complete NO conversion with around 95%  $N_2$  yield and 3% coexisting  $O_2$  in the feed was achieved.

### **2.2.3 Integrated OTM in power production**

Oxygen separation from the air is the future technology through a ceramic-bases membranes, the oxygen demand is expanding more than 100 million tons of oxygen are produced every year and the demand expected to increase due to numerous applications in every industrial sector around the world [69]. Oxyfuel combustion is a process to burn hydrocarbons fuel using oxygen instead of air, which produce flue gas mainly contain  $H_2O$  and  $CO_2$ , thus eliminate the presence of nitrogen in the flue gas and avoid the formation of  $NO_x$ . The  $CO_2$  can easily separate from  $H_2O$  and captured, where can be liquefied or sequestered. In addition, the energy input to the system will be less because there is no need to heat the nitrogen gas, which is about 80% of air to combustion temperature. The cryogenic method is now used to provide the oxygen required for the oxyfuel power unit, which is energy intensive, the energy demand for oxygen production is about  $240KWh/t_{O_2}$  resulting in an overall efficiency drop of the power plant by 8-10%-point [70].

Oxygen transport membranes (OTM) are integrated to power units and can be used to supply the oxygen required for the combustion by heating the membrane to the temperature about  $800^{\circ}C$  and applying a partial oxygen pressure difference across the membrane. The energy requirement for oxygen separation through the membrane is  $147KWh/t_{O_2}$  compared to  $240KWh/t_{O_2}$  for cryogenic air separation, therefore the total efficiency drops in power plant operated with oxygen membrane transport integration, including  $CO_2$  compression by about 5.3%-points [71, 72]. OTM can be integrated and operated in the oxyfuel combustion process either in three-end or four-end mode. In the three-end mode, oxygen is extracted from the membrane by increasing the feed pressure or by a vacuum pump as shown in figure (2.5.a), while in the four-end mode, the flue gas is recycled and used as a sweep gas on membrane

oxygen permeation side as in figure(2.5.b) [73-76]. The membrane materials integrated with power production need to be chemically stable and maintain high oxygen permeability in the presence of CO<sub>2</sub> and other gases. Therefore, the three-end mode is more feasible to apply because there is no direct contact between the flue gas and membrane materials.

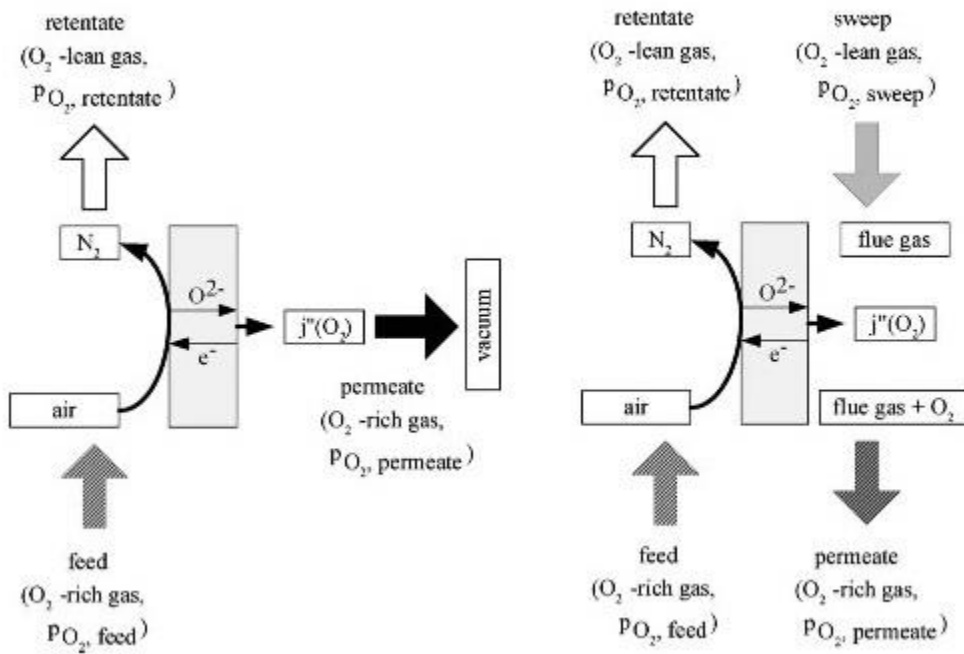


**Figure (2.5)** Schematic of membrane for oxygen separation in oxyfuel processes using (a) three-end concept (b) four-end concept [72]

Griffin [77] proposed advance zero emissions gas turbine power plant cycle (AZEP), where the ordinary gas turbine combustion chamber is replaced with a mixed conductive membrane reactor, which includes a combustor, air preheater, oxygen separation membrane, and heat exchanger. Air is compressed in the gas compressor to 20 bar and around 450°C, then the compressed air is preheated to about 900-1100°C. It is then passed through the oxygen transport membrane. Preheating the air helps in increasing the permeability of the oxygen membrane and reduce the required membrane area. Natural gas is burned with nitrogen-free environment in the combustor and the flue gas is fed to power generation turbine, part of flue gas is recirculated into

the reactor to preheat air enters the membrane as shown in figure (2.6). The design of the MIEC membrane reactor and the heat exchanges are based on monolithic structure (honeycombs) with a high surface to volume ration and low pressure drop. The membrane material needs to withstand the combustion temperature of 1300°C also carbon dioxide resistance, which is difficult in the current available materials [69].

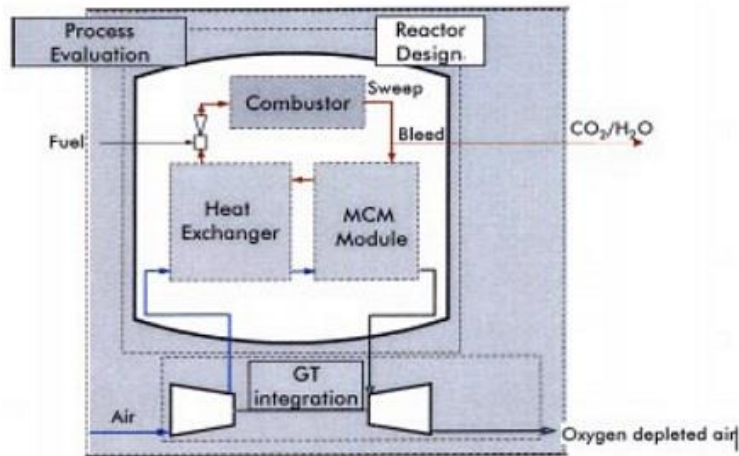


**Figure (2.6)** AZEP cycle work package [77]

[78] studied the economic performance of the AZEP combined cycle with ordinary different size combined cycles. The result shown uncertainties in mixed conducting membrane reactor cost and the life expectancy of mixed conducting membrane reactor do not have a big influence on the cost of electricity.

Yantovski suggested a zero emission ion transport membrane oxygen power (ZEITMOP) cycle shown in figure (2.7), where the ion transport membrane (ITM) reactor is separated from the combustion chamber, to overcome the destabilization of the membrane material due to exposure to higher temperatures. In addition, this also results in attainment of higher efficiencies by the gas turbine when the combustion process occurs at the highest pressure and temperature. The cycle efficiency is claimed as 46% due to the limitation of inlet gas temperature to the gas turbine to 1300°C. The efficiency will be increased to 56% if the inlet temperature is increased to 1500°C.



generate syngas, the air separation unit (ASU) to provide high purity oxygen, the quenching/scrubbing process to remove pollutants, and the combined cycle for power generation. The cryogenic distillation process consumes about 10-20% of the total power output and 70% of the auxiliary power consumption [81], therefore using ion transfer membrane will increase the cycle efficiency. Han reported 1% and 0.6% higher net efficiency when ITM technology is used in ASU for IGCC cycle. In addition, ITM ASU is beneficial to increase steam turbine output and reduce the energy penalty of the ASU.

### **2.3 Oxygen pickup and release**

There are many factors that affect the oxygen transport through the membrane as discussed previously. The reaction of oxygen on the feed side of the membrane or the permeate side fluid often controls the rate for a thin membrane [11]. Applying a coating layer on the faces of the membrane is one solution to increase the rate of these reactions and improve the stability of the membrane reactor. Hence, picking out the right materials that can behave as an oxygen carrier is a vital measure in the procedure. Oxygen carrier materials are extensively analyzed and is dependent on many of the same desired properties as in chemical looping combustion (CLC). CLC offers power production and CO<sub>2</sub> capture via separation of air and fuel using the intermediate oxygen carrier that is oxidized by air in the air reactor and reduced with the fuel in the fuel reactor. A successful operation of the chemical looping process depends on the oxygen carrier characteristics, such as oxygen transport capacity, a high reaction rate with the fuel, complete fuel conversion to CO<sub>2</sub> and H<sub>2</sub>O, long term recyclability and durability, mechanical strength, suitable heat capacity and high melting points, lower cost and have no health and environmental impact [13]. Among various metals Ni, Fe, Cu, Mn, and Co- based materials are used as oxygen carriers These materials exhibit strong oxidation potentials and can be used for

full or partial fuel oxidation. They, however, present some disadvantages such as low reactivity with different fuel types and oxygen transport capacity limitation of Fe and Mn, low melting points and high agglomeration tendency of Cu, as well as a higher cost and environmental effect of Ni and Co [82].

Ni-based oxygen carriers exhibit higher reactivity and very good performance when working at high temperature (900-1100<sup>0</sup>C). Complete methane conversion is achieved during the CLC process, although thermodynamic restrictions result in a small presence of CO and H<sub>2</sub> in the gas outlet of the fuel reactor [83]. Ni oxide is expensive and easily deactivated by sulphur from the fuel. Therefore, it is not suitable with solid fuel such as coal [84]. In addition, the use of Ni oxide requires more safety measures because of its toxicity. NiO is the only oxide state for Ni-based particles, which show low porosity, therefore NiO particles have a low reaction rate [85, 86]. Improved Ni-based oxygen carrier materials are required to tackle these drawbacks for further application. Adding different compounds as supporting materials and different methods to prepare the Ni-based oxygen carriers impact the reactivity, regeneration, agglomeration and mechanical strength of the particles [87-89].

Copper is another material that has been investigated as an oxygen carrier in the CLC. Copper showed high reaction rates and very good oxygen transport capacity, and contrary to Ni, it has no thermodynamic restrictions for complete fuel conversion to CO<sub>2</sub> and H<sub>2</sub>O. Copper has flexible redox behavior between the oxidizer state CuO and reduced Cu or Cu<sub>2</sub>O state. In addition, copper is cheaper and causes less environmental problems compared to other materials such as Ni and Co used in CLC. There are two drawbacks of Cu-based materials that limit the use of Cu as an oxygen carrier. The first is attrition due to weakness in mechanical strength when the number of redox cycles is increased. The second is agglomeration as a result of the

low melting point of Cu (1085°C), which limit the fuel reactor operation temperature to (800°C), to avoid melting problem [90, 91]. To improve the oxide performance different compounds are added as support materials ( $\text{Al}_2\text{O}_3$ ,  $\text{MgO}$ ,  $\text{SiO}_2$ ,  $\text{TiO}_2$  and  $\text{ZrO}_2$ ). The resulting compound exhibits excellent chemical stability and maintain mechanical strength after multicycle operations [92].

Another interesting material has been investigated is manganese because this metal has various oxidation states, including  $\text{MnO}_2$ ,  $\text{Mn}_2\text{O}_3$ ,  $\text{Mn}_3\text{O}_4$  and  $\text{MnO}$ . It is cheap, has good oxygen transport capacity and is non-toxic. Only  $\text{Mn}_3\text{O}_4$  and  $\text{MnO}$  can be consider for CLC because they are thermodynamically and chemically stable under a higher temperature while other oxides state decompose around 500°C. The use of pure Mn-based as OC shows low reactivity with methane or coal [93, 94]. Therefore, several compounds such as bentonite and  $\text{ZrO}_2$  are stabilized with the addition of  $\text{MgO}$ ,  $\text{CaO}$  or  $\text{CeO}_2$ . The materials showed high reactivity, limited physical changes and lower agglomeration [95, 96]. Abad [97] studied Mn-based stabilized zirconia in a continuous operating laboratory CLC unit, where methane and syngas were used as fuel in the fuel reactor. The thermal power was between 100 and 300W. The result showed lower reactivity with methane because methane was detected in the exit flue gases, while it achieved a complete conversion with syngas. Combustion efficiency ranged between 0.88 to 0.99. Efficiency increased temperature and decreased with fuel flow rate. In contrast, using supports such as  $\text{SiO}_2$ ,  $\text{TiO}_2$ ,  $\text{Al}_2\text{O}_3$  or  $\text{MgAl}_2\text{O}_4$  form stable and unreactive materials resulting in inhibiting reactivity, thereby making them unsuitable as oxygen carriers [98-100].

Cobalt oxide was considered as a possible oxygen-carrier material due to its high reactivity and oxygen transport capacity. However, they suffer from high cost and environmental problems. Most cobalt common oxide, stable state  $\text{CoO}$ , and  $\text{Co}_3\text{O}_4$ , but only the

loop between CoO and Co are considered during the redox operation in CLC applications. CoO is thermodynamically stable at all temperatures, while  $\text{Co}_3\text{O}_4$  is not stable at  $900^\circ\text{C}$ , and converted into CoO [83]. Even when CoO and Co is used in CLC applications, a maximum conversion of 95 to 97% of  $\text{H}_2$  and 89 to 97 % for CO is achieved in the temperature range  $800\text{--}1200^\circ\text{C}$ . Therefore, Co-based materials have attracted little attention. Cobalt reacts strongly with the inert supports such as  $\text{Al}_2\text{O}_3$ ,  $\text{TiO}_2$  and  $\text{MgO}$  to form unreactive materials  $\text{CoAl}_2\text{O}_4$ ,  $\text{CoTiO}_3$ , and  $\text{Mg}_{0.4}\text{Co}_{0.6}\text{O}$  which result in almost complete loss of reactivity [99, 101]. In contrast, the Co-based oxygen carrier with YSZ (yttria-stabilized zirconia) as support was found to exhibit good reactivity and high resistance to carbon formation in CLC applications [101].

Iron based materials are commonly used as an oxygen carrier in chemical looping applications, despite their low reactivity and low oxygen transport capacity. They are still a good option due to their low price, high mechanical strength, high melting point, no tendency for carbon or sulfur deposition, making them promising candidates with all chemical looping applications involving carbon and sulfur containing fuel and is environmentally friendly [102, 103]. Furthermore, iron oxide presents the highest oxygen storage capacity from  $\text{CO}_2$  ( $0.7 \text{ mol CO}_2/\text{mol Fe}$ ) over a wide range of operating temperatures ( $600$  to  $1800^\circ\text{C}$ ) [104]. Fe-based OC has different oxidation states (Fe, FeO,  $\text{Fe}_3\text{O}_4$ ,  $\text{Fe}_2\text{O}_3$ ), but only  $\text{Fe}_2\text{O}_3$  to  $\text{Fe}_3\text{O}_4$  are considered for CLC industrial applications due to thermodynamic limitations. In addition, a further reduction to FeO or Fe would decrease the  $\text{CO}_2$  purity in the fuel reactor and increase the concentration of CO [105]. A variety of supports such as  $\text{Al}_2\text{O}_3$ ,  $\text{MgAl}_2\text{O}_3$ ,  $\text{SiO}_2$ ,  $\text{TiO}_2$ , and Zr-based, etc. have been used to increase oxygen transport and reactivity.  $\text{Al}_2\text{O}_3$  is the most common support used and provides a positive effect on the oxygen transport capacity due to formation  $\text{FeAl}_2\text{O}_4$ . The drawback of Fe-based materials is the relatively low reactivity toward

gaseous fuels and the agglomeration related to magnetite formation. Therefore, developing new generation Fe-based OC needs to focus on solving these issues.

Figure (2.8) compares key information for traditional oxygen carrier materials, where (a) represent a comparison of Ni, Fe, Cu, Mn and Co-based oxygen carriers in the term of oxygen transport capacity, (b) melting point and (c) cost, reactivity, agglomeration and attrition resistance.

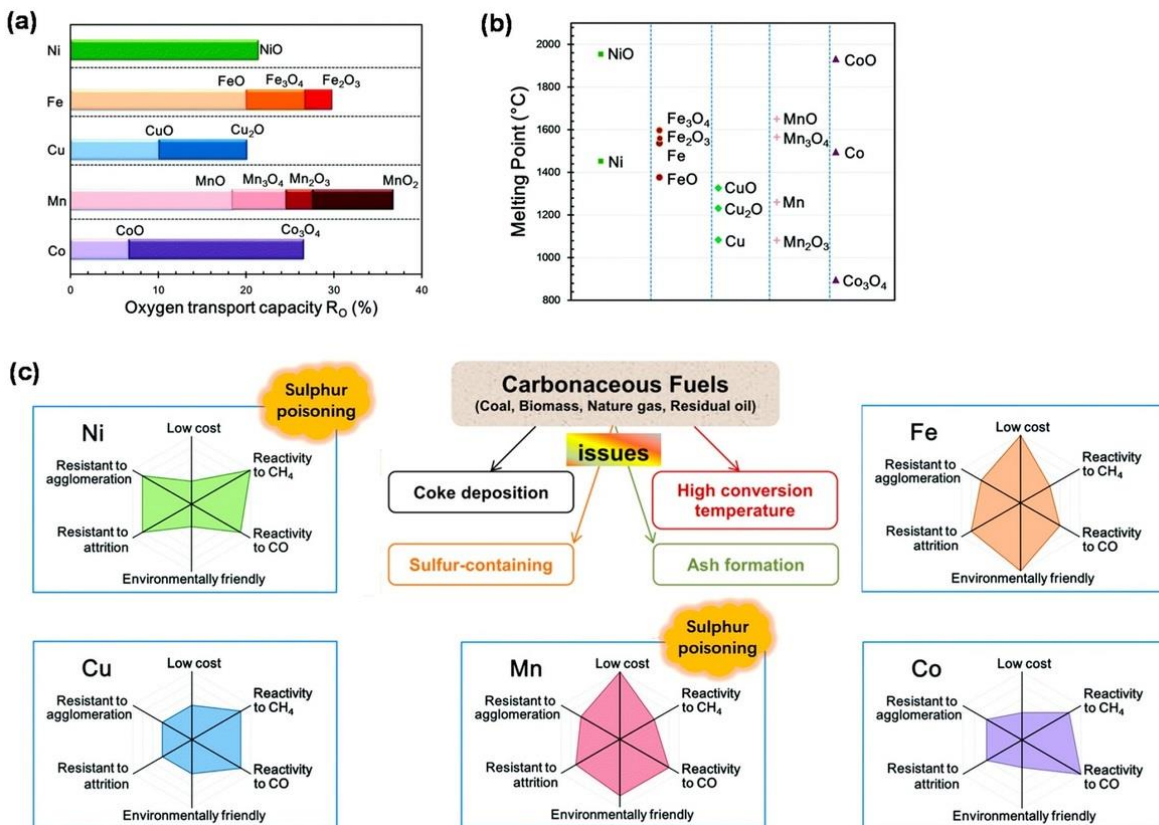


**Figure (2.8 a,b and c)** Comparison among tradition oxygen carrier [102]

In addition to the traditional oxygen carrier materials, mixed oxides and perovskite materials are considered as oxygen carriers to provide more beneficial properties than those individual metal oxides. Mixed metal oxides are prepared to overcome the drawback of these individual metal oxides and improve reactivity, oxygen transport capacity, stability, mechanical strength, attention rate, conversion of the fuel gas and carbon deposition [106-108]. Other

complex metal oxide with perovskite structure had been investigated to be used as oxygen carriers. Ryden [109] investigated  $\text{La}_x\text{Sr}_{1-x}\text{Fe}_y\text{Co}_{1-y}\text{O}_{3-\delta}$  perovskites by reduction with  $\text{CH}_4$  and oxidation with air in a fixed-bed quartz reactor at  $900^\circ\text{C}$ , with additional three oxygen carriers based on  $\text{NiO}$ ,  $\text{Fe}_2\text{O}_3$  and  $\text{Mn}_3\text{O}_4$ .  $\text{La}_x\text{Sr}_{1-x}\text{Fe}_y\text{Co}_{1-y}\text{O}_{3-\delta}$  perovskites were found to have the potential to be used for CLC applications due to the high conversion of  $\text{CH}_4$  into  $\text{H}_2\text{O}$  and  $\text{CO}$ . It does not seem to provide any obvious advantages compared to proven metal oxide materials.

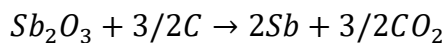
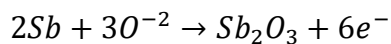
#### **2.4 Molten oxygen carriers**

Molten metal oxides were proposed to be used in chemical looping combustion or gasification applications to avoid challenges face regular solid metal oxides, such as agglomeration, attrition, structural change due to redox cycles and erosion. In addition, solid metal oxide particles limit the system operating temperature to around  $1000^\circ\text{C}$  to avoid softening and damage if the particles. Thus, using molten metal oxide will offer higher operating temperature and and increase system efficiency. However, new challenges are associated with handling the molten metal oxides, selection of proper materials to withstand higher temperature and solidification of molten metal [8]. There are many metals, mostly in groups 3A through 6A, that exist in liquid form at the operating temperature [110]. Picking out the best candidates for molten metal oxygen carriers depends on different parameters such as melting point temperature, as well as the Gibbs free energy and reaction enthalpy. For example, some of the oxides requires much higher temperatures for melting: eg  $\text{SnO}$  at  $1080^\circ\text{C}$  with a second form  $\text{SnO}_2$  at  $1630^\circ\text{C}$  and chrome in the form of  $\text{CrO}_3$   $197^\circ\text{C}$ ,  $\text{Cr}_2\text{O}_3$   $243.5^\circ\text{C}$  and  $\text{CrO}$   $300^\circ\text{C}$  [111]. In addition, solidification can happen since  $\text{Cr}_2\text{O}_3$  has a higher melting point. Similar challenges exist for  $\text{SnO}_2$ . The solidification cause blockages and degrade performance. Gibbs energy plays a major role in the selection of the molten oxygen carrier. Rhodium oxide has a positive Gibbs free

energy for both oxidation with air and reduction with graphite, which means that the reactions are unlikely to occur at a temperatures in the range 1100°C-1500°C. Additionally, rhodium is both radioactive and a scarce element [111]. Therefore, these elements are excluded and not consider as candidates for the liquid molten oxygen carrier leaving materials such as lead, copper, antimony, and bismuth as possible materials to serve as molten oxygen carriers. Due to the toxicity of lead makes it less desirable metal. Copper oxides, Cu<sub>2</sub>O and CuO have melting temperature are 1230°C and 1325.6°C respectively. Bismuth oxide, Bi<sub>2</sub>O<sub>3</sub>, melting temperature is 817°C. These are relatively high melting point making them suitable to chemical looping combustion and other application [111, 112]. Antimony and its oxide with a melting point of 630°C and 656°C, respectively, is the primary focus of this work [113].

The integrated system of oxygen transport membranes and molten metal oxides as an intermediate is limited and little research has been conducted directly on using a molten metal as an intermediate between the oxygen membrane and fuel. The solid oxide fuel cell (SOFC) that discussed earlier provide such integration where molten metal is served as intermediate between the cathode and anode, where at cathode the oxidation of the molten metal by air occurs and at the anode regeneration of the molten metal by reduction of the metal with fuel, occurs, allowing continuous operation. Antimony and antimony oxide have lower melting temperature, 903K and 929K respectively, making antimony suitable as anode interface in SOFC.

Jayakumar [114] investigated the direct utilization of carbonaceous fuel in SOFC with the molten Sb anode at 973K, where the Sb is oxidized resulting Sb<sub>2</sub>O<sub>3</sub> being reduced by the fuel in a separate step as the following below:



The  $\text{Sb}_2\text{O}_3$  reduction with four solid fuels which are sugar char, rice starch, Carbon black and graphite were studied and the data indicated that at approximately 850K  $\text{Sb}_2\text{O}_3$  begins to reduce with chars, while carbon black required higher temperature around 973K and graphite with lower reaction rates at 1073K. The cell achieved  $300 \text{ mW cm}^{-2}$  power density and 0.5V cell potential. The first case where no carbon is added stability of power for less than 1hr is achieved due to the conversion of 10% of Sb to  $\text{Sb}_2\text{O}_3$  which increase cell resistance and drop the power density, while 12h cell performance remains stable until all of the fuel has been consumed. This proved that the  $\text{Sb}_2\text{O}_3$  formed at the electrolyte interface was being reduced by carbon. The result demonstrates that a fuel cell based on Sb- $\text{Sb}_2\text{O}_3$  redox provides good performance while operating at 973K, and the cell stability depends on the thickness of the Sb and  $\text{Sb}_2\text{O}_3$  film. Furthermore, a broad range of fuel types with different impurity levels is accepted without affecting the high-power density.

Direct carbon fuel cells (DCFCs) are technology to convert solid carbon energy to electricity with higher thermodynamic efficiency. This is an environmentally friendly technology since pure  $\text{CO}_2$  produced in the anode, where it can be collected and reused for industrial application or sequestered. The main challenge is utilizing the solid carbon fuels directly inside the fuel cells due to the difficulty in achieving enough physical contact between the solid fuel and electrode interface [115, 116]. The molten metal used as anode is a promising technology because it possesses the power to convey oxygen and has higher electrical conductivity.

Xu [113] studied the performance of DCFC that used  $\text{Ba}_{0.5}\text{Sr}_{0.5}\text{Co}_{0.8}\text{Fe}_{0.2}\text{O}_{3-\delta}$  (BSCF) as a cathode, samaria-doped ceria (SDC) as the electrolyte, molten Sb- $\text{Sb}_2\text{O}_3$  as the anode and active carbon as solid fuel. 2g of antimony powder was packed in an alumina tube to form the molten

anode, with 0.5g of carbon on top. Nitrogen gas was added as protection gas. The resistance associated with the molten Sb-Sb<sub>2</sub>O<sub>3</sub> electrode is only 0.026, 0.045 and 0.121 Ωcm<sup>-2</sup> at 750, 700 and 650°C, respectively, while the maximum power output reached 327, 268 and 222 mWcm<sup>-2</sup> at the corresponding temperature. The power density of 512.5 mAcm<sup>-2</sup>, with the electrode area of 0.28 cm<sup>2</sup> of the DCFC cell, decreased after 22h, while theoretically must last to 40h until antimony and carbon are used up. This is due to the slow displacement of Sb<sub>2</sub>O<sub>3</sub> by Sb without stirring. This laboratory scale system demonstrated high current densities with the possibility of direct solid carbon conversion and CO<sub>2</sub> capture.

Cao [117] investigated the performance of SOFC with liquid antimony anode numerically. The one-dimensional model fuel cell is fabricated from 500µm smooth single crystal yttria-stabilized zirconia (YSZ) as the electrolyte, 1µm mixed conducting layer YSZ/Pt, 7.5 mm liquid Sb anode and 14µm Pt cathode. The cell discharged at 0.3 V for 30,000 sec and operate at 800°C without providing any fuel or fresh metallic Sb, which mean the fuel cell studied under battery mode. The electrochemical reaction, mass transport and microstructure of the anode were considered, the model showed that at the end of discharging of 30,000 sec, only 35% of metallic Sb is consumed and the insufficient Sb concentration in the anode will weakening the diffusion of metallic Sb. The model is a remarkable tool to describe the ongoing works of liquid Sb in the anode at SOFC and provide useful information to develop and optimized cell performance.

Duan [118] illustrated tubular DCFC design that provided a structural advantage in cell sealing interconnection and refueling. The cell used biomass fuel, porous coconut active charcoal (SAC) and flaky pyrolyzed corn stretch (PCS). The cathode is a LSCF-10GDC ceramic membrane supported by 8mol% Y<sub>2</sub>O<sub>3</sub> stabilized ZrO<sub>2</sub> (YSZ) and molten Sb is used as the anode.

Cell performance at different temperatures, 700, 750 and 800°C, as well as the influence of fuel properties on anode was studied. 5g of Sb and with and without 2g biomass were investigated. The result of the cell battery mode achieved in 700, 750 and 800°C for open circuit voltage (OCV) values 0.741, 0.712, and 0.690 V with maximum power density values 114, 196, and 304 mWcm<sup>-2</sup> respectively. In addition, the cell performance at 750 and 800°C under the current density of 0.4Acm<sup>-2</sup> showed around 1.6h and 2.1h respectively, without carbon added, with CSC 12h and 16h respectively and with PCS around 4h and 12h respectively. The performance of the cell depended on oxidation and reduction kinetics of molten antimony Therefore higher temperature resulted in higher performance, as well as the fuel utilization, its performance.

## CHAPTER 3

### MATHEMATICAL MODEL

#### **3.1 Objective**

The objective of this research is to create a 2D simulation model for the novel oxycombustion system by integrating the OTM, oxycombustion, and LCLC in one reactor. Antimony oxides are used as a mediator that carries the oxygen from the OTM to the fuel site. The overall objective is to understand the temperature distribution inside the reactor to achieve the optimum reactor design. Different oxidation and reduction rates are taken under consideration with respect to different operating temperature.

#### **3.2 System schematic**

The single reactor system adopted and used in this study is shown in figure (3.1). The oxygen is supplied after it is separated in the OTM, methane is supplied from two ports on the walls of the reactor. The total reactor height is 0.4 m and the diameter is 0.05m in order to gain a better understanding of the system, the reactor is divided into three zones; namely Sb, Sb<sub>2</sub>O<sub>3</sub> and CO<sub>2</sub> zones. Table (3.1) lists the total volumes for each zone. At t=0 sec Sb zone contains only liquid antimony, Sb<sub>2</sub>O<sub>3</sub> zone have only liquid antimony trioxide and CO<sub>2</sub> zone contain carbon dioxide gas. Due to the density difference between antimony and antimony trioxide, 6405 kg/m<sup>3</sup> and 5000 kg/m<sup>3</sup>, respectively, antimony will settle to the bottom of the reactor. At t >0 both oxygen and methane are supplied, and heterogeneous reactions will begin. The oxygen oxidizes Sb to form Sb<sub>2</sub>O<sub>3</sub> in Sb zone. This oxidation is an exothermic process. Furthermore, the heterogeneous reduction reaction occurs when CH<sub>4</sub> reduces Sb<sub>2</sub>O<sub>3</sub> to Sb in Sb<sub>2</sub>O<sub>3</sub> zone, the reaction is endothermic. The oxidation and reduction reactions are shown in the following

reaction equations (3.1) and (3.2). Liquid metals will naturally circulate in the reactor due to density differences.

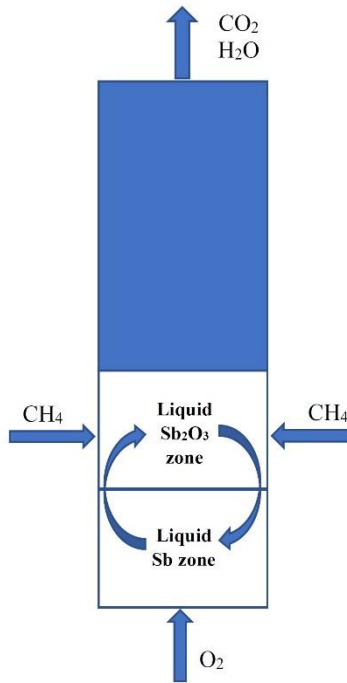
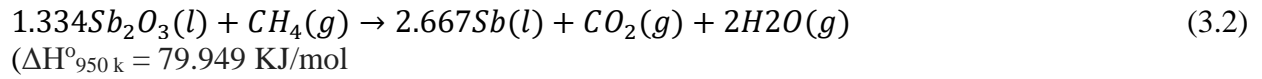


**Figure (3.1)** Reactor schematic diagram

**Table 3.1** Reactor zones volume

| Zone                           | Volume (m <sup>3</sup> ) |
|--------------------------------|--------------------------|
| Sb                             | $2.5 \times 10^{-3}$     |
| Sb <sub>2</sub> O <sub>3</sub> | $2.5 \times 10^{-3}$     |
| CO <sub>2</sub>                | $1.5 \times 10^{-2}$     |
| Total                          | $2.00 \times 10^{-2}$    |

### **3.3 Problem statement and formulation**

A two-dimensional schematic diagram of the problem under consideration is illustrated in figure (3-1). Four different oxidation and reduction ratio are considered to evaluate the temperature profiles in each zone. The reactor is also evaluated at three operation temperature,

namely, 950K, 1000K and 1050K. The minimum temperature, 950K, is considered to ensure both oxygen carriers are in liquid phase because the melting temperature for antimony and antimony trioxide are 903.7K and 929K respectively. The rest of the reactor is filled with CO<sub>2</sub> to guarantee there will be no unwanted oxidation of the fuel. For the computational purpose, two phases are considered, the gas phase and liquid phase. The gas phase is a mixture of O<sub>2</sub>, CH<sub>4</sub>, CO<sub>2</sub> and H<sub>2</sub>O, where O<sub>2</sub>, and CH<sub>4</sub> are supplied to the system and the rest are products of the reduction heterogeneous reaction. Sb and Sb<sub>2</sub>O<sub>3</sub> are a liquid mixture and represent the liquid phase. The viscosity of liquids will determine the transfer rates of Sb and Sb<sub>2</sub>O<sub>3</sub> from their point of formation of the predominant region of that species. The impact of different ratios of liquids viscosity on reactor characteristics was also assessed.

Euler-Euler approach is considered, where gas and liquid phases are treated mathematically as interpenetration continua. The volume fractions ( $\alpha_q$ ) of each phase are assumed to be a continuous function of space and time. The volume fractions represent the space occupied by each gas and liquid phase, and the conservation laws are satisfied by each phase individually, the volume of phase ( $V_q$ ) can be calculated using equation (3.3) as shown:

$$V_q = \int_V \alpha_q dV \quad (3.3)$$

Where

$$\sum_{q=1}^n \alpha_q = 1 \quad (3.4)$$

The effective density,  $\hat{\rho}_q$ , of phase q is

$$\hat{\rho}_q = \alpha_q \rho_q$$

and  $\rho_q$  is the physical density of phases q.

In this work, we have the following assumptions:

1. No mass transfer between gas and liquid phase.
2. Temperature independent gas and liquid properties, except the specific heat of gas phase mixture.
3. The fluids are incompressible, Newtonian fluid
4. No-slip condition on the walls.
5. Laminar flow model to describe gas and liquid phases.
6. Only heterogeneous reaction takes place and there is no homogeneous reaction in the system.
7. The system is adiabatic at the reactor walls.
8. Reactor walls assumed as blackbodies with internal emissivity of 1.

The above assumptions were applied to the Navier-Stokes and energy transport equations that govern the fluid motion and temperature distribution inside the reactor.

### **3.3.1 Continuity equation:**

The continuity equation for gas and liquid phases are giving by

$$\frac{\partial}{\partial t}(\alpha_g \rho_g) + \nabla(\alpha_g \rho_g \vec{v}_g) = 0 \quad (3.5)$$

$$\frac{\partial}{\partial t}(\alpha_l \rho_l) + \nabla(\alpha_l \rho_l \vec{v}_l) = 0 \quad (3.6)$$

Where  $\alpha$ ,  $\rho$  and  $\vec{v}$  are the volume fraction, the density, and velocity, respectively.

### **3.3.2 Momentum equations:**

The momentum equations for gas and liquid phase are given by:

$$\frac{\partial}{\partial t}(\alpha_g \rho_g \vec{v}_g) + \nabla(\alpha_g \rho_g \vec{v}_g \vec{v}_g) = -\alpha_g \nabla p + \nabla \cdot \bar{\tau}_g + \alpha_g \rho_g \vec{g} + \vec{R}_{lg} \quad (3.7)$$

$$\frac{\partial}{\partial t}(\alpha_l \rho_l \vec{v}_l) + \nabla(\alpha_l \rho_l \vec{v}_l \vec{v}_l) = -\alpha_l \nabla p + \nabla \cdot \bar{\tau}_l + \alpha_l \rho_l \vec{g} + \vec{R}_{lg} \quad (3.8)$$

where  $\vec{g}$  is the gravity,  $\bar{\tau}_q$  phase stress-strain tensor, and  $\vec{R}$  is the interaction force between the gas phase and liquid phase, which can be written in the following form:

$$\sum_{p=1}^n \vec{R}_{lg} = \sum_{p=1}^n \vec{K}_{lg} (\vec{v}_l - \vec{v}_g) \quad (3.9)$$

The interphase momentum coefficient depends on the friction, pressure, cohesion and other effects therefore:

$$\vec{R}_{lg} = -\vec{R}_{gl} \quad (3.10)$$

$\vec{K}_{lg}$  is the interphase momentum exchange coefficient

$$\vec{K}_{lg} = \frac{\rho_{lg} f}{6\tau_{lg}} dA_f \quad (3.11)$$

$$\tau_{lg} = \frac{\rho_{lg} d^2}{18\mu_{lg}} \quad (3.12)$$

and

$$\mu_{lg} = \alpha_l \mu_l + \alpha_g \mu_g \quad (3.13)$$

$$\rho_{lg} = \alpha_l \rho_l + \alpha_g \rho_g \quad (3.14)$$

$$Re = \frac{\rho_{lg} |v_l - v_g|}{\mu_{lg}} \quad (3.15)$$

$$f = \frac{C_D Re}{24} \quad (3.16)$$

$$C_D = 24(1 + 0.15Re^{0.687})/Re \quad (3.17)$$

where  $\mu_{lg}$ ,  $\rho_{lg}$  and  $\tau_{lg}$  are the viscosity, density and shear stress calculated from volume averaged properties.

The phase stress-strain tensor is expressed as

$$\bar{\tau}_g = \alpha_g \mu_g (\nabla \vec{v}_g + \nabla \vec{v}_g^T) + \alpha_g \left( \lambda_g - \frac{2}{3} \mu_g \right) \nabla \cdot \vec{v}_g \bar{I} \quad (3.18)$$

$$\bar{\tau}_l = \alpha_l \mu_l (\nabla \vec{v}_l + \nabla \vec{v}_l^T) + \alpha_l \left( \lambda_l - \frac{2}{3} \mu_l \right) \nabla \cdot \vec{v}_l \bar{I} \quad (3.19)$$

Here  $\mu_g, \mu_l, \lambda_g, \lambda_l$  are the shear and bulk viscosity of gas and liquid phase.

### **3.3.4 Energy conservation equation:**

To describe the conservation of energy in Eulerian multiphase applications, a separate enthalpy equation can be written for each phase:

$$\frac{\partial}{\partial t}(\alpha_g \rho_g h_g) + \nabla \cdot (\alpha_g \rho_g \vec{u} h_g) = \alpha_g \frac{\partial P_g}{\partial t} + \bar{\tau}_g : \nabla \vec{u}_g - \nabla \cdot \vec{q}_g + Q_{lg} + S_g \quad (3.20)$$

$$\frac{\partial}{\partial t}(\alpha_l \rho_l h_l) + \nabla \cdot (\alpha_l \rho_l \vec{u} h_l) = \alpha_l \frac{\partial P_l}{\partial t} + \bar{\tau}_l : \nabla \vec{u}_l - \nabla \cdot \vec{q}_l + Q_{gl} + S_l \quad (3.21)$$

$h_g, h_l$  are the specific enthalpy gas and liquid phases,  $\vec{q}_g, \vec{q}_l$  are the heat flux and  $Q_{lg}, Q_{gl}$  are the intensity of the heat exchange between the gas and liquid phases.  $S_g, S_l$  are the heat source of chemical reaction and radiation in case radiation is considered for gas and liquid phases.

Where

$$Q_{lg} = -Q_{gl} \quad (3.22)$$

and

$$Q_{lg} = \bar{h}_{lg} A_f (T_l - T_g) \quad (3.23)$$

$$\bar{h}_{lg} = \bar{h}_{gl} \quad (3.24)$$

is the volumetric heat transfer coefficient between the liquid and the gas phase.

$$\bar{h}_{lg} = \frac{k_g Nu_g}{d} \quad (3.25)$$

Here  $k_g$  is the thermal conductivity of gas phase,  $d$  is the bubble diameter.

$$Nu = 2.0 + 0.15 Re^{0.8} Pr^{0.5} \quad (3.26)$$

The interfacial area concentration is defined as the interfacial area between gas and liquid phases per unit mixture volume.

$$A_f = \frac{6\alpha(1-\alpha)}{d} \quad (3.27)$$

The heat source of chemical reaction ( $S_c$ ) in gas and liquid phase can be calculated by

$$S_c = -\sum_i \frac{\dot{h}_i}{M_i} R_i \quad (3.28)$$

Where  $\dot{h}_i$  is the enthalpy of formation of species i,  $R_i$  is the reaction rate of species i and  $M_i$  is the molecular weight of species i in each gas and liquid phases.

In the case where the radiation effect is considered the  $S_g$ ,  $S_l$  heat sources in the energy equation will equal the heat source from chemical reaction ( $S_c$ ) plus heat transfer due to radiation ( $S_r$ ), the radiation model was assumed to be gray radiation, which radiation incident is a function for temperature only as shown below:

$$q_r = -\frac{1}{(3(a+\sigma_s)-C\sigma_s)} \nabla G \quad (3.29)$$

Where  $q_r$ ,  $a$ ,  $\sigma_s$ ,  $\nabla G$  and  $C$  are radiation flux, absorption coefficient, scattering coefficient, incident radiation and the linear-anisotropic phase function coefficient respectively.  $C$  is a property of the fluid. It is assumed to be isotropic scattering, mean scattering is equally likely in all directions, which mean value is define a zero.

$$\Gamma = \frac{1}{(3(a+\sigma_s)-C\sigma_s)} \quad (3.30)$$

$$q_r = -\Gamma \nabla G \quad (3.31)$$

The transport equation for  $G$  is

$$\nabla \cdot (\Gamma \nabla G) - aG + 4an^2\sigma T^4 = S_r \quad (3.32)$$

Where  $n$  is refractive index of the medium,  $\sigma$  is the Stefan-Boltzmann constant and the ( $S_r$ ) is the radiation source which is equal

$$-\nabla \cdot q_r = S_r = aG - 4an^2\sigma T^4 \quad (3.33)$$

### 3.3.5 Species transport Equations

The gas phase is assumed to be a mixture of 4 species, represented as follows: O<sub>2</sub>, CH<sub>4</sub>, CO<sub>2</sub> and H<sub>2</sub>O. The liquid phase is a mixture of 2 species Sb and Sb<sub>2</sub>O<sub>3</sub>. In this work, the transport equations of species take the general form:

$$\frac{\partial}{\partial t} (\rho_g \alpha_g Y_{g,i}) + \nabla \cdot (\rho_g \alpha_g \vec{v}_g Y_{g,i}) = -\nabla \cdot \alpha_g \vec{J}_{g,i} + \alpha_g X_{g,i} + H_i \quad (3.34)$$

$$\frac{\partial}{\partial t} (\rho_l \alpha_l Y_{l,i}) + \nabla \cdot (\rho_l \alpha_l \vec{v}_l Y_{l,i}) = -\nabla \cdot \alpha_l \vec{J}_{l,i} + \alpha_l X_{l,i} + H_i \quad (3.35)$$

Where  $\vec{J}_{g,i}$  and  $\vec{J}_{l,i}$  are the diffusion flux of species *i* in the gas and liquid mixture.  $H_i$  is the heterogeneous reaction rate in species *i*.  $X_{g,i}$  and  $X_{l,i}$  are the mass source for gas and liquid phases. Diffusion flux for each phase is calculated as:

$$\vec{J}_{g,i} = -\rho_g D_{M,i} \nabla \cdot Y_{g,i} - D_{T,i} \frac{\nabla T}{T} \quad (3.36)$$

$$\vec{J}_{l,i} = -\rho_l D_{M,i} \nabla \cdot Y_{l,i} - D_{T,i} \frac{\nabla T}{T} \quad (3.37)$$

Here  $D_{M,i}$  is the mass diffusion coefficient for species *i* in the mixture, which set to  $2.88 \times 10^{-5}$  (m<sup>2</sup>/s) and  $D_T$  is the thermal diffusion coefficient, which is neglected because the full multicomponent diffusion model is not considered. The mass sources for gas and liquid can be written as:

$$X_{ri} = -R \sum_{ri} \gamma_j^r M_j^{ri} \quad (3.38)$$

$$X_{pi} = R \sum_{pi} \gamma_j^p M_j^{pi} \quad (3.39)$$

The mass source for gas and liquid is

$$X = X_{pi} + X_{ri} \quad (3.40)$$

Where  $\gamma$  the stoichiometric coefficient,  $pi$  is represent the product, and  $ri$  represent the reactant.

### **3.3.6 Thermo-physical properties**

The thermo-physical properties of both gas mixture and liquid mixture are listed in Table (3.2). The properties such as density, thermal conductivity, heat capacity and viscosity for both gas and liquid phase's mixture are evaluated based on the mass fraction of each mixture as shown in equation (3.41), (3.42), (3.43) and (3.44). Since a more realistic temperature field can be obtained by increasing the specific heat capacity for each species [119, 120] as the reactor temperature increases, therefore the specific heat of the gas phase mixture are set to be a polynomial function with temperature as shown in equation (3.45), the constants for each equation listed in the table (3.3).

The temperature dependence of the thermal conductivity of liquid Sb and Sb<sub>2</sub>O<sub>3</sub> are not available in the literature, and, therefore weighted average based on solid phase was employed. Similar mathematical treatment was applied for the estimation of Sb<sub>2</sub>O<sub>3</sub> density and viscosity.

$$\rho_m = \frac{1}{\sum_i \frac{Y_i}{\rho_i}} \quad (3.41)$$

$$k_m = \sum_i Y_i k_i \quad (3.42)$$

$$\mu_m = \sum_i Y_i \mu_i \quad (3.43)$$

$$Cp_m = \sum_i Y_i Cp_i \quad (3.44)$$

where  $\rho_m$ ,  $k_m$ ,  $\mu_m$  and  $Cp_m$  are mixture density, thermal conductivity, viscosity and heat capacity respectively,  $Y_i$  is mass fraction and (i) denoted to species.

$$Cp(T) = A_1 + A_2T + A_3T^2 + A_4T^3 + A_5T^4 + A_6T^5 + A_7T^6 \quad (3.45)$$

**Table (3.2)** Material thermo-physical properties

| Property                             | O <sub>2</sub>        | CH <sub>4</sub>       | CO <sub>2</sub>       | H <sub>2</sub> O      | Sb liquid             | Sb <sub>2</sub> O <sub>3</sub> liquid |
|--------------------------------------|-----------------------|-----------------------|-----------------------|-----------------------|-----------------------|---------------------------------------|
| Density (kg/m <sup>3</sup> )         | 0.3848                | 0.3087                | 0.5292                | 0.2167                | 6405                  | 5000                                  |
| Cp (J/kg.k)                          | -                     | -                     | -                     | -                     | 257.764               | 517.0321                              |
| Thermal conductivity (w/m.k)         | 0.07155               | 0.08711               | 0.07049               | 0.09707               | 30                    | 24                                    |
| Viscosity (kg/m.s)                   | 4.91×10 <sup>-5</sup> | 1.97×10 <sup>-5</sup> | 4.13×10 <sup>-5</sup> | 3.76×10 <sup>-5</sup> | 1.19×10 <sup>-3</sup> | 1.19×10 <sup>-3</sup>                 |
| Molecular weight (kg/kmol)           | 31.9988               | 16.04303              | 44.00995              | 18.01534              | 121.75                | 291.5                                 |
| Standard state Enthalpy (J/kmol)     | 0                     | 7.49×10 <sup>7</sup>  | -3.94×10 <sup>8</sup> | 2.42×10 <sup>8</sup>  | 1.75×10 <sup>7</sup>  | 7.09×10 <sup>8</sup>                  |
| Standard state Entropy (J/kmol.k)    | 205026.9              | 186040.1              | 213720.2              | 188696.4              | 62710                 | 123009.6                              |
| Reference Temperature (k)            | 298.15                | 298.15                | 298.15                | 298.15                | 298.15                | 298.15                                |
| L-J Characteristic length (angstrom) | 3.458                 | 3.758                 | 3.941                 | 2.605                 | -                     | -                                     |
| L-J Energy parameter (K)             | 107.4                 | 148.6                 | 195.2                 | 572.4                 | -                     | -                                     |

**Table (3.3)** Gas specific heat constant

| Cp constant    | O <sub>2</sub>             | CH <sub>4</sub>           | CO <sub>2</sub>           | H <sub>2</sub> O          |
|----------------|----------------------------|---------------------------|---------------------------|---------------------------|
| A <sub>1</sub> | 8.76317×10 <sup>2</sup>    | 2005                      | 5.35446×10 <sup>2</sup>   | 1.93780×10 <sup>3</sup>   |
| A <sub>2</sub> | 1.22828×10 <sup>-1</sup>   | -6.81428×10 <sup>-1</sup> | 1.27867                   | -1.18077                  |
| A <sub>3</sub> | 5.58304×10 <sup>-4</sup>   | 7.08589×10 <sup>-3</sup>  | -5.46776×10 <sup>-4</sup> | 3.64357×10 <sup>-3</sup>  |
| A <sub>4</sub> | -1.20247×10 <sup>-6</sup>  | -4.71368×10 <sup>-6</sup> | -2.38224×10 <sup>-7</sup> | -2.86327×10 <sup>-6</sup> |
| A <sub>5</sub> | 1.14741×10 <sup>-9</sup>   | 8.51317×10 <sup>-10</sup> | 1.89204×10 <sup>-10</sup> | 7.59578×10 <sup>-10</sup> |
| A <sub>6</sub> | -5.12377×10 <sup>-13</sup> | -                         | -                         | -                         |
| A <sub>7</sub> | 8.56597×10 <sup>-17</sup>  | -                         | -                         | -                         |
|                |                            |                           |                           |                           |

### **3.4 Numerical procedures**

The numerical simulation was done using the CFD software FLUENT 19.1, utilizing multiphase Eulerian transient flow with two heterogeneous reactions, oxidation and reduction.

The pressure based solution is selected, which is recommended for incompressible flow [121] where the pressure field is obtained by manipulating continuity and momentum equations. Fluent solved the governing integral equations (3.5), (3.6), (3.7), (3.8), (3.20), (3.21), (3.34) and (3.35) based on control-volume-based techniques. The domain is divided into discrete control volume and integration of the governing equations on the individual control volumes was employed to calculate the discrete dependent variable such as velocities, pressure, temperature and other conserved scalars. The coupled algorithm is used to solve all equations for phase velocity corrections and shared pressure correction simultaneously, thus offer improved convergence, but required more memory compared with other methods [122]. The implicit scheme is considered over explicit for time discretization, due to the significant larger time steps that can be used without a decrease of simulation stability. Due to laminar flow and the mesh cell is quadrilateral the first order upwind accuracy spatial securitization is selected. Mesh refinement was applied for all the zones to achieve better mesh quality.

A set of user-defined functions (UDFs) was written in C to calculate the heterogeneous reaction rate of oxidation and reduction, to describe the reactions in the system. These UDFs were compiled and linked to the code throughout the simulation runs. Convergence criteria to terminate iteration ( $R^\varphi$ ) in this study is set as  $10^{-4}$  for continuity equations,  $10^{-3}$  for volume of fraction and  $10^{-6}$  for the energy equation. The default convergence criterion in FLUENT required that the global scaled residual be defined by the following equation:

$$R^\varphi = \frac{\sum_{cellsP} |\sum_{nb} a_{nb} \varphi_{nb} + b - a_p \varphi_p|}{\sum_{cellsP} |a_p \varphi_p|} \quad (3.46)$$

Here  $\varphi_p$  is general variable at a cell p,  $a_p$  is the center coefficient,  $a_{nb}$  are the influence coefficients for the neighboring cells, and b is the contribution of the constant part of the source term  $S_c$  [123]

To ensure grid independent result, three different grid sizes (N=3850 with total cell size 2.3 mm, N=8778 with cell size 1.5mm and N=20000 with cell size 1mm) were evaluated for discretization the computational domain. A grid size of N=3850 was selected to reduce the total time required for simulation for the same results as shown in figure (3.2a) and (3.2b).

Furthermore, three different time steps ( $\Delta t=0.001$ , 0.0005 and 0.0001 sec) were tested for integrating time derivatives. A time step of 0.001 sec was found sufficient to keep solution independent, stable and save time in the simulation process as seen in figure (3.3a) and (3.3b).

The under-relaxation factors for pressure, momentum, energy, and volume of fraction were 0.6, 0.6, 0.95 and 0.5 respectively.

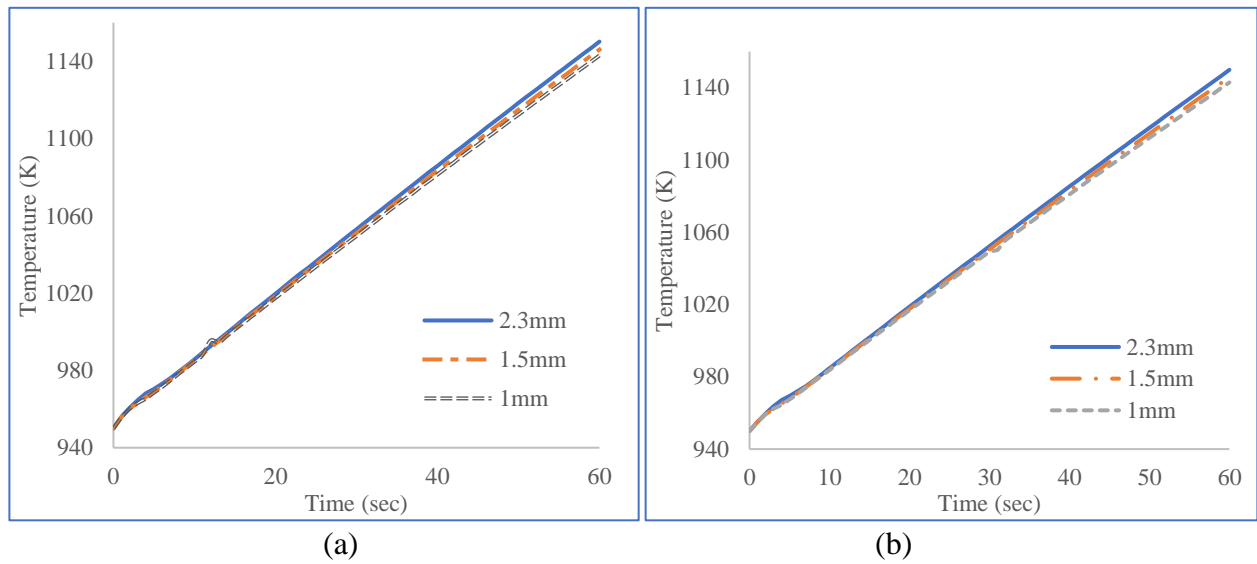


**Figure (3.2)** Effect of grid size on (a) net gas temperature (b) net liquid temperature verses reaction time

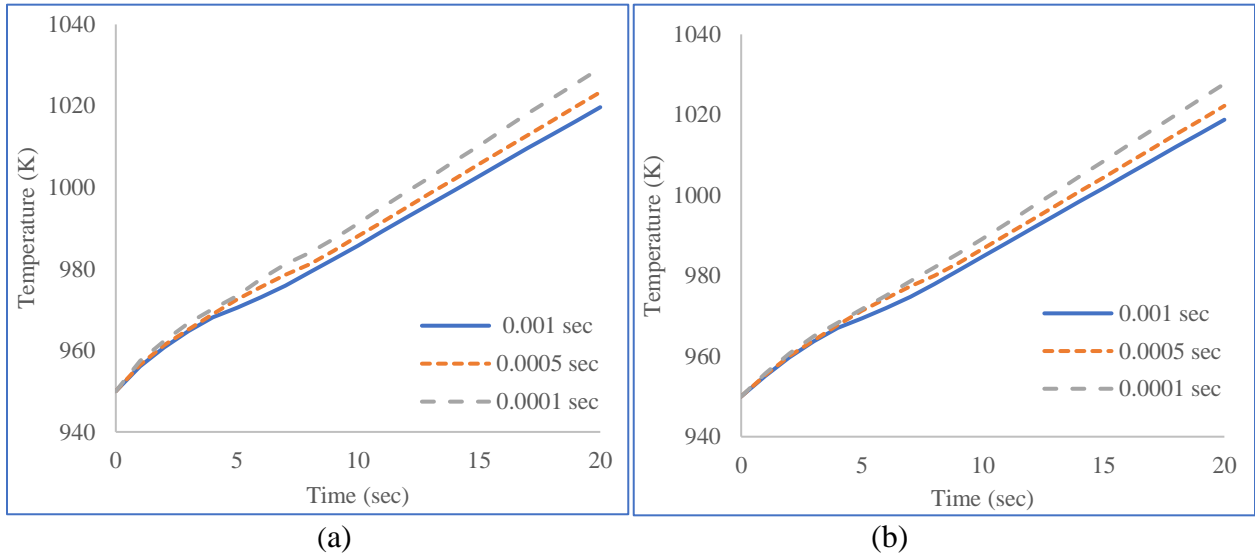


**Figure (3.3)** Effect of time step on (a) net gas temperature (b) net liquid temperature verses reaction time

## CHAPTER 4

### RESULT AND DISCUSSION

#### 4.1 Oxygen carrier selection

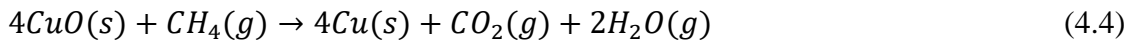
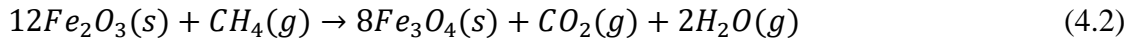
The optimum temperature for gas turbine and heat recovery steam cycle is around 1200°C, which consider a higher operating temperature for solid particles. In order to avoid agglomeration and softening, solid particle is always operating at a lower temperature (1000°C) depending on the properties of metal is used [124]. This is considered a major hurdle for using solid particles in the CLC. Therefore, liquid metals may be used as an intermediate oxygen carrier instead of solid particles to overcome such a problem. Liquid metals have greater oxygen transferred between the oxidation and reduction in the liquid chemical looping reactors[111]. Such replacement will bring other challenging such as higher temperature operation system to maintain the liquid metal, therefore choosing the right metal plays a key role in this process. In this section, several metals and metal oxides, are investigated based on the thermodynamic potential using HSC chemistry 5.1 software to demonstrate the Gibbs free energy and enthalpy of reaction with respect to operating temperature. Table 4-1 contains data on the melting point, boiling point and density of Sb, Sb<sub>2</sub>O<sub>3</sub>, Pb, PbO, Cu, CuO, Fe<sub>2</sub>O<sub>3</sub> and Fe<sub>3</sub>O<sub>4</sub>.

**Table (4.1)** properties of antimony, lead, copper and Iron oxides

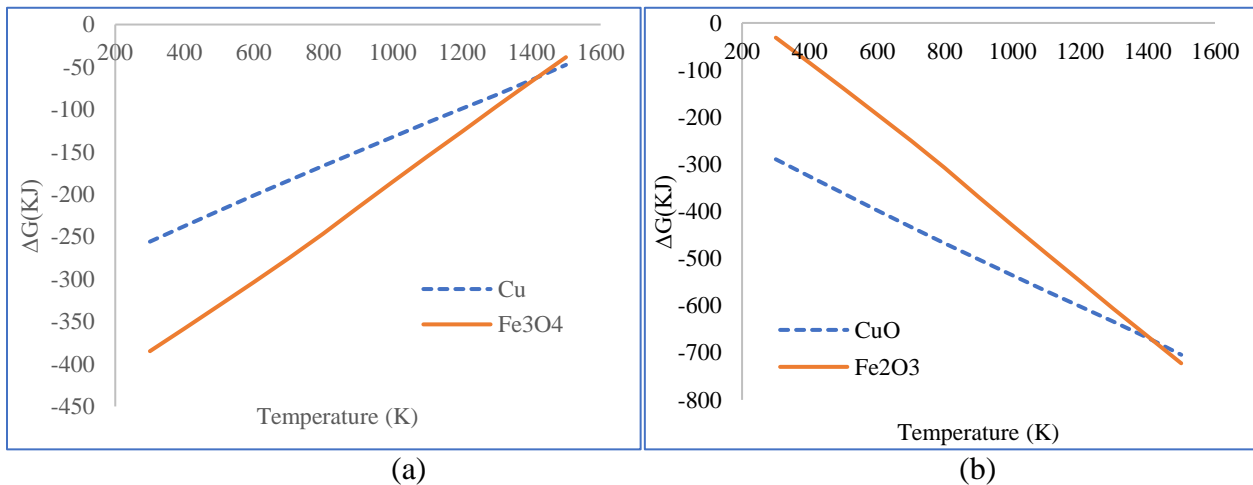
| Metal                          | Melting point (K) | Boiling point (K) | Density (kg.m <sup>-3</sup> ) |
|--------------------------------|-------------------|-------------------|-------------------------------|
| Sb                             | 904               | 1860              | 6684                          |
| Sb <sub>2</sub> O <sub>3</sub> | 928               | 1698              | 5580                          |
| Pb                             | 600.6             | 2022              | 11344                         |
| PbO                            | 1160              | 1808              | 9530                          |
| Cu                             | 1357.77           | 2835              | 8960                          |
| CuO                            | 1719              | 2270              | 6300                          |
| Fe <sub>2</sub> O <sub>3</sub> | 1838              | Decompose         | 5240                          |
| Fe <sub>3</sub> O <sub>4</sub> | 1870              | 2896              | 5170                          |

The high melting temperature for Fe<sub>2</sub>O<sub>3</sub> and Fe<sub>3</sub>O<sub>4</sub> make the reactor operation expensive and the risk associated with handling molten liquid is higher than other metals. Cu and CuO have

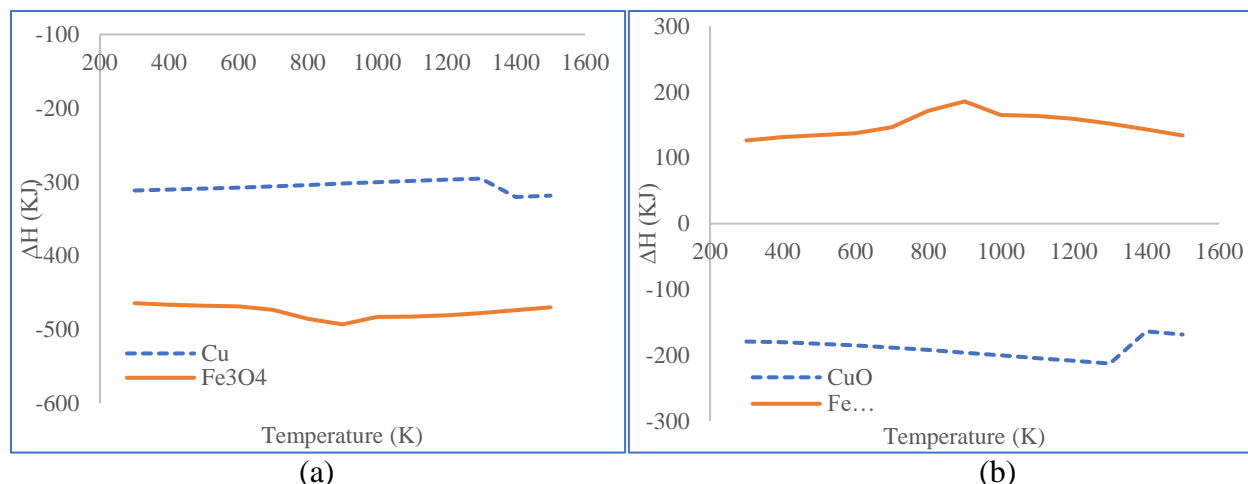
a large difference between their melting points which may lead to metal oxide solidification. Therefore, Cu, CuO, Fe<sub>2</sub>O<sub>3</sub>, and Fe<sub>3</sub>O<sub>4</sub> are preferred to be used as a solid oxygen carrier in the chemical looping process and be oxidized and reduced in separate reactors. The oxidation and reduction process are described in Equation (4.1), (4.2), (4.3) and (4.4).



Both oxidation and reduction reactions have negative Gibbs free energy with respect to temperature, but the Gibbs free energy for oxidation reactions increases with temperature while those for reduction become more negative, as shown in Figure (4.1a) and (4.1b). The enthalpy change from oxidation and reduction are negative values, which mean exothermic reactions with a wide range of operating temperatures except for the reduction reaction shown in equation (4.2) where the reaction is endothermic as shown in figure (4.2a) and (4.2b).

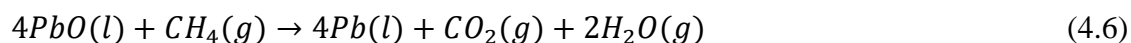


**Figure (4.1)** Gibbs free energy with operating temperature (a) oxidation (b) reduction



**Figure (4.2)** Enthalpy of reaction with operation temperature (a) oxidation reaction (b) reduction reaction

Sb, Sb<sub>2</sub>O<sub>3</sub>, Pb, and PbO have lower melting points and higher boiling temperature, which make them suitable to the LCLC. Lead and lead oxide can be oxidized and reduced using methane gas in equilibrium as shown in equation (4.5) and (4.6). Meanwhile, figure (4.3a) and (4.3b) are the change in the Gibbs free energy and enthalpy due to the redox reactions of lead. It is seen in the figures that negative Gibbs free energy for both oxidation and reduction and exothermic reactions for oxidation and reduction. However, lead has a lower melting point compared to the lead oxide, which may lead to complications of oxide solidification. The Another redox couple, Sn and SnO<sub>2</sub> also have similar issues related to the wide difference between melting points of the metal and metal oxide.



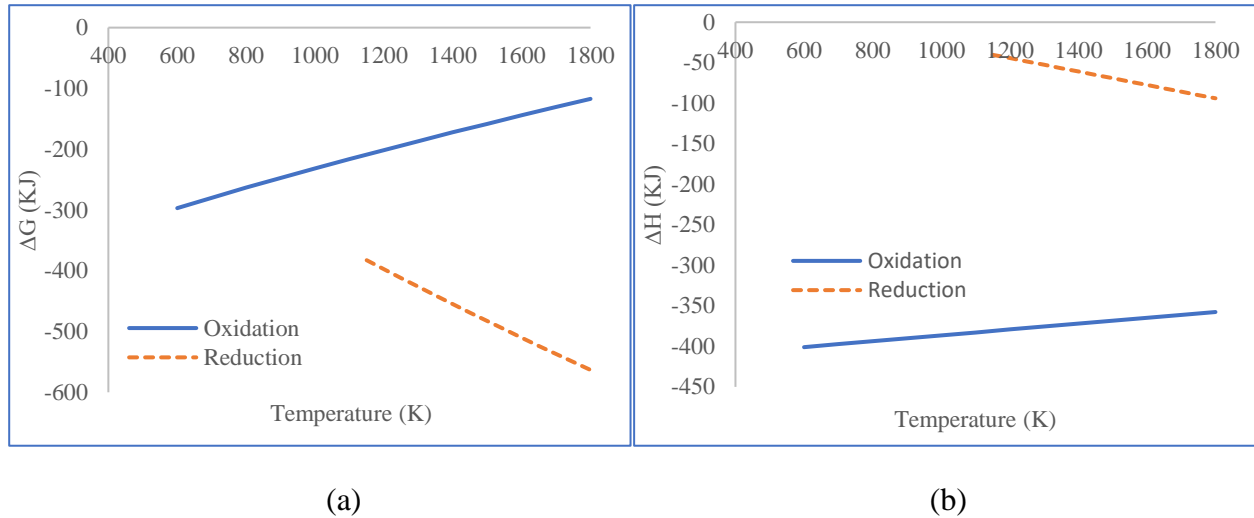


**Figure (4.3)** Lead and lead oxide oxidation and reduction (a) Gibbs free energy (b) enthalpy of reaction with wide operation temperature

Antimony and antimony trioxide have a good potential to serve over a wide temperature range as oxygen carrier due to lower and similar melting point for both Sb and  $Sb_2O_3$ . Antimony and antimony trioxide can be oxidized with pure oxygen and reduced using methane gas as shown in Equation (3.1) and (3.2). Figure (4.4a) contains the plots of the Gibbs free energy change during the oxidation and reduction reactions with pure oxygen and methane, respectively. As observed in the figure, the Gibbs free energy for both reactions are negative over the temperature range is shown. This means that both reactions are spontaneous for a wide range of temperature. Figure (4.4b) contains the plots of the change in enthalpy ( $\Delta H$ ) for oxidation and reduction reactions. In the case of the oxidation reaction, the change in enthalpy is negative throughout the selected temperature range, although it is found to increase with temperature. In the case of the reduction reaction with  $CH_4$ , the reaction is endothermic and the change in enthalpy is found to decrease with temperature. As compared to the lead-based system, antimony-antimony trioxide redox system released a larger amount of heat. The energy balance released from the oxidation and reduction of Sb and  $Sb_2O_3$  with 1kmol of  $CH_4$  and 1kmol of  $O_2$

is 425.85MJ at 950K Figure (4.5) show total energy balance with a wide range of operating temperature. The higher net heat generation from the redox couple as well as the lower and closer melting points between the oxidative and reductive states, antimony-antimony trioxide redox couple is found to better suit liquid carrier-based looping.

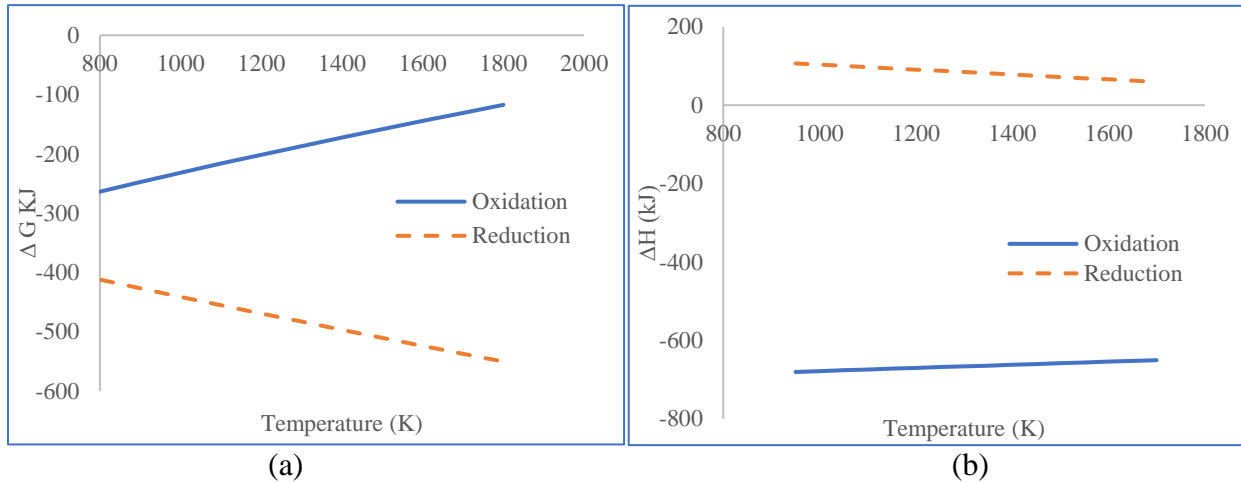


**Figure (4.4)** Antimony and antimony trioxide oxidation and reduction (a) Gibbs free energy (b) enthalpy of reaction with wide operation temperature

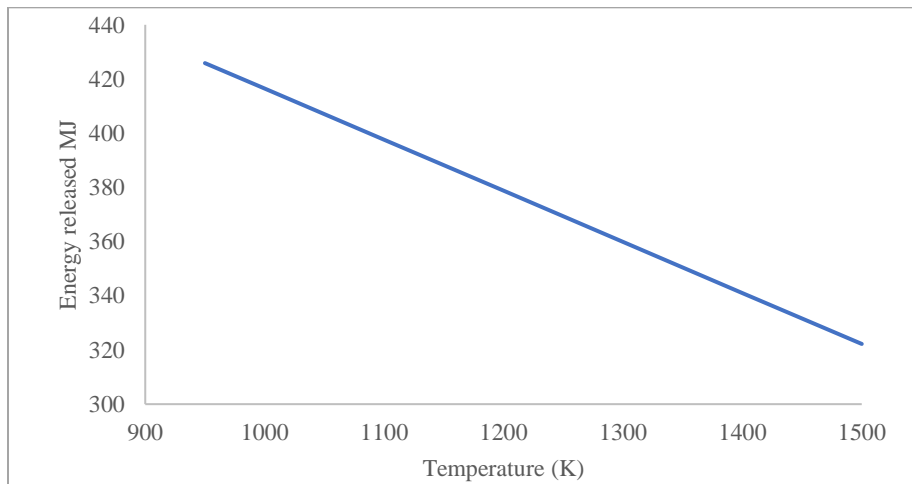


**Figure (4.5)** Energy balance for antimony and antimony trioxide reaction

## **4.2 Oxidation and reduction effect based on experimental data**

According to the experimental data conducted by Sims [125], yttrium and zirconium co-doped cerium oxide is a promising material as an oxygen transport membrane (OTM) with the potential to maximize the oxygen flux in future. Table (4.2) contains data on the oxygen flux through the membrane along with the maximum oxygen addition and removal rates from Sb and Sb<sub>2</sub>O<sub>3</sub> metals obtained in a laboratory. These data were used during the simulation to determine and predict the temperature profile in the reactor. The reactor areas for oxygen pickup and release are 500cm<sup>2</sup> and 400cm<sup>2</sup>, respectively. The total volumetric oxygen and methane flow rate enter the reactor were calculated to be 0.0195 m<sup>3</sup>/s.m<sup>2</sup> and 0.0007247 m<sup>3</sup>/s.m<sup>2</sup> respectively. Based on the condition of complete consumption of oxygen and methane in the reactor, the oxidation and reduction rate can be calculated and the ratio will be 21.02 as shown in the table (4.3).

**Table (4.2)** Sims experimental data

|                                                                                   |                          |
|-----------------------------------------------------------------------------------|--------------------------|
| Max oxygen transport (Through Membrane; (mol/s.cm <sup>2</sup> ))                 | 3.67067×10 <sup>-7</sup> |
| Max oxygen Addition (To Sb; mol/s.cm <sup>2</sup> )                               | 3.127×10 <sup>-5</sup>   |
| Max oxygen Removal (From Sb <sub>2</sub> O <sub>3</sub> ; mol/s.cm <sup>2</sup> ) | 1.859×10 <sup>-6</sup>   |

**Table (4.3)** Simulation data

| Inlet                       | Volumetric flow (m <sup>3</sup> /m <sup>2</sup> .s) | Area (m <sup>2</sup> ) | Molar flow rate (kmol/s)  | Ratio=O <sub>2</sub> molar flow rate/CH <sub>4</sub> molar flow rate |
|-----------------------------|-----------------------------------------------------|------------------------|---------------------------|----------------------------------------------------------------------|
| O <sub>2</sub> inlet        | 0.0195                                              | 0.05                   | 1.172625×10 <sup>-5</sup> | 21.02                                                                |
| CH <sub>4</sub> inlet 1     | 0.0007247                                           | 0.02                   | 2.7892×10 <sup>-7</sup>   |                                                                      |
| CH <sub>4</sub> inlet 2     | 0.0007247                                           | 0.02                   | 2.7892×10 <sup>-7</sup>   |                                                                      |
| Total CH <sub>4</sub> inlet | 0.0007247                                           | 0.04                   | 5.5784×10 <sup>-7</sup>   |                                                                      |

The initial temperature for liquid antimony and antimony trioxide are 950K which is the same temperature of gases enter the reactor. This temperature is selected because it is above the melting point of liquid metal and metal oxide and ensures no solidification occurs. The temperature in both gas and liquid phase with respect to time are shown in figures (4.6a) and (4.6b). According to the figures, the net temperature for both gas and liquid phase increases with respect to time. The temperature in Sb zone increases first due to the exothermic nature of the oxidation reaction. Due to density differences,  $Sb_2O_3$  start to rise upward to the adjacent zones until it reaches the  $Sb_2O_3$  dominant zone. In the  $Sb_2O_3$  zone, the endothermic reduction reaction produces cooler Sb which sinks downwards to lower zones. The upward motion of  $Sb_2O_3$  and the downward mobility of the Sb creates an internal circulation, which enhances the convective heat transfer between the zones along with the natural separation of the oxidized and reduced carrier. Figure (4.7) shows the temperature contours for the reactor zones in both gas and liquid phase.

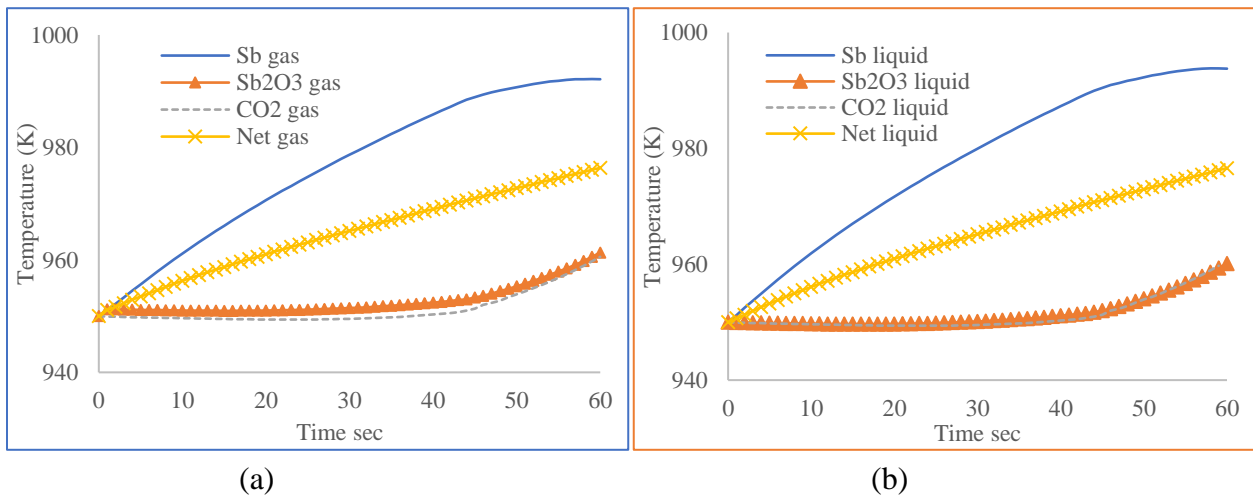


**Figure (4.6)** Temperature distribution of gas and liquid phases in each reactor zone Sims case (a) gas phase (b) liquid phase

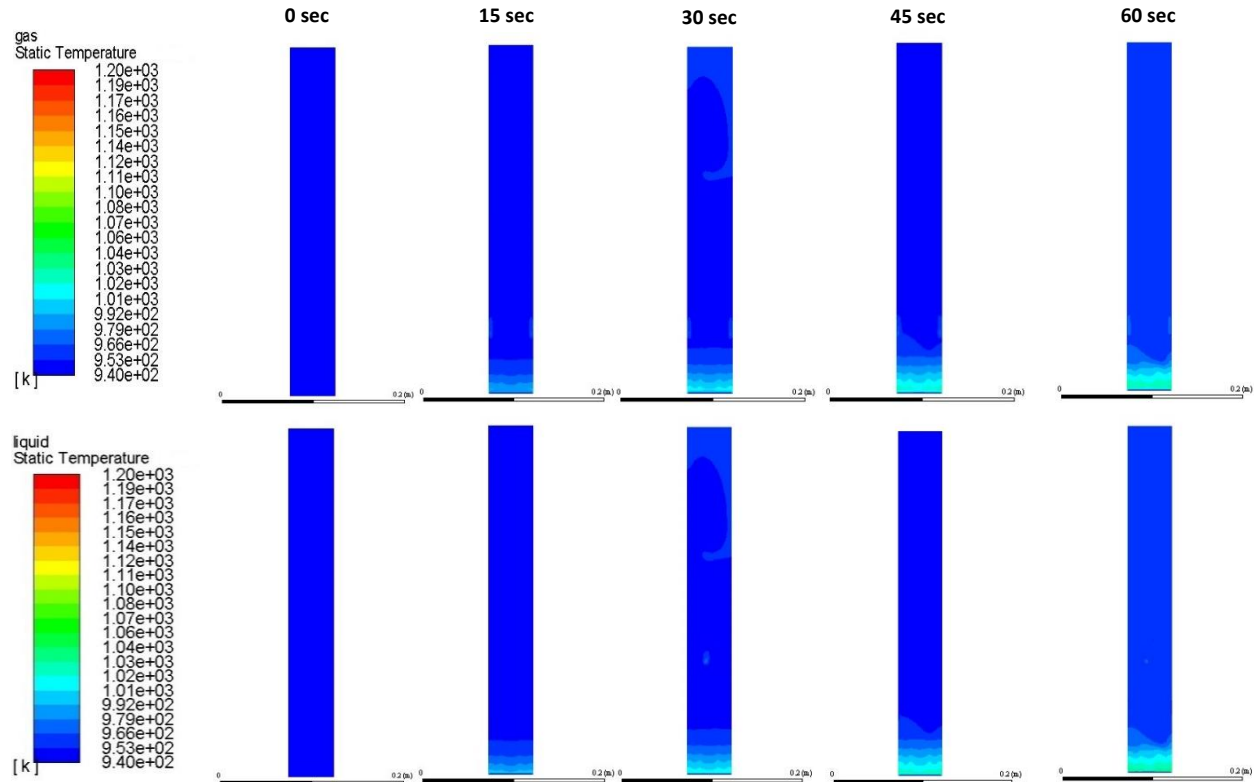


**Figure (4.7)** Temperature contour of gas and liquid phases in the reactor zones based on experimentally validated case [11]

The Sb and  $Sb_2O_3$  concentration also change with respect to time due to the oxidation and reduction process where Sb is forming in the  $Sb_2O_3$  zone and  $Sb_2O_3$  in the Sb zone. At  $t=0$  Sb molar concentration in Sb zone is  $52.608 \text{ kmol m}^{-3}\text{s}^{-1}$  and  $Sb_2O_3$  molar concentration in  $Sb_2O_3$  zone is  $17.154 \text{ kmol m}^{-3}\text{s}^{-1}$ . At  $t > 0$ , the concentration changes with time till  $t= 45\text{sec}$ . Please note that the software cannot track each particle because they are mixed and particle tracking is not applied since it is a time expensive process. Thus, we are focusing more on the temperature profiles in each zone, the concentration for both Sb and  $Sb_2O_3$  inside the reactor shown in figure (4.8).

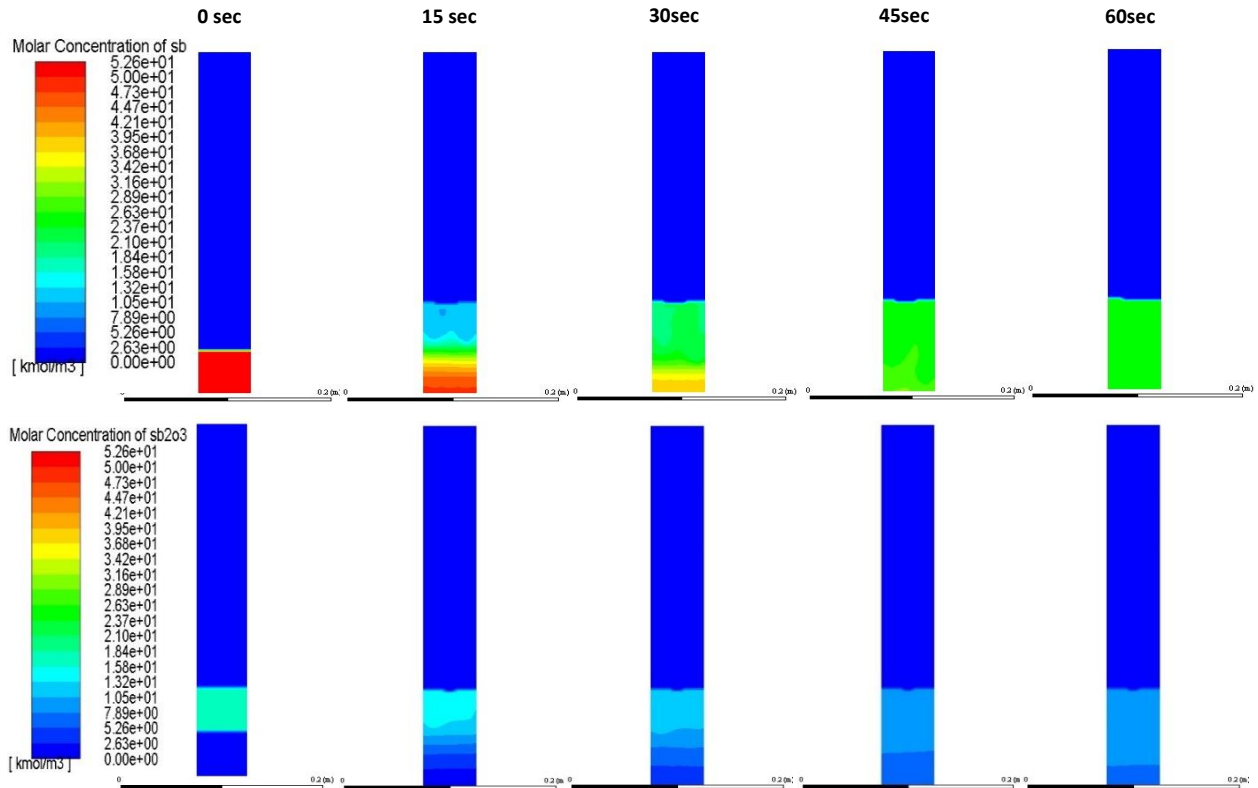


**Figure (4.8)** Sb and Sb<sub>2</sub>O<sub>3</sub> molar concentration with respect to time

Volume fractions for each phase are shown in figure (4.9) where the gas occupied the CO<sub>2</sub> zone and the liquid will mainly occupy the Sb and Sb<sub>2</sub>O<sub>3</sub> zones. O<sub>2</sub> and CH<sub>4</sub> are entering these zones, but they will react completely to oxidize and reduce liquid metals.

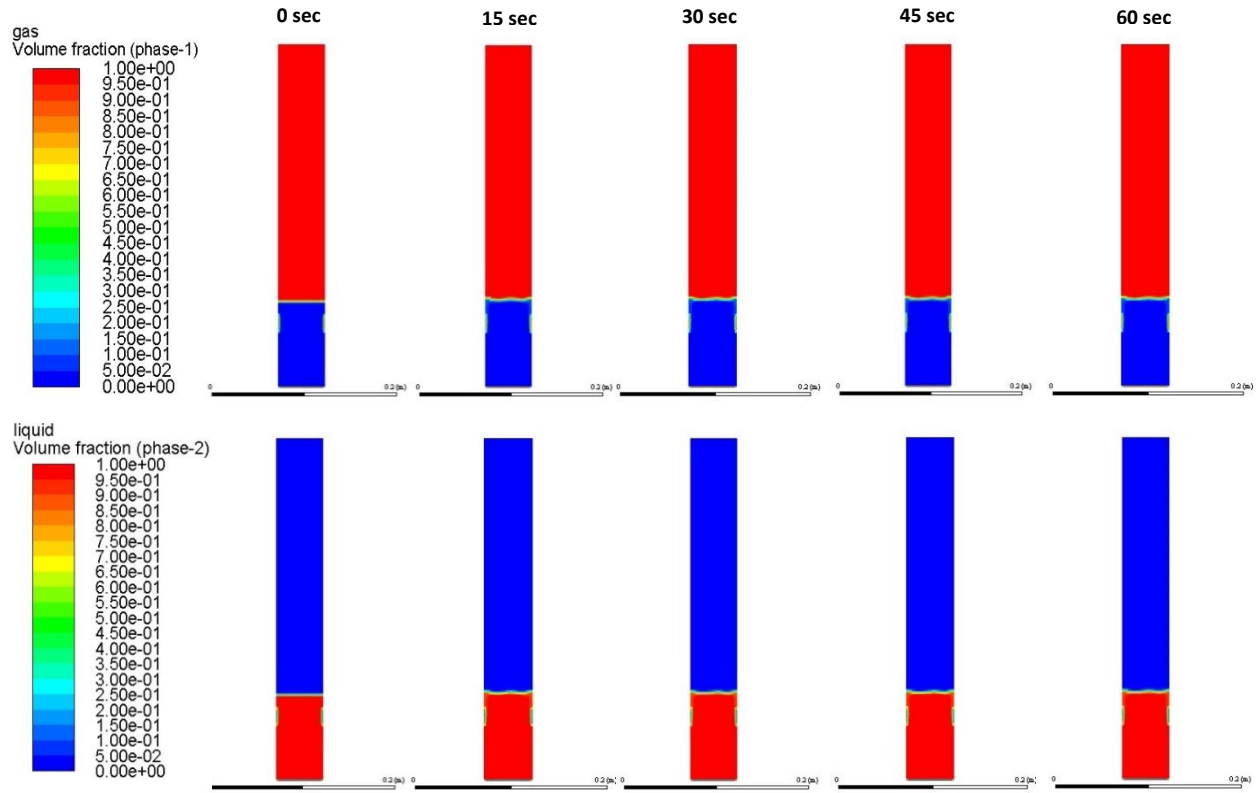


**Figure (4.9)** Gas and liquid volume fraction with respect to time

The mass fraction of  $O_2$  and  $CH_4$  distribution in the reactor is shown in figure (4.10) where all the inlet gases are consumed during the reaction and nothing will remain in the reactor. Figure (4.11) shows the mass fraction of  $CO_2$  and  $H_2O$ . The  $CO_2$  mass fraction value is 1 in the  $CO_2$  zone because this zone is full of the gas at  $t=0$ . This value decreases as the reaction progresses and more  $H_2O$  vapor is released. The  $H_2O$  vapor is not present in the reactor at  $t=0$ . However, its value increases with respect to time because of more  $H_2O$  vapor released as a result of the reduction reaction in the  $Sb_2O_3$  zone where the water vapor is produced and rises to  $CO_2$  zone and tries to leave through the reactor outlet. The mass fraction of  $H_2O$  inside  $Sb$  and  $Sb_2O_3$  zones is calculated to be equal to 1. This does not happen in the real case. The reason for this anomalous result is related to ANSYS FLUENT gas mixture species order. The order for the gas phase mixture in the current case under investigated is  $O_2$ ,  $CH_4$ ,  $CO_2$  and  $H_2O$ , FLUENT

consider the last species in the list to be the bulk and the most abundant species. This, along with the very low volume fraction of the gas phase in the Sb and Sb<sub>2</sub>O<sub>3</sub> zone compared to CO<sub>2</sub> zone figure (4.9), caused FLUENT to represent all the regions that contain lower gas mass fraction with the abundant species which is H<sub>2</sub>O. Figure (4.12) shows the mole of H<sub>2</sub>O vapor in each zone, which is really close to zero for Sb and Sb<sub>2</sub>O<sub>3</sub> and higher values at CO<sub>2</sub> zone.

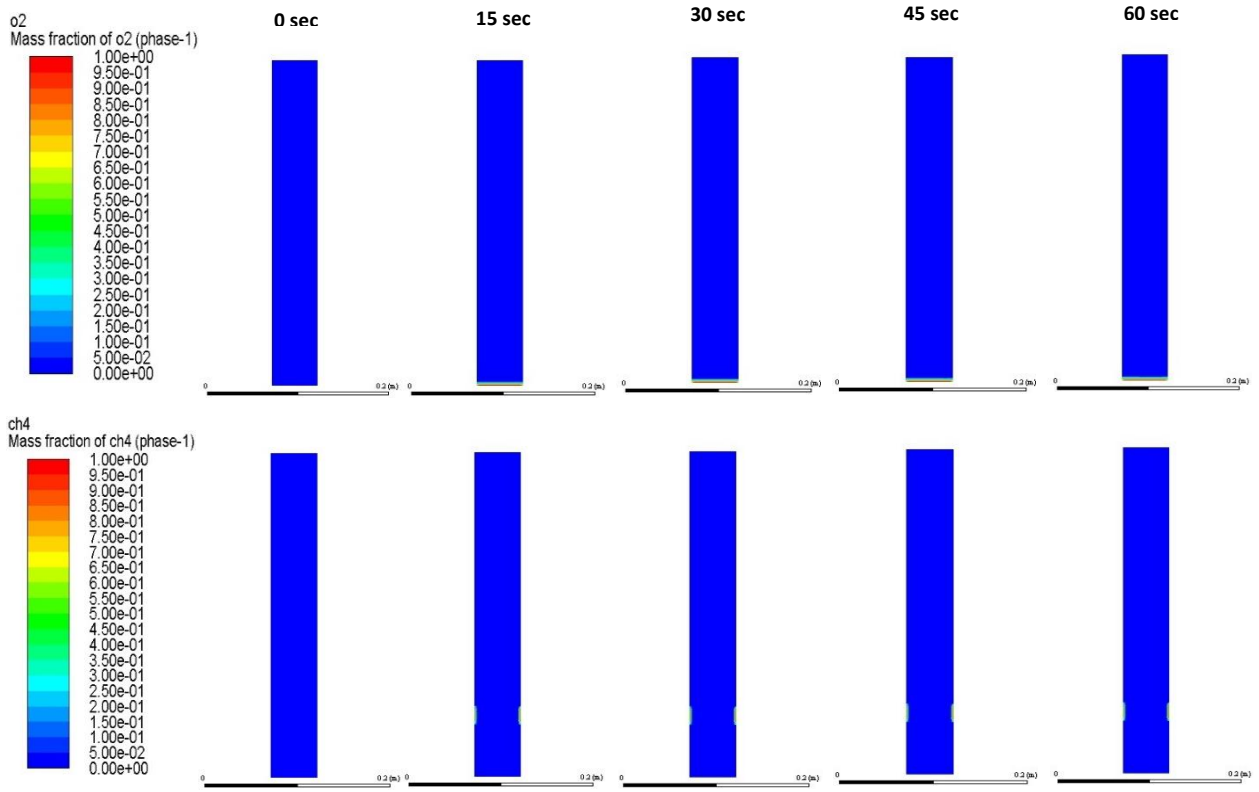


**Figure (4.10)** O<sub>2</sub> and CH<sub>4</sub> mass fraction distribution with respect to time

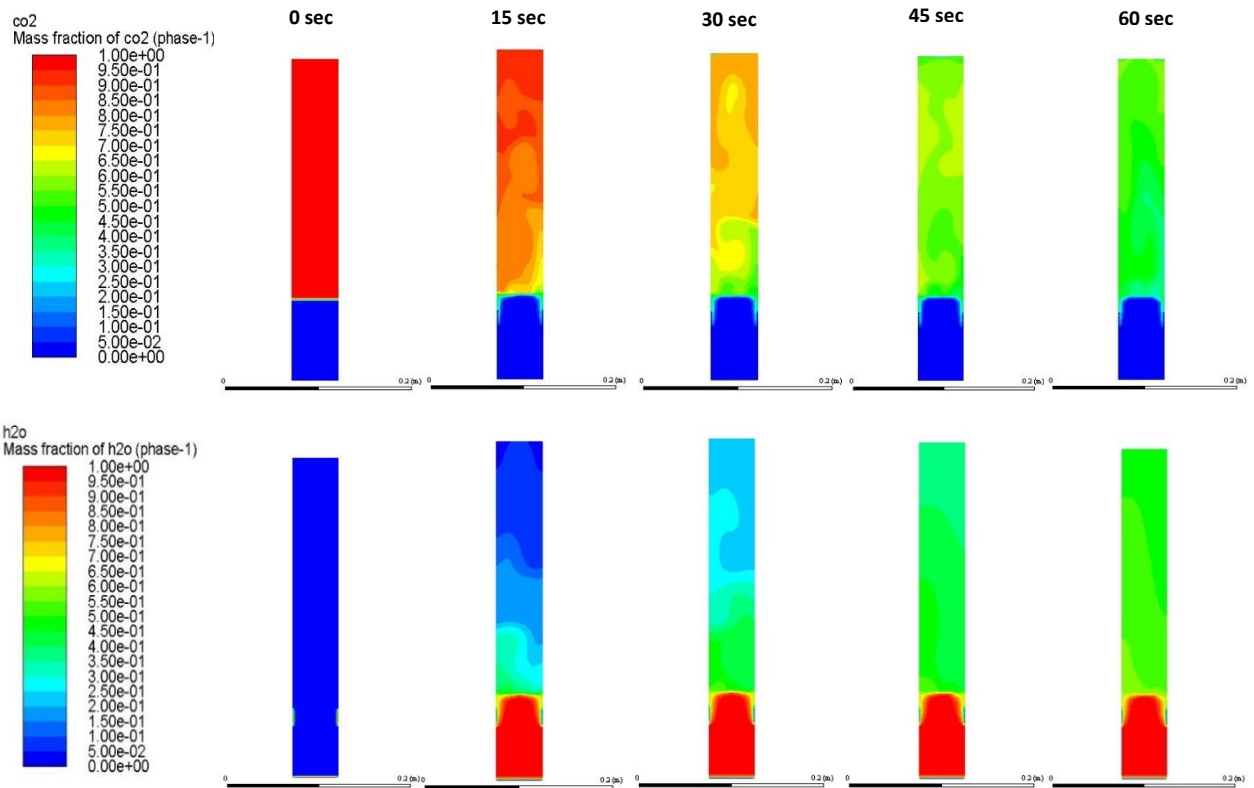


**Figure (4.11)** CO<sub>2</sub> and H<sub>2</sub>O mass fraction distribution with respect to time

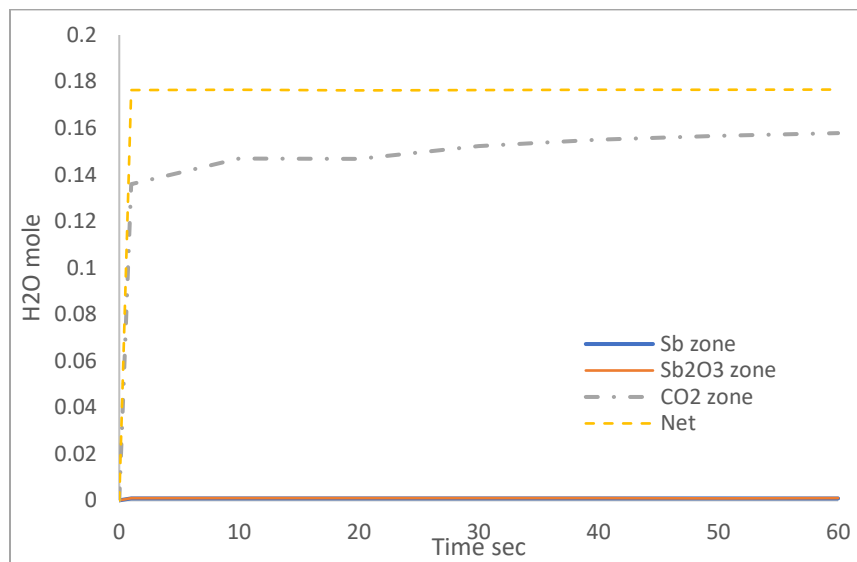


**Figure (4.12)** H<sub>2</sub>O mole value in each zone with respect to time

### **4.3 Oxidation and reduction ratio**

There were many technical limitations during the experiments conducted by Sims [11] that have a direct impact on the result obtained. The operating pressure on the membrane air side is limited to atmospheric, as well as the shape of the OTM was flat due to manufacturing limitations affected the oxygen fed to the reactor and the reaction rate for both oxidation and reduction. Using a different configuration, such as tubular or hollow fiber configuration will provide a much higher area per unit volume and allow for more contact between the air and oxygen carrier. In addition, it will reduce the membrane system size remarkably [41, 126]. Increasing the operating pressure and using different OTM configuration will dramatically increase the oxygen supply and will positively affect the redox rates for the integrated reactor. To overcome the limitation in the experimental results achieved by Sims [11] and to simulate such scenario, the oxidation rate was increased by 7.69 times in this study and reduction rate was increased by 20.69, 10.34 and 7.69 times that reported in the experimental work. Such an increase can be achieved by using higher operating pressure and different OTM configuration. In the current study, the temperature distributions in each zone for these cases are predicted. The total ratios of oxygen molar flow to methane molar flow calculated based on these increased rates as compared to the experimental conditions were calculated to be 7.81, 15.62 and 21.02 as shown in Table (4.4).

**Table (4.4)** Volumetric and ratio of gas flow

| Case   | Inlet                       | Volumetric flow (m <sup>3</sup> /m <sup>2</sup> .s) | Area (m <sup>2</sup> ) | Molar flow rate (kmol/s)  | Increase ratio of molar flow rate compare to Sims case | Ratio=O <sub>2</sub> molar flow rate/CH <sub>4</sub> molar flow rate |
|--------|-----------------------------|-----------------------------------------------------|------------------------|---------------------------|--------------------------------------------------------|----------------------------------------------------------------------|
| Case 1 | O <sub>2</sub> inlet        | 0.15                                                | 0.05                   | $9.019088 \times 10^{-5}$ | 7.69                                                   | 7.81                                                                 |
|        | CH <sub>4</sub> inlet 1     | 0.015                                               | 0.02                   | $5.7726 \times 10^{-6}$   | 20.69                                                  |                                                                      |
|        | CH <sub>4</sub> inlet 2     | 0.015                                               | 0.02                   | $5.7726 \times 10^{-6}$   | 20.69                                                  |                                                                      |
|        | Total CH <sub>4</sub> inlet | 0.015                                               | 0.04                   | $1.15452 \times 10^{-5}$  | 20.69                                                  |                                                                      |
| Case 2 | O <sub>2</sub> inlet        | 0.15                                                | 0.05                   | $9.019088 \times 10^{-5}$ | 7.69                                                   | 15.62                                                                |
|        | CH <sub>4</sub> inlet 1     | 0.0075                                              | 0.02                   | $2.8863 \times 10^{-6}$   | 10.34                                                  |                                                                      |
|        | CH <sub>4</sub> inlet 2     | 0.0075                                              | 0.02                   | $2.8863 \times 10^{-6}$   | 10.34                                                  |                                                                      |
|        | Total CH <sub>4</sub> inlet | 0.0075                                              | 0.04                   | $5.7726 \times 10^{-6}$   | 10.34                                                  |                                                                      |
| Case 3 | O <sub>2</sub> inlet        | 0.15                                                | 0.05                   | $9.019088 \times 10^{-5}$ | 7.69                                                   | 21.02                                                                |
|        | CH <sub>4</sub> inlet 1     | 0.00557455                                          | 0.02                   | $2.1453 \times 10^{-6}$   | 7.69                                                   |                                                                      |
|        | CH <sub>4</sub> inlet 2     | 0.00557455                                          | 0.02                   | $2.1453 \times 10^{-6}$   | 7.69                                                   |                                                                      |
|        | Total CH <sub>4</sub> inlet | 0.00557455                                          | 0.04                   | $4.2906 \times 10^{-6}$   | 7.69                                                   |                                                                      |

For Case1, Case2 and Case3 with the different molar flow rate ratio 7.81, 15.62 and 21.02 respectively at 950K operating temperature, the temperature distribution in each zone with time of reaction in both gas and liquid phase are predicted and the results are shown in figures (4.13a), (4.13b), (4.14a), (4.14b) and (4.15a), (4.15b). The net temperature and the temperature in each zone were observed to increase with time due to the exothermic reaction taking place inside the Sb zone where heat is generated and transfer to the other zone despite the endothermic reaction occurring in the Sb<sub>2</sub>O<sub>3</sub> zone. If we compare the Case1, Case2 and Case3 with the experimental case, we notice that the reactor reaches a steady state temperature in about 8 sec in all phases while in the experimental case the steady state condition is not achieved in 60 sec. This is due to the relatively higher reaction rates as a result of higher feed rates more products are generated and recirculated inside the reactor, therefore, temperature steady state is shortly achieved compared to Sims case.

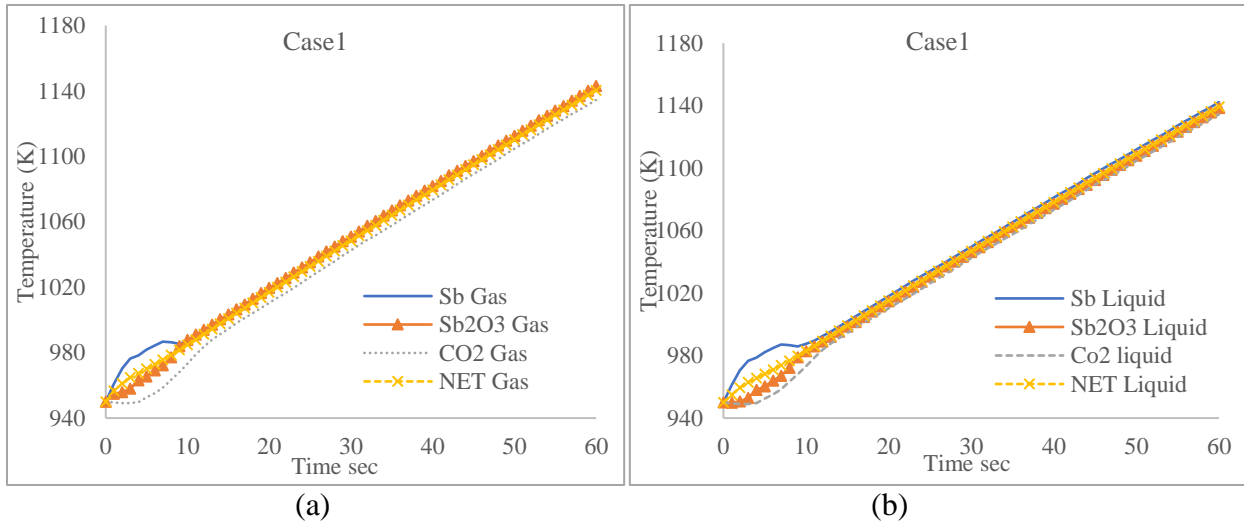


**Figure (4.13)** Temperature distribution of gas and liquid phases in each reactor zone Case1 at 950K temperature (a) gas phase (b) liquid phase

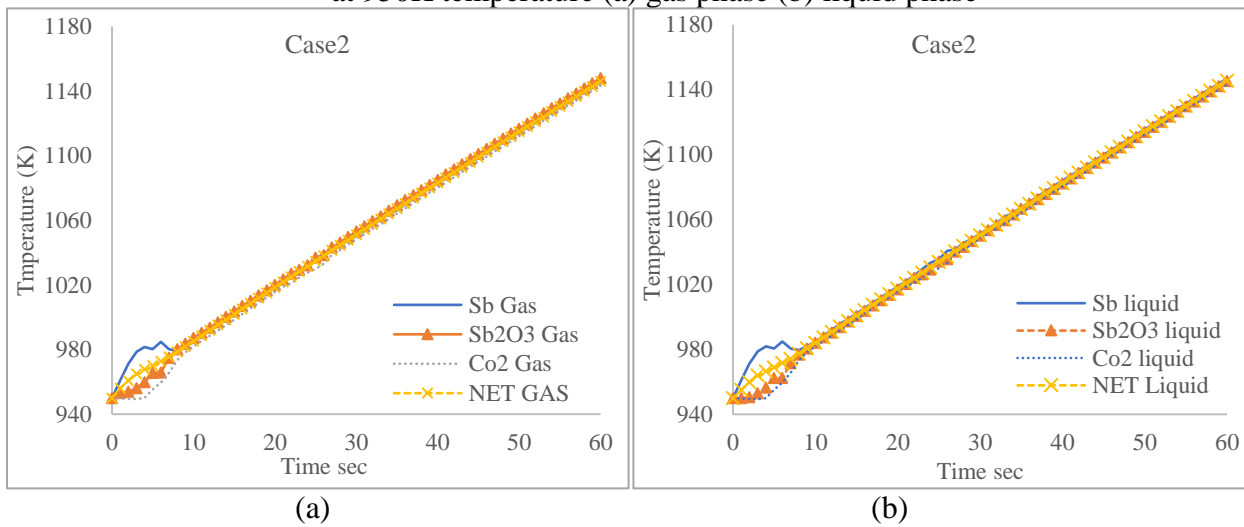


**Figure (4.14)** Temperature distribution of gas and liquid phases in each reactor zone Case2 at 950K temperature (a) gas phase (b) liquid phase

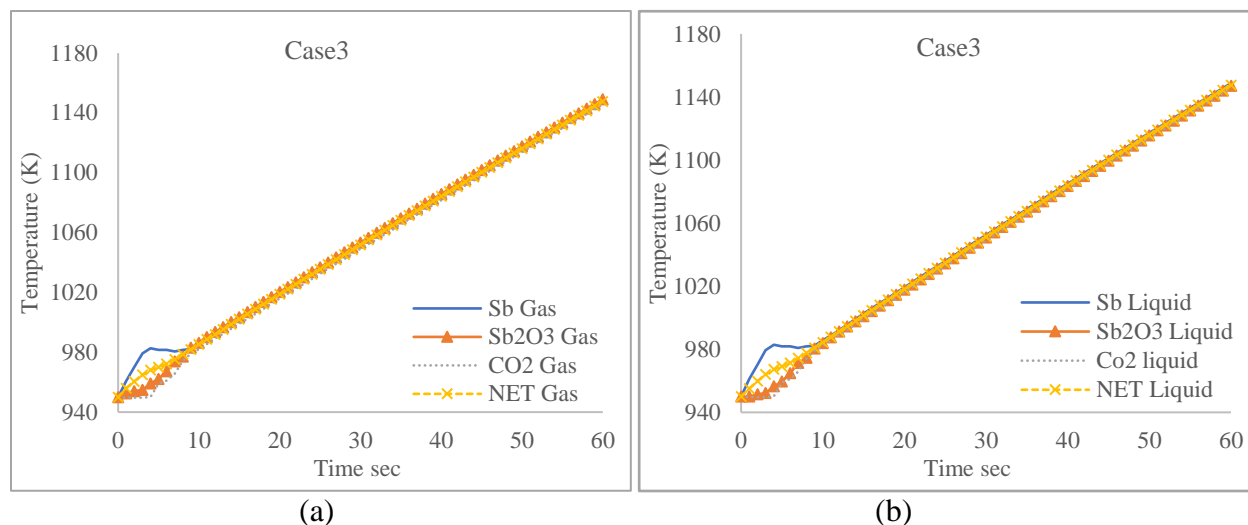


**Figure (4.15)** Temperature distribution of gas and liquid phases in each reactor zone Case 3 at 950K temperature (a) gas phase (b) liquid phase

The figures (4.16), (4.17) and (4.18) show the predicted gas and liquid phase temperature profiles contours for each case with respect to reaction time. The net temperature for both gas and liquid are higher for the Case3 as compared to other cases (Case1, Case2 and Sims case) from more oxidation and less reduction reaction take place inside the reactor as shown in figure (4.19) and (4.20).

The heat released during the exothermic oxidation process drives the temperature difference. It is significantly larger than the convective heat transfer. As a result, the Sb zone liquid phase has a higher temperature compared to other areas inside the reactor as shown in figure (4.21a). If the intensity of heat exchange and the volumetric heat transfer coefficient between the two phases are equal, then the temperature profiles predicted are almost the same. Only the temperature of the gas phase in  $Sb_2O_3$  zone has a higher temperature than the Sb zone in all simulated cases, despite the endothermic reaction nature taking place in this area as shown in figure (4.21b). Thus, due to higher convection rate inside  $Sb_2O_3$  zone due to the higher Nusselt - product form reduction reaction.

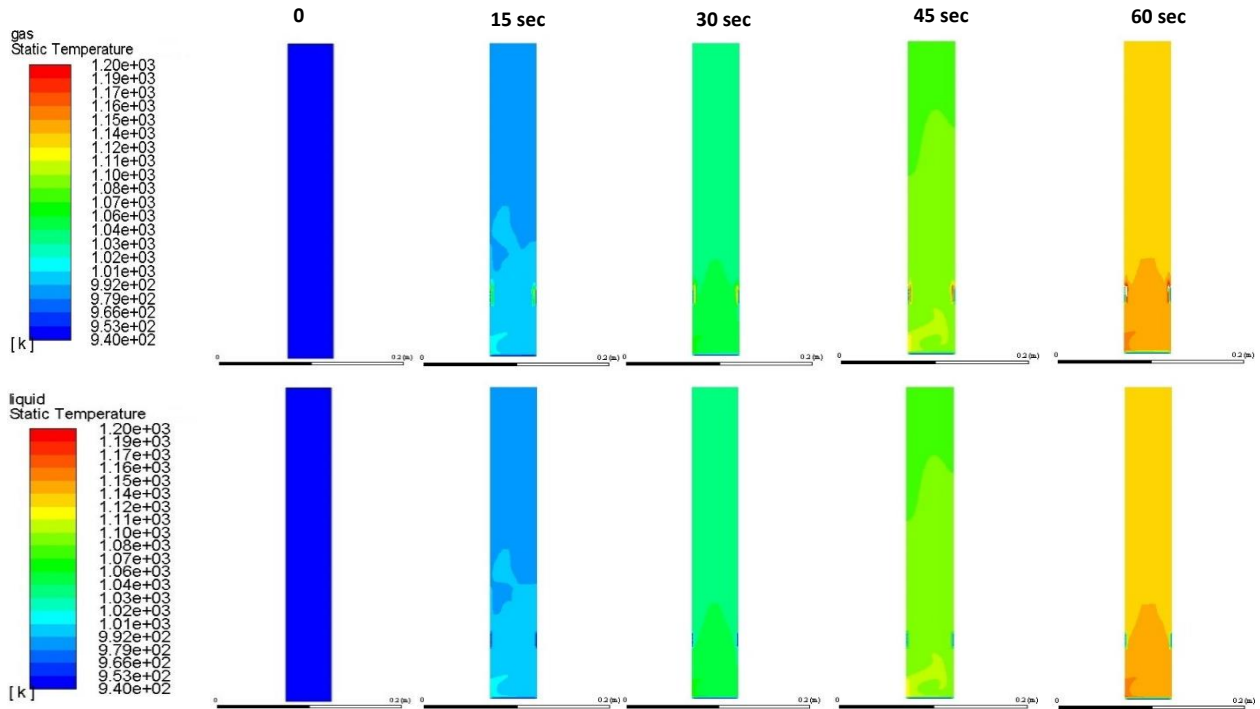


Figure (4.16) Temperature contour of gas and liquid of reactor zones Case1 at 950K

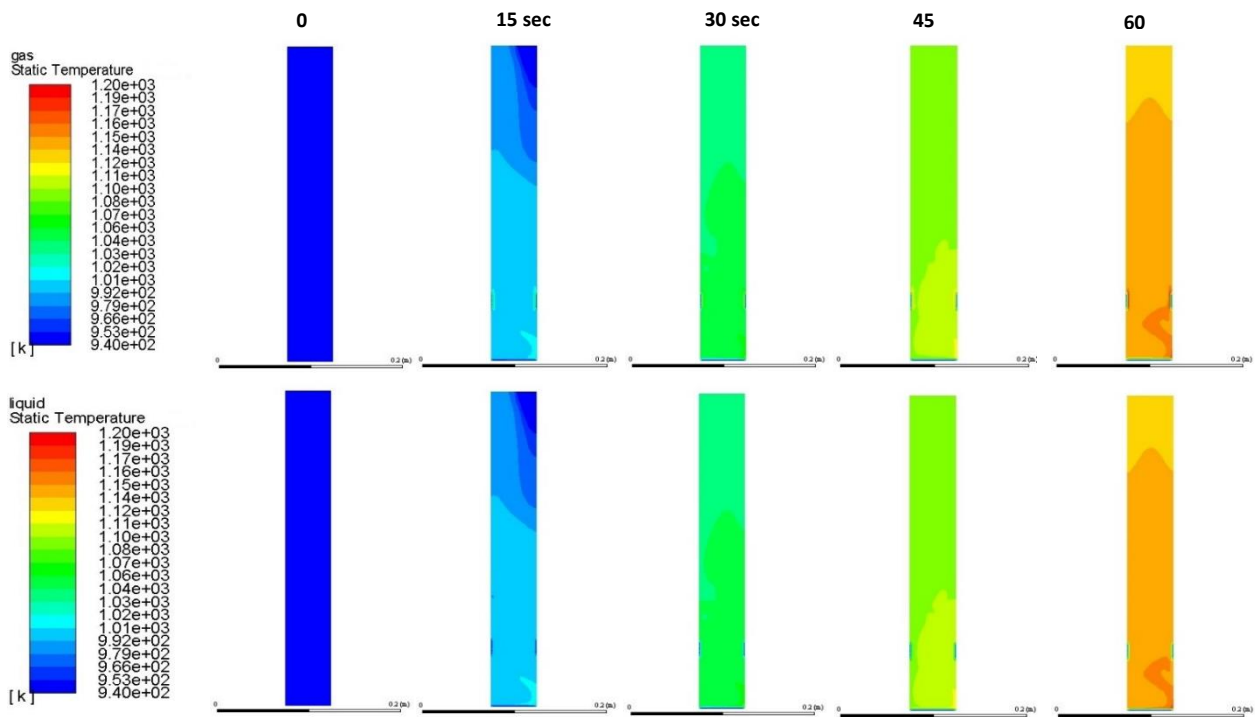
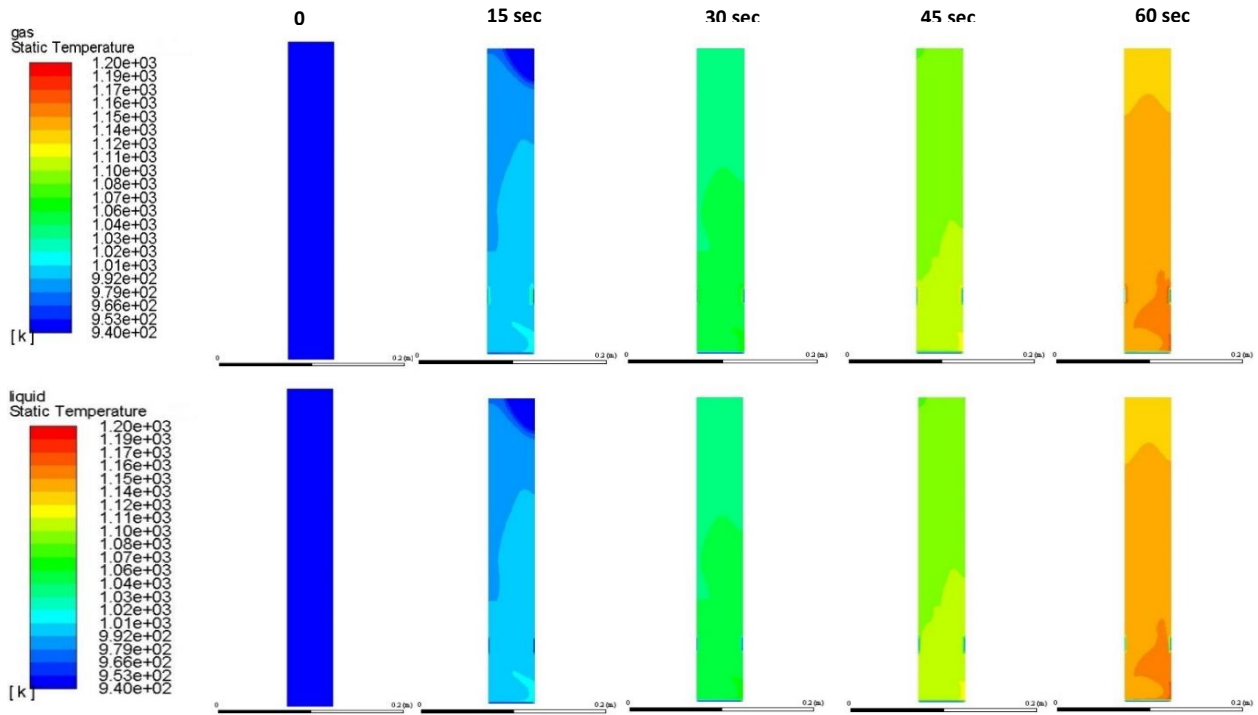
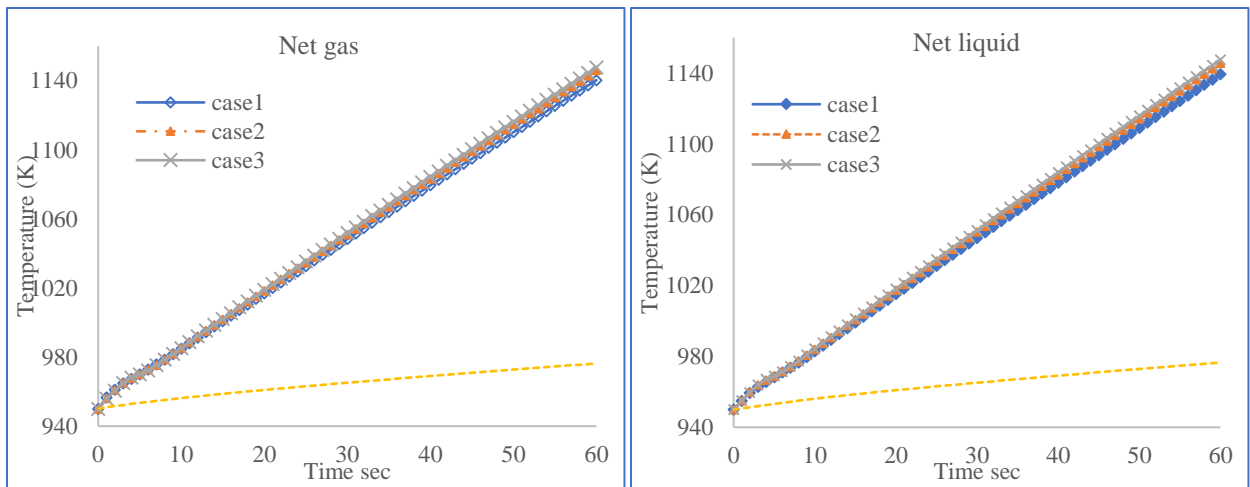


Figure (4.17) Temperature contour of gas and liquid of reactor zones Case2 at 950K



**Figure (4.18)** Temperature contour of gas and liquid of reactor zones Case3 at 950K



**Figure (4.19)** The net gas and liquid temperature comparison for all simulated cases at 950K

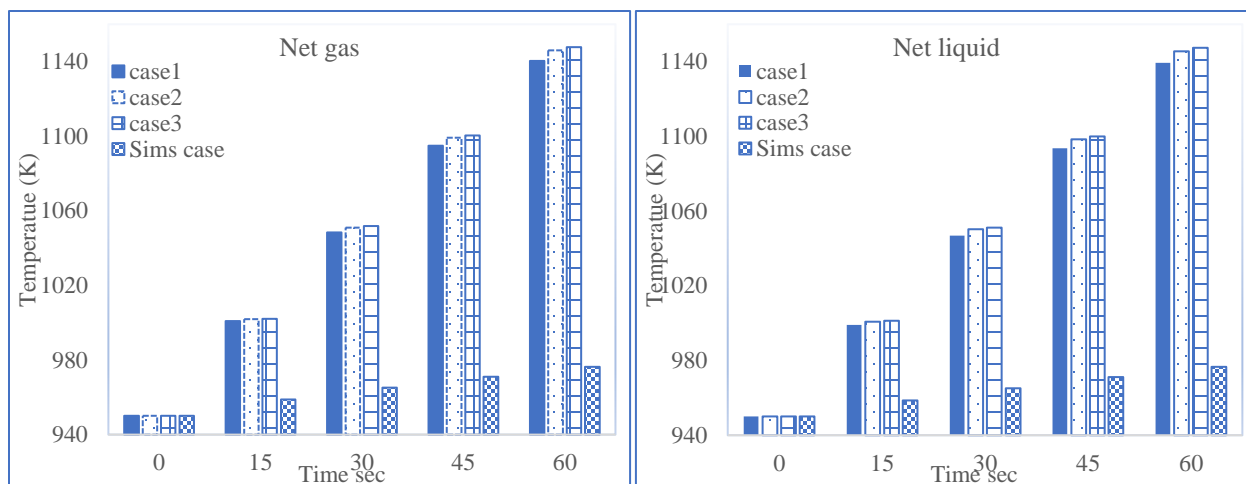


**Figure (4.20)** The net gas and liquid temperature comparison for all simulated cases at 950K

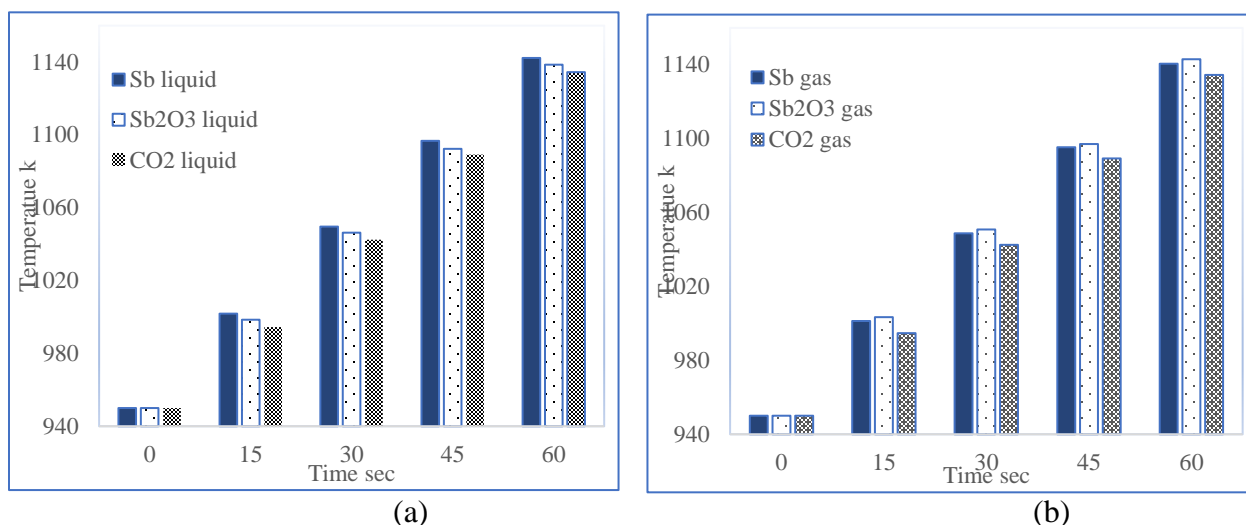


**Figure (4.21)** Temperature distribution for each reactor zone Case1 (a) liquid phase (b) gas phase

The concentration of Sb and Sb<sub>2</sub>O<sub>3</sub> inside the reactor are affected by the volumetric oxygen and methane rate entering the system. Here more Sb<sub>2</sub>O<sub>3</sub> is produced during the oxidation reactions and lower Sb is produced during the reduction when methane volumetric values are varied from Case1, Case2, Case3, and Sims case. Figure (4.22) shows the ration of Sb over Sb<sub>2</sub>O<sub>3</sub> inside the reactor respect to time of reaction where less Sb is produced in Case3 compared to Case1 with the higher volumetric flow of methane. Similar trends are observed in the Sims case where the Sb production is lower than Sb<sub>2</sub>O<sub>3</sub>.

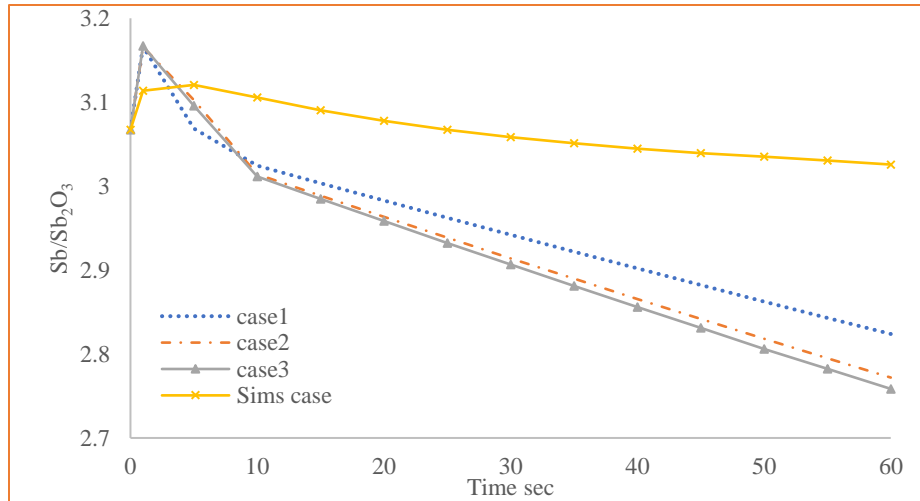
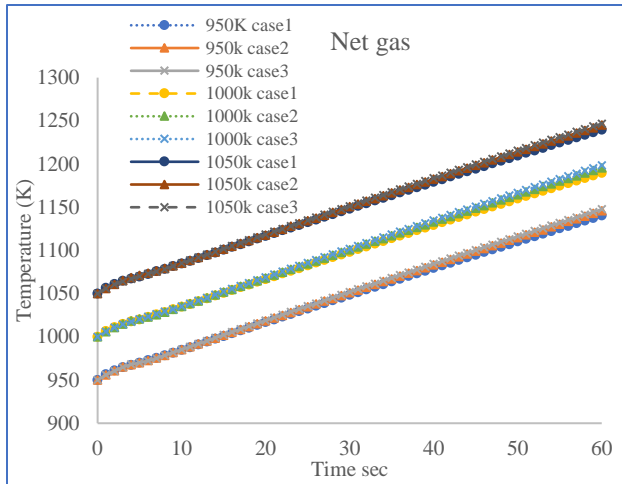


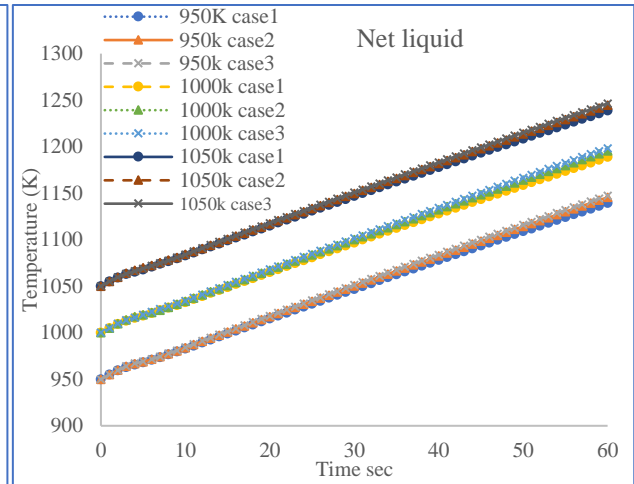
**Figure (4.22)** The concentration ratio of Sb and Sb<sub>2</sub>O<sub>3</sub> inside the reactor during reaction time

#### **4.4 The effect of operating temperature**

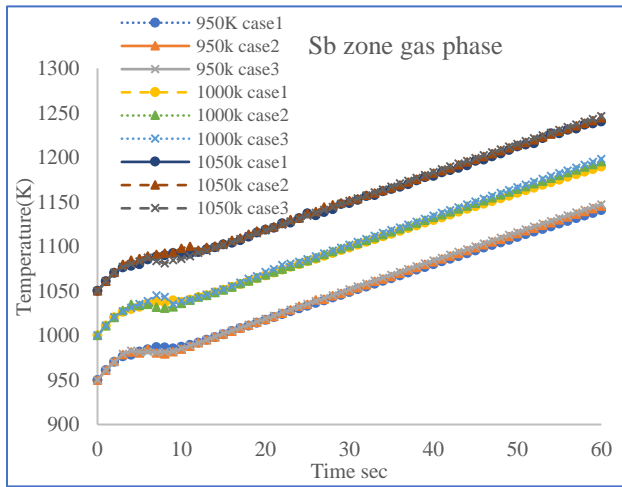
Increasing the operating temperature in real life will help to increase the efficiency of OTM, which mean more oxygen flux will be achieved. On the other hands higher operation temperature reactor will be useful to utilize the heat and generate steam with higher quality. The same molar flow rate of oxygen and methane (Case1, Cse2, Case3 and Sims case) are being used but with higher operating temperature 1000K and 1050K. These cases are selected in addition to the first simulation at 950K, to predict and compare the temperature profile inside reactor zones. During the 60 second reactor simulation the temperature of each zone and for both phases in Case1, Case2 and Case3 are found to increase about 200K regardless of the operating temperature as shown in figure (4.23). Increasing the oxidation rate by 7.69 with respect to the Sims case has a huge impact on the temperature profile in each case irrespective of the reduction rate, while the simulation using the experimental values showed a temperature increase of about 26K only as shown in figure (4.24).



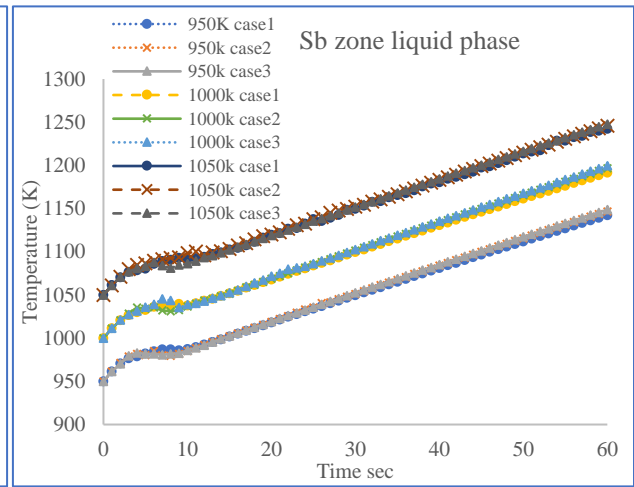
(a)



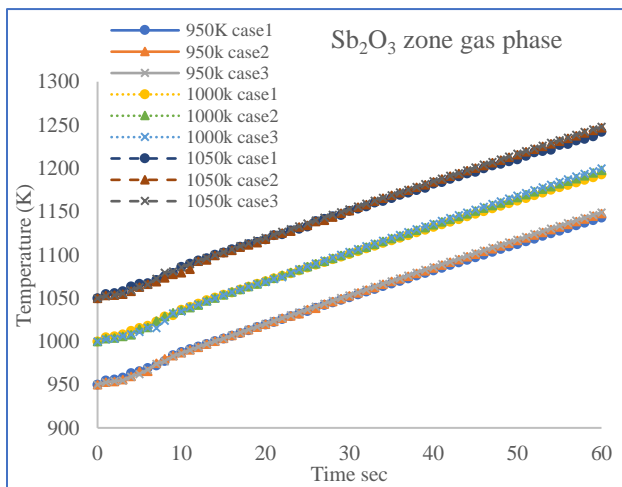
(b)



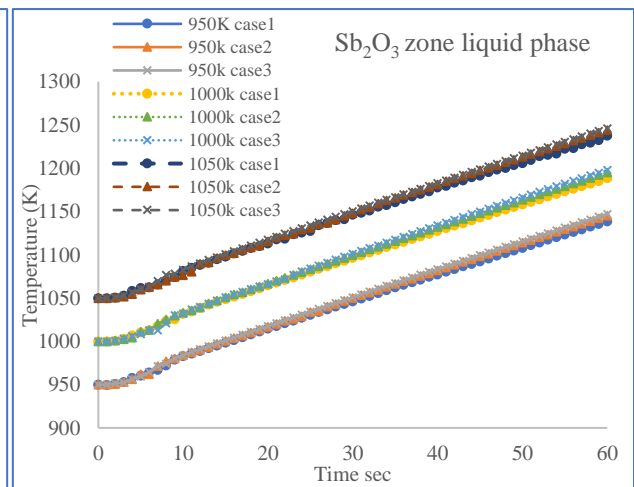
(c)



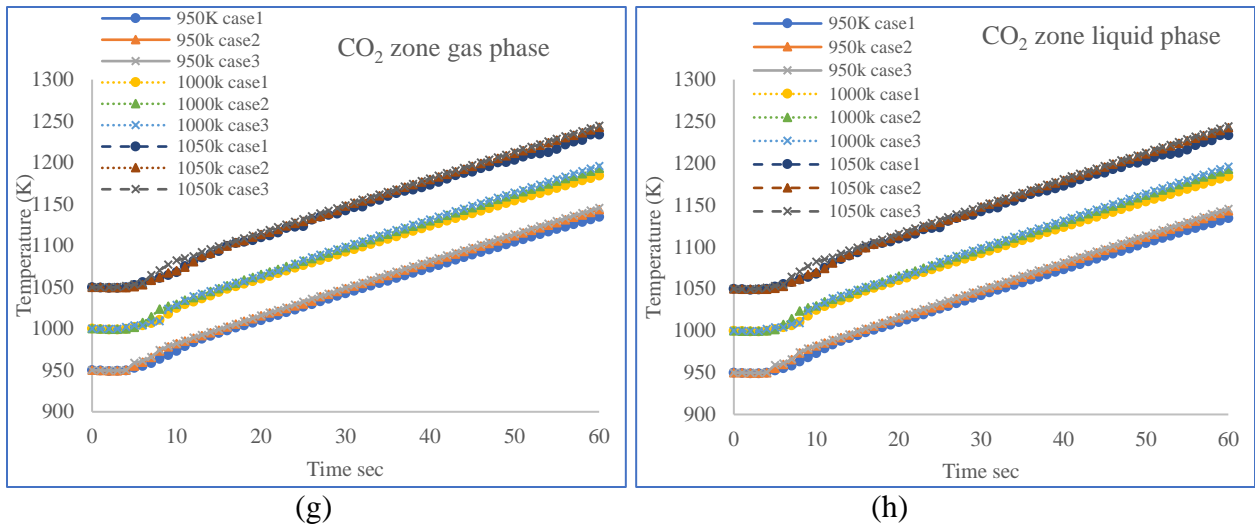
(d)



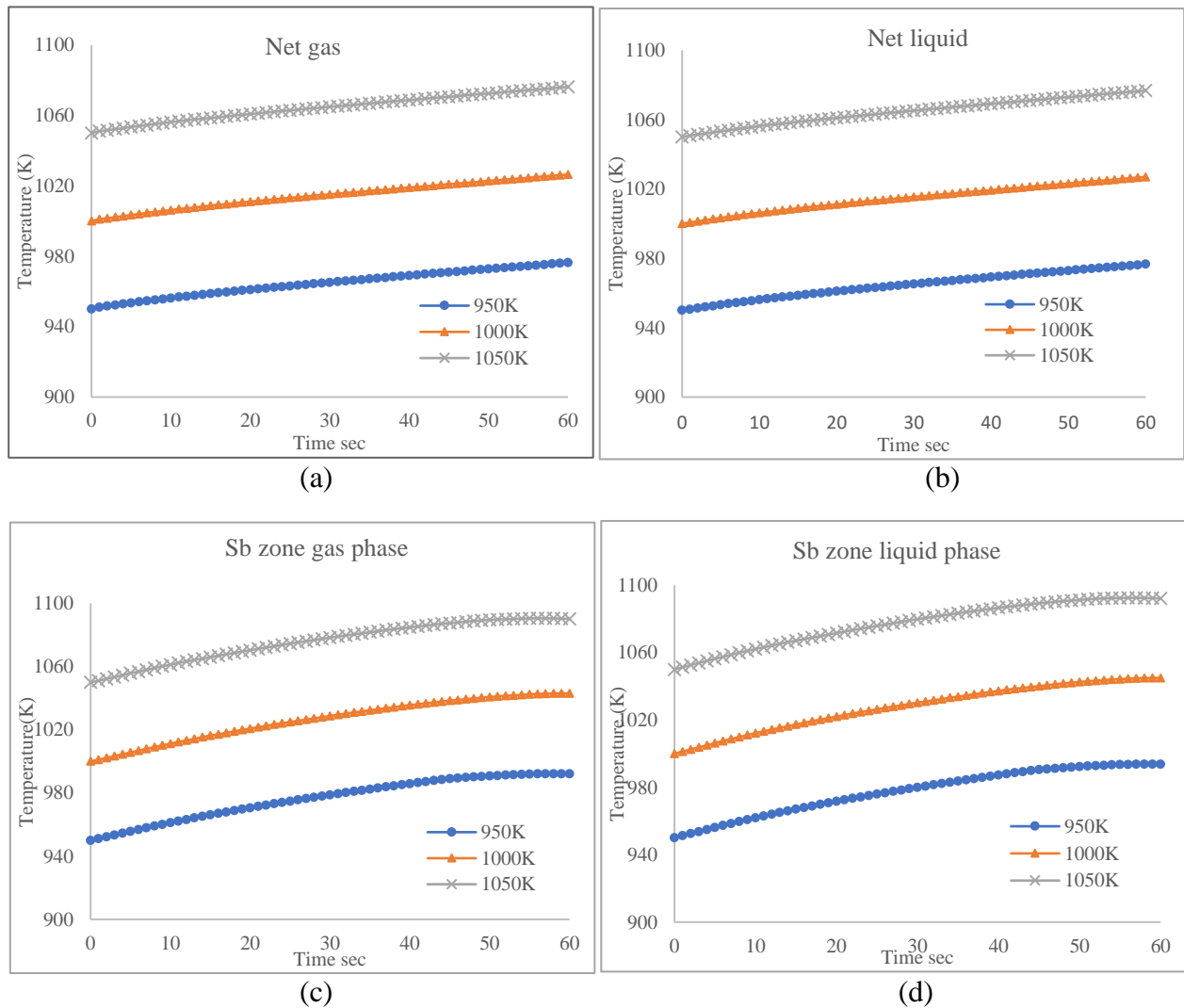
(e)



(f)



**Figure (4.23)** The temperature distribution prediction in each zone inside the reactor for different operation temperature.



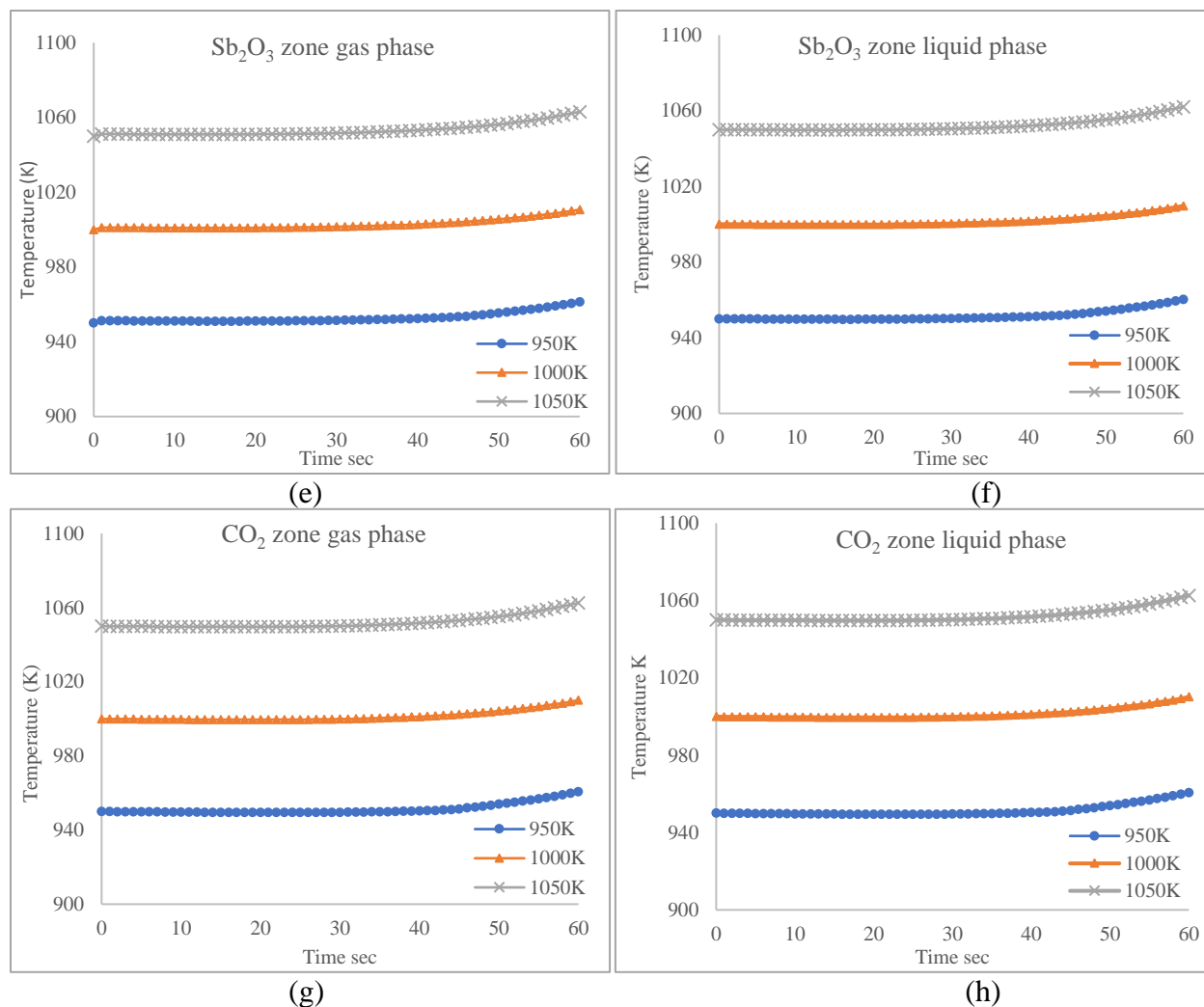


**Figure (4.24)** The temperature distribution prediction in each zone inside the reactor for different operation temperature Sims case.

#### 4.5 The effect of viscosity of liquid metals

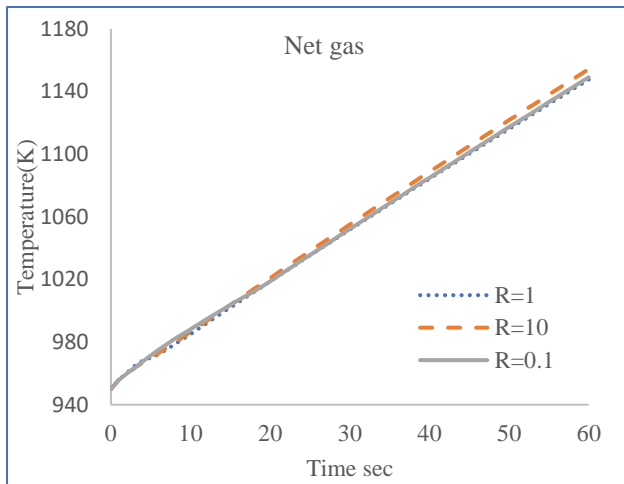
The concept of a single reactor system under investigation is dependent on the natural circulation of antimony and antimony trioxide due to the density difference, therefore metal viscosity plays a major role during the metal circulation. The lack of some physical properties, such as viscosity and thermal conductivity, of liquid antimony and antimony trioxide was challenging during this study. Therefore, the thermal conductivity used during this study is based on information available on the solid phase as discussed in the previous chapter. The value of

liquid antimony viscosity is used based on [127] where viscosity is a function of temperature, while the value of liquid antimony trioxide is not available in the literature. To circumvent this lack of data and to study the effect of the viscosity on the temperature profiles in each reactor zone a ratio (R) is defined as the viscosity of liquid antimony over viscosity of liquid antimony trioxide. The temperature profile predicted in reactor zones operated at 950K with three different ratios R=1, R=10 and R=0.1 as shown in the table (4.5).

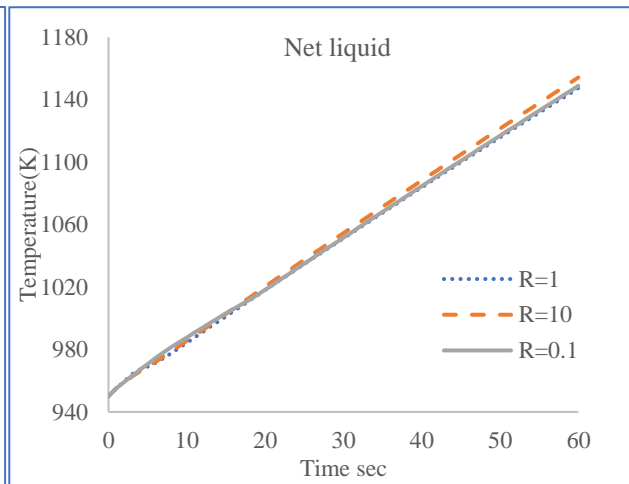
**Table (4.5)** The viscosity values for antimony and antimony trioxide used in the simulations

| ratio (R) | Sb viscosity (kg/m-s) | Sb <sub>2</sub> O <sub>3</sub> viscosity (kg/m-s) |
|-----------|-----------------------|---------------------------------------------------|
| 1         | 0.00118971            | 0.00118971                                        |
| 10        | 0.0118971             | 0.00118971                                        |
| 0.1       | 0.00118971            | 0.0118971                                         |

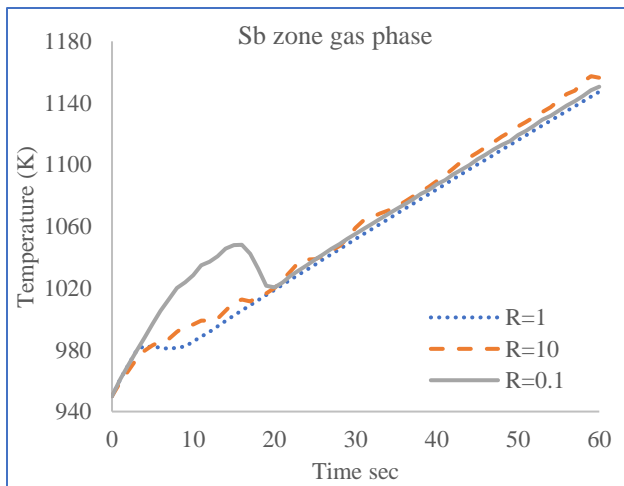
The result shows no changes in the net gas and net liquid temperature for all ratios under investigation. The only changes in temperature profiles have happened before reaching the steady state temperature in all zones. Viscosity is defined as fluid resistance to flow and because our reactor used liquid metal circulation to transfer heat among its zones, an increase in fluid flow resistance will lead to resistance to convective heat transfer. For R=0.1, which means the Sb<sub>2</sub>O<sub>3</sub> has a higher viscosity, the Sb<sub>2</sub>O<sub>3</sub> generated inside the Sb zone during the oxidation process will have more resistance to the flow and will need more time to rise to the next zone. This will affect the temperature profile inside all reactor zones with both gas and liquid by increasing the temperature in the Sb zone because the Sb<sub>2</sub>O<sub>3</sub> liquid metal needs more time to move to the next zone and decrease the temperature in both Sb<sub>2</sub>O<sub>3</sub> and CO<sub>2</sub>. The main viscosity effect is changing the time to reach steady state temperature, which in this case is about 20 sec compared to 8 sec for R=1. Similarly, for R=10, means Sb<sub>2</sub>O<sub>3</sub> have lower viscosity and therefore required less time to move to the next zone. In this case, steady state temperature can be achieved with about 4 sec as shown in figure (4.25)



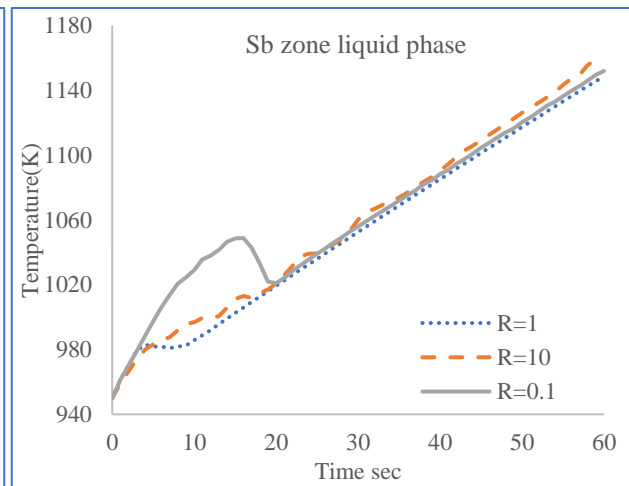
(a)



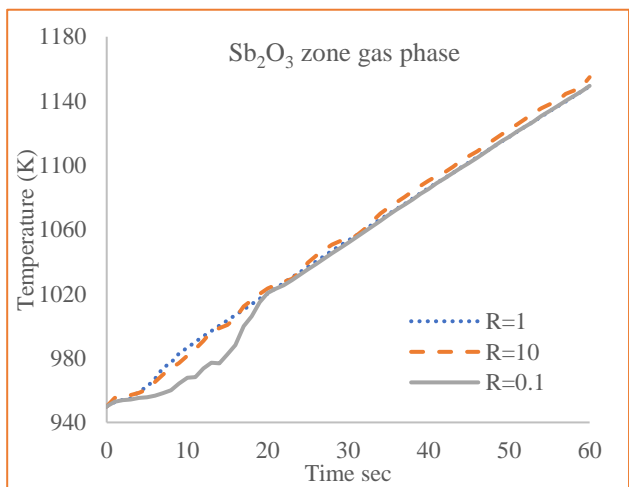
(b)



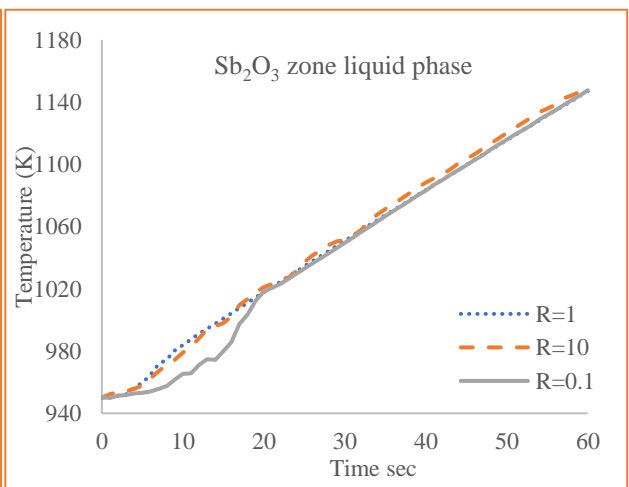
(c)



(d)



(e)



(f)

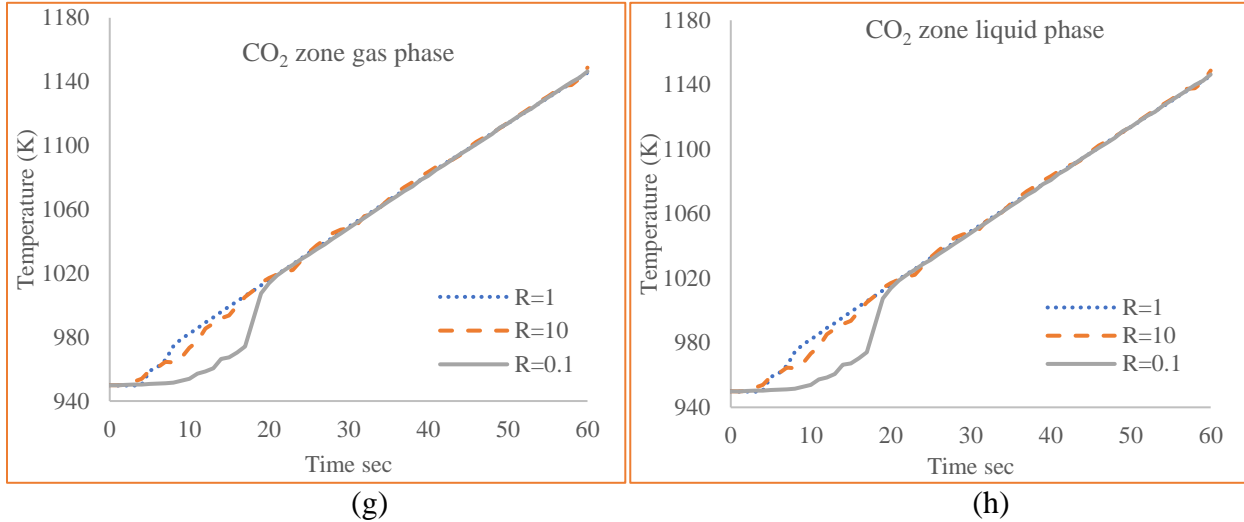
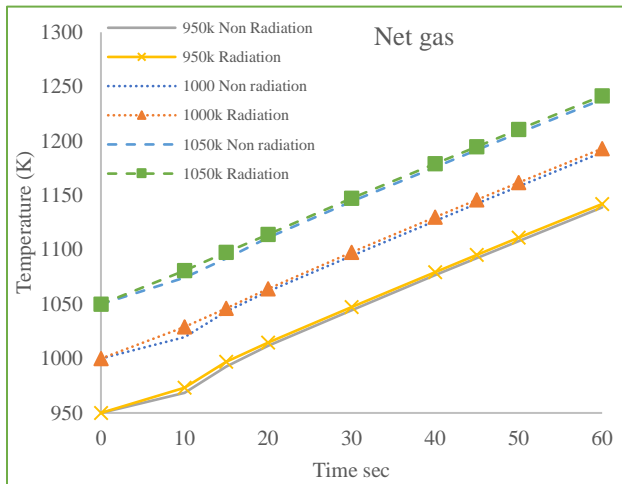


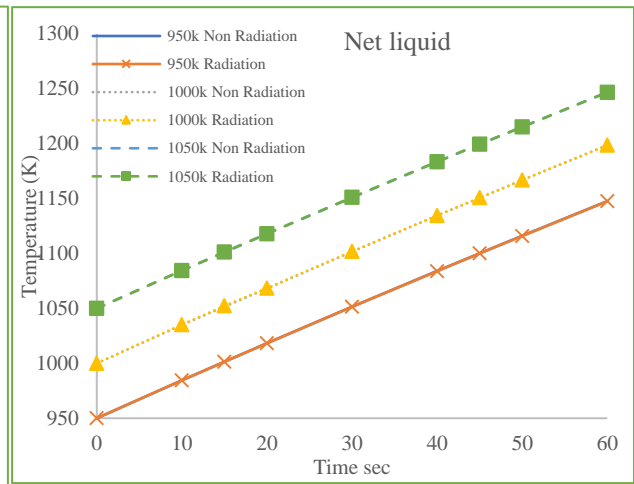
**Figure (4.25)** The effect of viscosity on temperature profile of reactor

#### **4.6 The effect of radiation**

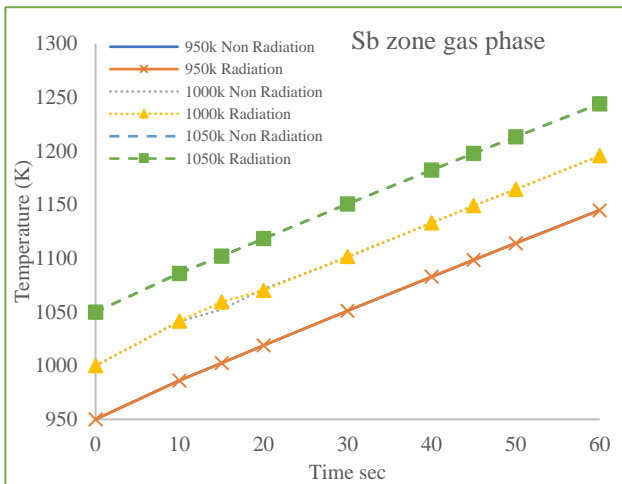
The radiation plays an important role inside the reactor by keeping the temperature constant and reduce the heat loss to the surroundings. In the case under investigation the wall is adiabatic but to show the effect of the radiation inside the reactor, radiation effect on temperature profiles are studied and compared with the non-radiation effects. Case3 are simulated with radiation and with three different operation temperature 950K, 1000K and 1050K. The results are shown in figure (4.26), where the net gas temperature increased slightly due to the radiation effect and because the gas mixture mainly CO<sub>2</sub> and H<sub>2</sub>O are absorbing more heat and thus increase the temperature of the zone. The CO<sub>2</sub> zone with gas phase have a higher temperature compared to the non-radiation case, we can see a slight change in the total temperature. The liquid phase inside the reactor has no change due to zero absorption condition assumption.



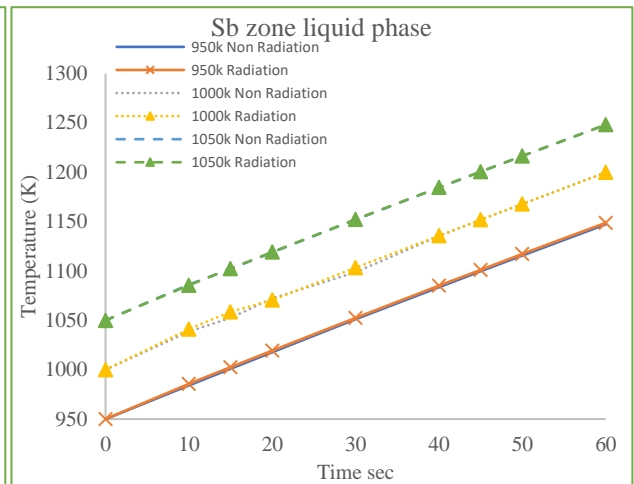
(a)



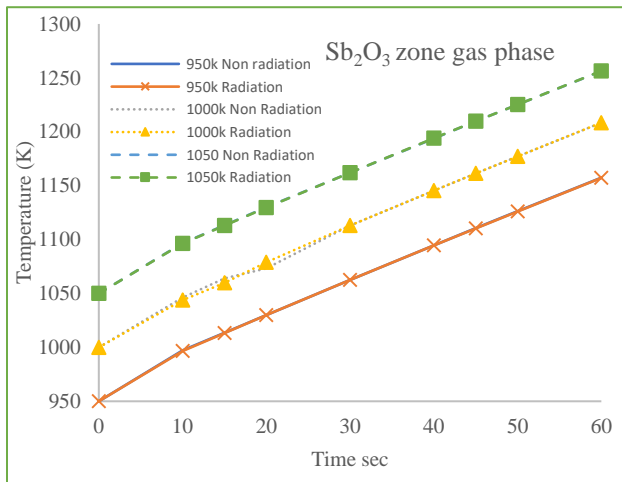
(b)



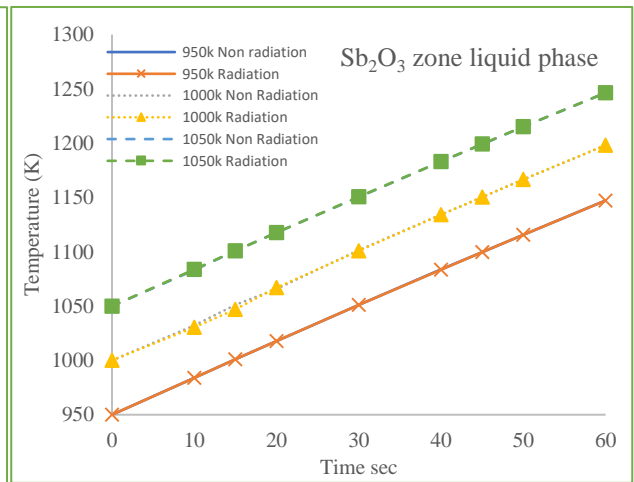
(c)



(d)



(e)



(f)

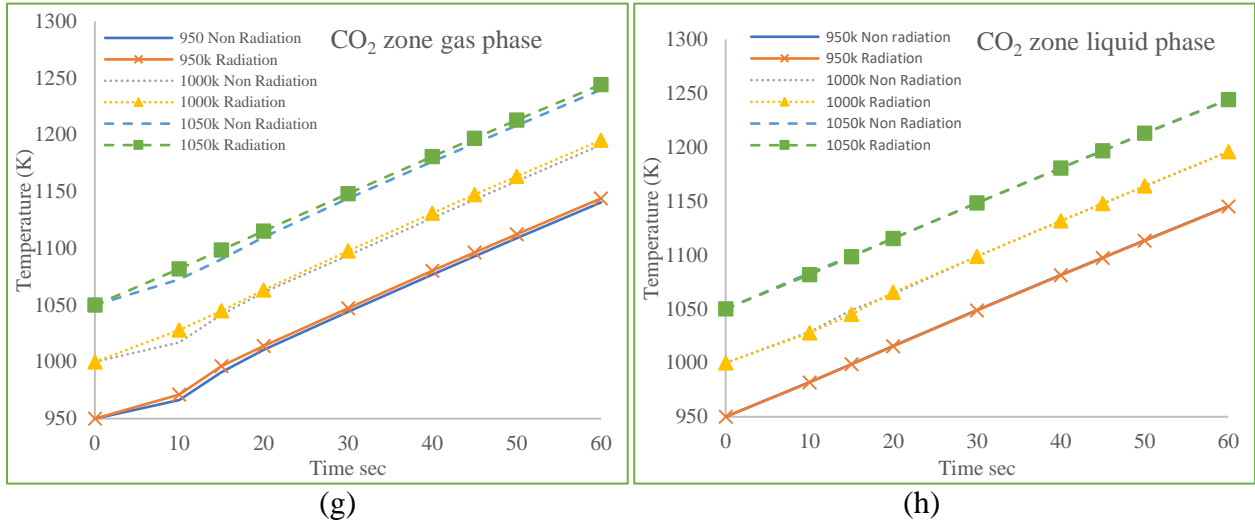


**Figure (4.26)** Radiation effect in each reactor zone with different operation temperature Case3

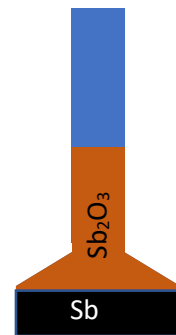
## CHAPTER 5

### CONCLUSION

In this work simulation for the integrated oxycombustion system is investigated to predict and understand the temperature profiles inside the reactor zones using different oxidation and reduction rates, the viscosity of liquid metal and radiation. The graphical curves and the contours show the predicted temperature profiles and the species concentration with respect to reaction time. The result of this work has led to the following conclusions.

1. Increasing the volumetric oxygen flow rate by 7.69 times the experimental conditions increased the total energy released from  $100 \text{ kWm}^{-2}$  to  $760 \text{ kWm}^{-2}$ .
2. Increasing the volumetric methane flow rate will reduce the reactor overall temperature and the temperature in each zone for both phases.
3. Increasing the operating temperature does not affect the rate of temperature increase in each zone, but the higher operation temperature is preferred to increase the OTM efficiency, ie the oxygen transport rate through the membrane.
4. The liquids' viscosity effects are recognized only before the reactor reaches steady state temperature because no enough amount of Sb and  $\text{Sb}_2\text{O}_3$  is forming. Increasing liquid metal concentration in each zone will inhibit the viscosity effect.
5. Operating temperature has no effect on the rate of temperature increase in each zone. Higher operation temperature in real life will increase the OTM efficiency, means more oxygen flux. Higher operating temperature will be useful to utilize the heat and generate steam with higher quality.

6. As expected, the radiation effect is only recognized for gas in the CO<sub>2</sub> zone because gas absorbed more heat and radiation effect of liquid is not noticeable due to zero absorption condition.
7. Increasing the contact area between the oxygen and medium by changing the OTM configuration will increase the oxygen reaction rate and, thus increase the heat released.
8. The best place to mount a boiler tubes is the CO<sub>2</sub> zone to utilize the heat and produce steam with good quality.
9. Using an inverted funnel shape reactor will increase the effective contact area of a membrane per unit reactor volume and provide longer residence time for uncombusted components. The tube diameter ratios can be designed based on the oxidation/ reduction rates to ensure required Sb and Sb<sub>2</sub>O<sub>3</sub> content is obtained as required for steady state condition. Finally, static nozzles may be used for the delivery of methane to create swirls inside Sb<sub>2</sub>O<sub>3</sub> in order to increase the heat transfer rate.



### **Recommendation for future work**

The integrated system under investigation are contained three sub system oxycombustion, LCLC, and OTM, therefore enhancement in one of these subsystems will improve the overall efficiency of the integrated. The following suggestion for future works:

1. Develop a 3D model to simulate the reactor with boiler tubes placed inside it to predict the overall temperature profiles in the reactor and inside the heat exchanger.
2. Antimony and antimony trioxide have great potential to serve as a medium in LCLC, but other metals have the same potential. One such element is bismuth. The different liquid

metal and metal oxides redox couples that exist as liquids at reasonable temperatures need to be investigated.

3. The reduction process for the system under study simulates methane as fuel. Using other fuel types such as coal and biomass to predict the temperature profile inside the reactor and compare the result of using different fuel types. Experimental studies will provide the required kinetic parameters.
4. The reduction process is assumed to be complete with using methane. This is achievable by controlling the methane feed rate. It is recommended to simulate the incomplete combustion by using higher methane flow rates and compare the two data.

## REFERENCES

- [1] NASA, "Graphic: The relentless rise of carbon dioxide,"  
[https://climate.nasa.gov/climate\\_resources/24/graphic-the-relentless-rise-of-carbon-dioxide/](https://climate.nasa.gov/climate_resources/24/graphic-the-relentless-rise-of-carbon-dioxide/).
- [2] 2017, "Carbon Dioxide Emissions From Power Plants Rated Worldwide,"  
<https://www.sciencedaily.com/releases/2007/11/071114163448.htm>.
- [3] Châtel-Pélage, F., Varagani, R., Pranda, P., Perrin, N., Farzan, H., U. Yongqi, L., Chen, S., Rostam-Abadi, M., and Bose, A., 2006, Applications of Oxygen for NO<sub>x</sub> Control and CO<sub>2</sub> Capture in Coal-Fired Power Plants.
- [4] Abu-Zahra, M. R. M., Niederer, J. P. M., Feron, P. H. M., and Versteeg, G. F., 2007, "CO<sub>2</sub> capture from power plants: Part II. A parametric study of the economical performance based on mono-ethanolamine," *International Journal of Greenhouse Gas Control*, 1(2), pp. 135-142.
- [5] Gibbins, J., and Chalmers, H., 2008, "Carbon capture and storage," *Energy Policy*, 36(12), pp. 4317-4322.
- [6] Bhowan, A. S., and Freeman, B. C., 2011, "Analysis and Status of Post-Combustion Carbon Dioxide Capture Technologies," *Environmental Science & Technology*, 45(20), pp. 8624-8632.
- [7] Sunarso, J., Hashim, S. S., Zhu, N., and Zhou, W., 2017, "Perovskite oxides applications in high temperature oxygen separation, solid oxide fuel cell and membrane reactor: A review," *Progress in Energy and Combustion Science*, 61, pp. 57-77.
- [8] Jafarian, M., Arjomandi, M., and Nathan, G. J., 2017, "Thermodynamic potential of high temperature chemical looping combustion with molten iron oxide as the oxygen carrier," *Chemical Engineering Research and Design*, 120, pp. 69-81.

- [9] Chen, Y., Qian, B., Hao, Y., Liu, S., Tade, M. O., and Shao, Z., 2014, "Influence of sealing materials on the oxygen permeation fluxes of some typical oxygen ion conducting ceramic membranes," *Journal of Membrane Science*, 470, pp. 102-111.
- [10] Mondal, K., 2016, "Mediated Oxycombustion Of Coal (MOC) With Integrated Advanced Oxygen Supply."
- [11] Sims, A. W., 2017, *A Novel Mediated Oxycombustion System: Subsystem Evaluation and Integration*, Southern Illinois University at Carbondale.
- [12] Aslanidis, N., and Iranzo, S., 2009, "Environment and development: is there a Kuznets curve for CO<sub>2</sub> emissions?," *Applied Economics*, 41(6), pp. 803-810.
- [13] Fan, L.-S., 2010, *Chemical looping systems for fossil energy conversions*, Wiley-AIChE, Hoboken, NJ.
- [14] Mattisson, T., Lyngfelt, A., and Cho, P., 2001, "The use of iron oxide as an oxygen carrier in chemical-looping combustion of methane with inherent separation of CO<sub>2</sub>," *Fuel*, 80(13), pp. 1953-1962.
- [15] Matson, S. L., Ward, W. J., Kimura, S. G., and Browall, W. R., 1986, "Membrane oxygen enrichment: II. Economic assessment," *Journal of Membrane Science*, 29(1), pp. 79-96.
- [16] Murali, R. S., Sankarshana, T., and Sridhar, S., 2013, "Air Separation by Polymer-based Membrane Technology," *Separation & Purification Reviews*, 42(2), pp. 130-186.
- [17] Fernández-Barquín, A., Casado-Coterillo, C., Valencia, S., and Irabien, A., 2016, "Mixed Matrix Membranes for O<sub>2</sub>/N<sub>2</sub> Separation: The Influence of Temperature," *Membranes*, 6(2).
- [18] Sunarso, J., Baumann, S., Serra, J. M., Meulenber, W. A., Liu, S., Lin, Y. S., and Diniz da Costa, J. C., 2008, "Mixed ionic–electronic conducting (MIEC) ceramic-based membranes for oxygen separation," *Journal of Membrane Science*, 320(1-2), pp. 13-41.

- [19] Zhang, Z., Verykios, X. E., and Baerns, M., 1994, "Effect of Electronic Properties of Catalysts for the Oxidative Coupling of Methane on Their Selectivity and Activity," *Catalysis Reviews*, 36(3), pp. 507-556.
- [20] Cousin, P., and Ross, R. A., 1990, "Preparation of mixed oxides: a review," *Materials Science and Engineering: A*, 130(1), pp. 119-125.
- [21] Cushing, B. L., Kolesnichenko, V. L., and O'Connor, C. J., 2004, "Recent Advances in the Liquid-Phase Syntheses of Inorganic Nanoparticles," *Chemical Reviews*, 104(9), pp. 3893-3946.
- [22] A. Haas, P., 1989, Gel processes for preparing ceramics and glasses, *Chemical Engineering Progress*
- [23] Sōmiya, S., and Roy, R., 2000, "Hydrothermal synthesis of fine oxide powders," *Bulletin of Materials Science*, 23(6), pp. 453-460.
- [24] Thampi, K. R., Rao, M. S., Schwarz, W., Grätzel, M., and Kiwi, J., 1988, "Preparation of SrTiO<sub>3</sub> by sol-gel techniques for the photoinduced production of H<sub>2</sub> and surface peroxides from water," *Journal of the Chemical Society, Faraday Transactions 1: Physical Chemistry in Condensed Phases*, 84(5), pp. 1703-1712.
- [25] Zeng, P., Ran, R., Chen, Z., Gu, H., Shao, Z., Diniz da Costa, J. C., and Liu, S., 2007, Significant Effects of Sintering Temperature on the Performance of La<sub>0.6</sub>Sr<sub>0.4</sub>Co<sub>0.2</sub>Fe<sub>0.8</sub>O<sub>3-δ</sub> Oxygen Selective Membranes.
- [26] Tan, X., and Li, K., 2011, "Chapter 18 Engineering Aspects of MIEC Hollow Fiber Membranes for Oxygen Production," *Membrane Engineering for the Treatment of Gases: Volume 2: Gas-separation Problems Combined with Membrane Reactors*, The Royal Society of Chemistry, pp. 253-278.

- [27] Xu, S. J., and Thomson, W. J., 1999, "Oxygen permeation rates through ion-conducting perovskite membranes," *Chemical Engineering Science*, 54(17), pp. 3839-3850.
- [28] Wagner, C., 1975, "Equations for transport in solid oxides and sulfides of transition metals," *Progress in Solid State Chemistry*, 10, pp. 3-16.
- [29] Luo, H., Jiang, H., Klande, T., Cao, Z., Liang, F., Wang, H., and Caro, J., 2012, "Novel Cobalt-Free, Noble Metal-Free Oxygen-Permeable  $40\text{Pr}_{0.6}\text{Sr}_{0.4}\text{FeO}_{3-\delta}-60\text{Ce}_{0.9}\text{Pr}_{0.1}\text{O}_{2-\delta}$  Dual-Phase Membrane," *Chemistry of Materials*, 24(11), pp. 2148-2154.
- [30] Calès, B., and F. Baumard, J., 1984, Mixed Conduction and Defect Structure of  $\text{ZrO}_2\text{-CeO}_2\text{-Y}_2\text{O}_3$ , Solid Solutions.
- [31] Nigara, Y., Mizusaki, J., and Ishigame, M., 1995, "Measurement of oxygen permeability in  $\text{CeO}_2$  doped CSZ," *Solid State Ionics*, 79, pp. 208-211.
- [32] Badwal, S. P. S., 1992, "Zirconia-based solid electrolytes: microstructure, stability and ionic conductivity," *Solid State Ionics*, 52(1), pp. 23-32.
- [33] Kim, S., Kim, S., Lee, H., Seo, Y., Kim, B., and Lee, H., 2016, "Enhancement of ionic conductivity and thermal stability of CaO-stabilised zirconia (CSZ) with MgO addition by scavenging effects," *Advances in Applied Ceramics*, 115(8), pp. 495-498.
- [34] Kharton, V. V., Yaremchenko, A. A., Kovalevsky, A. V., Viskup, A. P., Naumovich, E. N., and Kerko, P. F., 1999, "Perovskite-type oxides for high-temperature oxygen separation membranes," *Journal of Membrane Science*, 163(2), pp. 307-317.
- [35] Malavasi, L., Fisher, C. A. J., and Islam, M. S., 2010, "Oxide-ion and proton conducting electrolyte materials for clean energy applications: structural and mechanistic features," *Chemical Society Reviews*, 39(11), pp. 4370-4387.

- [36] Zeng, Y., Lin, Y. S., and Swartz, S. L., 1998, "Perovskite-type ceramic membrane: synthesis, oxygen permeation and membrane reactor performance for oxidative coupling of methane," *Journal of Membrane Science*, 150(1), pp. 87-98.
- [37] Zhang, K., Sunarso, J., Shao, Z., Zhou, W., Sun, C., Wang, S., and Liu, S., 2011, "Research progress and materials selection guidelines on mixed conducting perovskite-type ceramic membranes for oxygen production," *RSC Advances*, 1(9), pp. 1661-1676.
- [38] Bouwmeester, H. J. M., and Burggraaf, A. J., 1996, "Chapter 10 Dense ceramic membranes for oxygen separation," *Membrane Science and Technology*, A. J. Burggraaf, and L. Cot, eds., Elsevier, pp. 435-528.
- [39] Fossdal, A., Menon, M., Wærnhus, I., Wiik, K., Einarsrud, M.-A., and Grande, T., 2004, "Crystal Structure and Thermal Expansion of  $\text{La}_{1-x}\text{Sr}_x\text{FeO}_{3-\delta}$  Materials," *Journal of the American Ceramic Society*, 87(10), pp. 1952-1958.
- [40] Bouwmeester, H. J. M., Kruidhof, H., and Burggraaf, A. J., 1994, "Importance of the surface exchange kinetics as rate limiting step in oxygen permeation through mixed-conducting oxides," *Solid State Ionics*, 72, pp. 185-194.
- [41] Han, N., Meng, B., Yang, N., Sunarso, J., Zhu, Z., and Liu, S., 2018, "Enhancement of oxygen permeation fluxes of  $\text{La}_{0.6}\text{Sr}_{0.4}\text{CoO}_{3-\delta}$  hollow fiber membrane via macrostructure modification and  $(\text{La}_{0.5}\text{Sr}_{0.5})_2\text{CoO}_4$  decoration," *Chemical Engineering Research and Design*, 134, pp. 487-496.
- [42] Yang, D., Yang, N., Meng, B., Tan, X., Zhang, C., Sunarso, J., Zhu, Z., and Liu, S., 2017, "A-Site Excess  $(\text{La}_{0.8}\text{Ca}_{0.2})_{1.01}\text{FeO}_{3-\delta}$  (LCF) Perovskite Hollow Fiber Membrane for Oxygen Permeation in  $\text{CO}_2$ -Containing Atmosphere," *Energy & Fuels*, 31(4), pp. 4531-4538.

- [43] Zhang, Y., Yuan, R.-h., He, Z.-y., Gao, J.-f., and Chen, C.-s., 2016, "Phase inversion tape casting and oxygen permeation properties of supported planar  $\text{Zr}_{0.84}\text{Y}_{0.16}\text{O}_{1.92}-\text{La}_{0.8}\text{Sr}_{0.2}\text{Cr}_{0.5}\text{Fe}_{0.5}\text{O}_{3-\delta}$  composite membrane," *Solid State Ionics*, 288, pp. 342-346.
- [44] Unger, L.-S., Meffert, M., Wilde, V., Störmer, H., Niedrig, C., Menesklou, W., Wagner, S. F., Gerthsen, D., and Ivers-Tiffée, E., 2016, "Influence of a  $\text{La}_{0.6}\text{Sr}_{0.4}\text{CoO}_{3-\delta}$  Functional Layer on  $(\text{Ba}_{0.5}\text{Sr}_{0.5})(\text{Co}_{0.8}\text{Fe}_{0.2})\text{O}_{3-\delta}$  Oxygen Transport Membranes (OTMs)," *ECS Transactions*, 72(7), pp. 37-45.
- [45] Kwon, Y.-i., Na, B. T., Park, J. H., Yun, K. S., Hong, S. K., Yu, J. H., and Joo, J. H., 2017, "Guidelines for selecting coating materials for a high oxygen permeation flux in a fluorite-rich dual-phase membrane," *Journal of Membrane Science*, 535, pp. 200-207.
- [46] Han, N., Zhang, S., Meng, X., Yang, N., Meng, B., Tan, X., and Liu, S., 2016, "Effect of enhanced oxygen reduction activity on oxygen permeation of  $\text{La}_{0.6}\text{Sr}_{0.4}\text{Co}_{0.2}\text{Fe}_{0.8}\text{O}_{3-\delta}$  membrane decorated by  $\text{K}_2\text{NiF}_4$ -type oxide," *Journal of Alloys and Compounds*, 654, pp. 280-289.
- [47] Pfaff, E. M., Kaletsch, A., and Broeckmann, C., 2012, "Design of a Mixed Ionic/Electronic Conducting Oxygen Transport Membrane Pilot Module," *Chemical Engineering & Technology*, 35(3), pp. 455-463.
- [48] Chen, Y., Qian, B., Li, S., Jiao, Y., Tade, M. O., and Shao, Z., 2014, "The influence of impurity ions on the permeation and oxygen reduction properties of  $\text{Ba}_{0.5}\text{Sr}_{0.5}\text{Co}_{0.8}\text{Fe}_{0.2}\text{O}_{3-\delta}$  perovskite," *Journal of Membrane Science*, 449, pp. 86-96.
- [49] Gao, D., Zhao, J., Zhou, W., Ran, R., and Shao, Z., 2011, "Influence of high-energy ball milling of the starting powder on the sintering; microstructure and oxygen permeability of  $\text{Ba}_{0.5}\text{Sr}_{0.5}\text{Co}_{0.5}\text{Fe}_{0.5}\text{O}_{3-\delta}$  membranes," *Journal of Membrane Science*, 366(1), pp. 203-211.

- [50] Ishihara, T., Tabuchi, J., Ishikawa, S., Yan, J., Enoki, M., and Matsumoto, H., 2006, "Recent progress in LaGaO<sub>3</sub> based solid electrolyte for intermediate temperature SOFCs," *Solid State Ionics*, 177(19), pp. 1949-1953.
- [51] Atkinson, A., Barnett, S., Gorte, R. J., Irvine, J. T. S., McEvoy, A. J., Mogensen, M., Singhal, S. C., and Vohs, J., 2004, "Advanced anodes for high-temperature fuel cells," *Nature Materials*, 3, p. 17.
- [52] Ellis, M. W., Spakovsky, M. R. V., and Nelson, D. J., 2001, "Fuel cell systems: efficient, flexible energy conversion for the 21st century," *Proceedings of the IEEE*, 89(12), pp. 1808-1818.
- [53] Singhal, S. C., 2000, "Advances in solid oxide fuel cell technology," *Solid State Ionics*, 135(1), pp. 305-313.
- [54] "Ceramic Membrane Reactors," *Ceramic Membranes for Separation and Reaction*.
- [55] Wang, H., Cong, Y., and Yang, W., 2003, "Investigation on the partial oxidation of methane to syngas in a tubular Ba<sub>0.5</sub>Sr<sub>0.5</sub>Co<sub>0.8</sub>Fe<sub>0.2</sub>O<sub>3-δ</sub> membrane reactor," *Catalysis Today*, 82(1), pp. 157-166.
- [56] Gallucci, F., Comite, A., Capannelli, G., and Basile, A., 2006, "Steam Reforming of Methane in a Membrane Reactor: An Industrial Case Study," *Industrial & Engineering Chemistry Research*, 45(9), pp. 2994-3000.
- [57] Slade, D. A., Duncan, A. M., Nordheden, K. J., and Stagg-Williams, S. M., 2007, "Mixed-conducting oxygen permeable ceramic membranes for the carbon dioxide reforming of methane," *Green Chemistry*, 9(6), pp. 577-581.
- [58] Zhu, W., Han, W., Xiong, G., and Yang, W., 2005, "Mixed reforming of heptane to syngas in the Ba<sub>0.5</sub>Sr<sub>0.5</sub>Co<sub>0.8</sub>Fe<sub>0.2</sub>O<sub>3</sub> membrane reactor," *Catalysis Today*, 104(2), pp. 149-153.

- [59] Akin, F. T., and Lin, Y. S., 2002, "Oxidative coupling of methane in dense ceramic membrane reactor with high yields," *AIChE Journal*, 48(10), pp. 2298-2306.
- [60] Lobera, M. P., Escolástico, S., and Serra, J. M., 2011, "High Ethylene Production through Oxidative Dehydrogenation of Ethane Membrane Reactors Based on Fast Oxygen-Ion Conductors," *ChemCatChem*, 3(9), pp. 1503-1508.
- [61] Perez-Ramirez, J., and Vigeland, B., 2005, "Perovskite membranes in ammonia oxidation: towards process intensification in nitric acid manufacture," *Angew Chem Int Ed Engl*, 44(7), pp. 1112-1115.
- [62] Sun, S., Rebeilleau-Dassonneville, M., Zhu, X., Chu, W., and Yang, W., 2010, "Ammonia oxidation in  $\text{Ba}_{0.5}\text{Sr}_{0.5}\text{Co}_{0.8}\text{Fe}_{0.2}\text{O}_{3-\delta}$  membrane reactor," *Catalysis Today*, 149(1), pp. 167-171.
- [63] Balachandran, U., Lee, T. H., Wang, S., and Dorris, S. E., 2004, "Use of mixed conducting membranes to produce hydrogen by water dissociation," *International Journal of Hydrogen Energy*, 29(3), pp. 291-296.
- [64] Jiang, H., Wang, H., Werth, S., Schiestel, T., and Caro, J., 2008, "Simultaneous Production of Hydrogen and Synthesis Gas by Combining Water Splitting with Partial Oxidation of Methane in a Hollow-Fiber Membrane Reactor," *Angewandte Chemie International Edition*, 47(48), pp. 9341-9344.
- [65] Jiang, H., Wang, H., Liang, F., Werth, S., Schirrmeister, S., Schiestel, T., and Caro, J., 2010, "Improved water dissociation and nitrous oxide decomposition by in situ oxygen removal in perovskite catalytic membrane reactor," *Catalysis Today*, 156(3), pp. 187-190.
- [66] !!! INVALID CITATION !!! [66].

- [67] Jin, W., Zhang, C., Zhang, P., Fan, Y., and Xu, N., 2006, "Thermal decomposition of carbon dioxide coupled with POM in a membrane reactor," *AIChE Journal*, 52(7), pp. 2545-2550.
- [68] Jiang, H., Xing, L., Czuprat, O., Wang, H., Schirrmeister, S., Schiestel, T., and Caro, J., 2009, "Highly effective NO decomposition by in situ removal of inhibitor oxygen using an oxygen transporting membrane," *Chem Commun (Camb)*(44), pp. 6738-6740.
- [69] Hashim, S. S., Mohamed, A. R., and Bhatia, S., 2011, "Oxygen separation from air using ceramic-based membrane technology for sustainable fuel production and power generation," *Renewable and Sustainable Energy Reviews*, 15(2), pp. 1284-1293.
- [70] Davison, J., 2007, "Performance and costs of power plants with capture and storage of CO<sub>2</sub>," *Energy*, 32(7), pp. 1163-1176.
- [71] L. Ochs, T., A. Summers, C., Gerdemann, S., Oryshchyn, D., Turner, P., and Patrick, B., 2011, "Integrated capture of fossil fuel gas pollutants including CO<sub>2</sub> with energy recovery."
- [72] Stadler, H., Beggel, F., Habermehl, M., Persigehl, B., Kneer, R., Modigell, M., and Jeschke, P., 2011, "Oxyfuel coal combustion by efficient integration of oxygen transport membranes," *International Journal of Greenhouse Gas Control*, 5(1), pp. 7-15.
- [73] Kneer, R., Toporov, D., Förster, M., Christ, D., Broeckmann, C., Pfaff, E., Zwick, M., Engels, S., and Modigell, M., 2010, "OXYCOAL-AC: Towards an integrated coal-fired power plant process with ion transport membrane-based oxygen supply," *Energy & Environmental Science*, 3(2), pp. 198-207.
- [74] Wilson, J., Christie, M., Degenstein, N., Shah, M., and Li, J., 2019, OTM Based Oxy-fuel Combustion for CO<sub>2</sub> Capture.

- [75] Engels, S., Beggel, F., Modigell, M., and Stadler, H., 2010, "Simulation of a membrane unit for oxyfuel power plants under consideration of realistic BSCF membrane properties," *Journal of Membrane Science*, 359(1), pp. 93-101.
- [76] Exter, M. J., Haije, W., and F. Vente, J., 2009, *Viability of ITM Technology for Oxygen Production and Oxidation Processes: Material, System, and Process Aspects*.
- [77] 2005, "Advanced Zero Emissions Gas Turbine Power Plant," *Journal of Engineering for Gas Turbines and Power*, 127(1), pp. 81-85.
- [78] Fredriksson Möller, B., Torisson, T., Assadi, M., Gunnar Sundkvist, S., Mats, S., Ake, K., Ingvar Asen, K., and Kjersti, W., 2006, *AZEP Gas Turbine Combined Cycle Power Plants - Thermo-economic Analysis*.
- [79] Kirsten, F., and Evgeny, Y., 2006, *History and State-of-the-Art of Fuel Fired Zero Emission Power Cycles*.
- [80] Yantovski, E., Gorski, J., Smyth, B., and ten Elshof, J., 2004, "Zero-emission fuel-fired power plants with ion transport membrane," *Energy*, 29(12), pp. 2077-2088.
- [81] Han, L., Deng, G., Li, Z., Fan, Y., Zhang, H., Wang, Q., and Iilejeji, K. E., 2018, "Simulation and optimization of ion transfer membrane air separation unit in an IGCC power plant," *Applied Thermal Engineering*, 129, pp. 1478-1487.
- [82] Hu, J., V. Galvita, V., Poelman, H., and B. Marin, G., 2018, *Advanced Chemical Looping Materials for CO<sub>2</sub> Utilization: A Review*.
- [83] Adanez, J., Abad, A., Garcia-Labiano, F., Gayan, P., and de Diego, L. F., 2012, "Progress in Chemical-Looping Combustion and Reforming technologies," *Progress in Energy and Combustion Science*, 38(2), pp. 215-282.

- [84] Wang, P., Means, N., Shekhawat, D., Berry, D., and Massoudi, M., 2015, "Chemical-Looping Combustion and Gasification of Coals and Oxygen Carrier Development: A Brief Review."
- [85] Ishida, M., and Jin, H., 1994, "A novel combustor based on chemical-looping reactions and its reaction kinetics," *Journal of chemical engineering of Japan*, 27(3), pp. 296-301.
- [86] Ishida, M., and Jin, H., 1996, "A Novel Chemical-Looping Combustor without NO<sub>x</sub> Formation," *Industrial & Engineering Chemistry Research*, 35(7), pp. 2469-2472.
- [87] Cabello, A., Gayán, P., García-Labiano, F., de Diego, L. F., Abad, A., Izquierdo, M. T., and Adánez, J., 2014, "Relevance of the catalytic activity on the performance of a NiO/CaAl<sub>2</sub>O<sub>4</sub> oxygen carrier in a CLC process," *Applied Catalysis B: Environmental*, 147, pp. 980-987.
- [88] Johansson, E., Mattisson, T., Lyngfelt, A., and Thunman, H., 2006, "A 300W laboratory reactor system for chemical-looping combustion with particle circulation," *Fuel*, 85(10), pp. 1428-1438.
- [89] Johansson, E., Mattisson, T., Lyngfelt, A., and Thunman, H., 2006, "Combustion of Syngas and Natural Gas in a 300 W Chemical-Looping Combustor," *Chemical Engineering Research and Design*, 84(9), pp. 819-827.
- [90] Cao, Y., Casenas, B., and Pan, W.-P., 2006, "Investigation of Chemical Looping Combustion by Solid Fuels. 2. Redox Reaction Kinetics and Product Characterization with Coal, Biomass, and Solid Waste as Solid Fuels and CuO as an Oxygen Carrier," *Energy & Fuels*, 20(5), pp. 1845-1854.
- [91] de Diego, L. F., García-Labiano, F., Adánez, J., Gayán, P., Abad, A., Corbella, B. M., and María Palacios, J., 2004, "Development of Cu-based oxygen carriers for chemical-looping combustion," *Fuel*, 83(13), pp. 1749-1757.

- [92] Chuang, S. Y., Dennis, J. S., Hayhurst, A. N., and Scott, S. A., 2008, "Development and performance of Cu-based oxygen carriers for chemical-looping combustion," *Combustion and Flame*, 154(1), pp. 109-121.
- [93] Siriwardane, R., Tian, H., Richards, G., Simonyi, T., and Poston, J., 2009, "Chemical-looping combustion of coal with metal oxide oxygen carriers."
- [94] Roux, S., Bensakhria, A., and Antonini, G., 2006, "Study and Improvement of the Regeneration of Metallic Oxides Used as Oxygen Carriers for a New Combustion Process," *International Journal of Chemical Reactor Engineering*.
- [95] Johansson, M., Mattisson, T., and Lyngfelt, A., 2006, "Investigation of Mn<sub>3</sub>O<sub>4</sub> With Stabilized ZrO<sub>2</sub> for Chemical-Looping Combustion," *Chemical Engineering Research and Design*, 84(9), pp. 807-818.
- [96] Abad, A., Adánez, J., García-Labiano, F., de Diego, L. F., Gayán, P., and Celaya, J., 2007, "Mapping of the range of operational conditions for Cu-, Fe-, and Ni-based oxygen carriers in chemical-looping combustion," *Chemical Engineering Science*, 62(1), pp. 533-549.
- [97] Abad, A., Mattisson, T., Lyngfelt, A., and Rydén, M., 2006, "Chemical-looping combustion in a 300 W continuously operating reactor system using a manganese-based oxygen carrier," *Fuel*, 85(9), pp. 1174-1185.
- [98] Adánez, J., de Diego, L. F., García-Labiano, F., Gayán, P., Abad, A., and Palacios, J. M., 2004, "Selection of Oxygen Carriers for Chemical-Looping Combustion," *Energy & Fuels*, 18(2), pp. 371-377.
- [99] Mattisson, T., Järnäs, A., and Lyngfelt, A., 2003, "Reactivity of Some Metal Oxides Supported on Alumina with Alternating Methane and Oxygen Application for Chemical-Looping Combustion," *Energy & Fuels*, 17(3), pp. 643-651.

- [100] Zafar, Q., Mattisson, T., and Gevert, B., 2006, "Redox Investigation of Some Oxides of Transition-State Metals Ni, Cu, Fe, and Mn Supported on SiO<sub>2</sub> and MgAl<sub>2</sub>O<sub>4</sub>," *Energy & Fuels*, 20(1), pp. 34-44.
- [101] Jin, H., Okamoto, T., and Ishida, M., 1998, "Development of a Novel Chemical-Looping Combustion: Synthesis of a Looping Material with a Double Metal Oxide of CoO–NiO," *Energy & Fuels*, 12(6), pp. 1272-1277.
- [102] Zhao, X., Zhou, H., Sikarwar, V. S., Zhao, M., Park, A.-H. A., Fennell, P. S., Shen, L., and Fan, L.-S., 2017, "Biomass-based chemical looping technologies: the good, the bad and the future," *Energy & Environmental Science*, 10(9), pp. 1885-1910.
- [103] Cho, P., Mattisson, T., and Lyngfelt, A., 2005, "Carbon Formation on Nickel and Iron Oxide-Containing Oxygen Carriers for Chemical-Looping Combustion," *Industrial & Engineering Chemistry Research*, 44(4), pp. 668-676.
- [104] Galvita, V. V., Poelman, H., Bliznuk, V., Detavernier, C., and Marin, G. B., 2013, "CeO<sub>2</sub>-Modified Fe<sub>2</sub>O<sub>3</sub> for CO<sub>2</sub> Utilization via Chemical Looping," *Industrial & Engineering Chemistry Research*, 52(25), pp. 8416-8426.
- [105] Jerndal, E., Mattisson, T., and Lyngfelt, A., 2006, "Thermal Analysis of Chemical-Looping Combustion," *Chemical Engineering Research and Design*, 84(9), pp. 795-806.
- [106] Lambert, A., Delquié, C., Clémeneçon, I., Comte, E., Lefebvre, V., Rousseau, J., and Durand, B., 2009, "Synthesis and characterization of bimetallic Fe/Mn oxides for chemical looping combustion," *Energy Procedia*, 1(1), pp. 375-381.
- [107] Ksepko, E., Siriwardane, R. V., Tian, H., Simonyi, T., and Sciazko, M., 2012, "Effect of H<sub>2</sub>S on Chemical Looping Combustion of Coal-Derived Synthesis Gas over Fe–Mn Oxides Supported on Sepiolite, ZrO<sub>2</sub>, and Al<sub>2</sub>O<sub>3</sub>," *Energy & Fuels*, 26(4), pp. 2461-2472.

- [108] Shulman, A., Cleverstam, E., Mattisson, T., and Lyngfelt, A., 2009, "Manganese/Iron, Manganese/Nickel, and Manganese/Silicon Oxides Used in Chemical-Looping With Oxygen Uncoupling (CLOU) for Combustion of Methane," *Energy & Fuels*, 23(10), pp. 5269-5275.
- [109] Rydén, M., Lyngfelt, A., Mattisson, T., Chen, D., Holmen, A., and Bjørgum, E., 2008, "Novel oxygen-carrier materials for chemical-looping combustion and chemical-looping reforming;  $LaxSr_{1-x}FeyCo_{1-y}O_{3-\delta}$  perovskites and mixed-metal oxides of NiO, Fe<sub>2</sub>O<sub>3</sub> and Mn<sub>3</sub>O<sub>4</sub>," *International Journal of Greenhouse Gas Control*, 2(1), pp. 21-36.
- [110] Howe, P., and Watts, P., 2005, "Tin and Inorganic Tin Compounds," World Health Organization.
- [111] Sarafraz, M. M., Jafarian, M., Arjomandi, M., and Nathan, G. J., 2017, "The relative performance of alternative oxygen carriers for liquid chemical looping combustion and gasification," *International Journal of Hydrogen Energy*, 42(26), pp. 16396-16407.
- [112] Patnaik, P., 2003, "Handbook of inorganic chemicals."
- [113] Xu, X., Zhou, W., and Zhu, Z., 2013, "Samaria-Doped Ceria Electrolyte Supported Direct Carbon Fuel Cell with Molten Antimony as the Anode," *Industrial & Engineering Chemistry Research*, 52(50), pp. 17927-17933.
- [114] Jayakumar, A., Küngas, R., Roy, S., Javadekar, A., Buttrey, D. J., Vohs, J. M., and Gorte, R. J., 2011, "A direct carbon fuel cell with a molten antimony anode," *Energy & Environmental Science*, 4(10).
- [115] Cao, D., Sun, Y., and Wang, G., 2007, "Direct carbon fuel cell: Fundamentals and recent developments," *Journal of Power Sources*, 167(2), pp. 250-257.

- [116] Cantero-Tubilla, B., Xu, C., Zondlo, J. W., Sabolsky, K., and Sabolsky, E. M., 2013, "Investigation of anode configurations and fuel mixtures on the performance of direct carbon fuel cells (DCFCs)," *Journal of Power Sources*, 238, pp. 227-235.
- [117] Cao, T., Shi, Y., Wang, H., and Cai, N., 2015, "Numerical simulation and experimental characterization of the performance evolution of a liquid antimony anode fuel cell," *Journal of Power Sources*, 284, pp. 536-546.
- [118] Duan, N.-Q., Tan, Y., Yan, D., Jia, L., Chi, B., Pu, J., and Li, J., 2016, "Biomass carbon fueled tubular solid oxide fuel cells with molten antimony anode," *Applied Energy*, 165, pp. 983-989.
- [119] Rose, J. W., Cooper, J. R., and Spiers, H. M., 1977, *Technical data on fuel*, British National Committee, World Energy Conference Edinburgh : Distributed by Scottish Academic Press, London.
- [120] Peters, A. A. F., and Weber, R., 1995, "Mathematical Modeling of a 2. 25 MWt Swirling Natural Gas Flame. Part 1: Eddy Break-up Concept for Turbulent Combustion; Probability Density Function Approach for Nitric Oxide Formation," *Combustion Science and Technology*, 110-111(1), pp. 67-101.
- [121] Amano, R., and Sundén, B., 2011, "Computational fluid dynamics and heat transfer : emerging topics."
- [122] Ghobadian, A., and Vasquez, S. A., 2007, "A General Purpose Implicit Coupled Algorithm for the Solution of Eulerian Multiphase Transport Equation," *Multiphase FlowGermany*.
- [123] 2011, ANSYS FLUENT Theory Guide.

[124] Hamers, H., Romano, M., Spallina, V., Chiesa, P., Gallucci, F., and van Sint Annaland, M., 2015, "Energy analysis of two stage packed-bed chemical looping combustion configurations for integrated gasification combined cycles," *Energy*, 85, pp. 489-502.

[125] !!! INVALID CITATION !!! .

[126] "<Pilot-scale production of oxygen from air using perovskite hollow fibre membranes.pdf>."

[127] Assael, M., E. Kalyva, A., Antoniadis, K., Banish, R., Egry, I., Wu, J., Kschnitz, E., and A. Wkeham, W., 2012, *Reference Data for the Density and Viscosity of Liquid Antimony, Bismuth, Lead, Nickel and Silver*.

## APPENDIX-A

### Nomenclature

|           |                                                |
|-----------|------------------------------------------------|
| $A$       | Area ( $m^2$ )                                 |
| $a$       | Absorption coefficient                         |
| ASU       | Air separation unit                            |
| AZEP      | Advance zero emissions gas turbine power plant |
| $C$       | Linear-anisotropic phase function coefficient  |
| $C_D$     | Drag coefficient                               |
| $C_p$     | Specific heat (J/kg.K)                         |
| CLC       | Chemical looping combustion                    |
| CMR       | Catalytic membrane reactor                     |
| DCFC      | Direct carbon fuel cells                       |
| $d$       | diameter (m)                                   |
| $D_m$     | Mass diffusion coefficient                     |
| $D_T$     | Thermal diffusion coefficient                  |
| F         | Faraday's constant (C/mol)                     |
| $f$       | Drag fraction                                  |
| $\vec{g}$ | Acceleration due to gravity ( $m/s^2$ )        |
| $G$       | Incident radiation                             |
| $h$       | Specific enthalpy (J/kmol)                     |
| $\bar{h}$ | Volumetric heat transfer coefficient           |
| $h^\cdot$ | Indicate electron holes                        |
| $h^o$     | Enthalpy of formation                          |
| $H$       | Heterogeneous reaction rate                    |
| IGCC      | Integrated gasification combined cycle         |
| ITM       | Ion transport membrane                         |
| $\vec{j}$ | Diffusion flux                                 |
| $J_{O_2}$ | Oxygen flux ( $mol\ s^{-1}\ cm^{-2}$ )         |
| $k$       | Thermal conductivity (w/m.k)                   |

|             |                                               |
|-------------|-----------------------------------------------|
| $\bar{K}$   | Momentum exchange coefficient                 |
| $L$         | Membrane thickness (m)                        |
| $L_c$       | Characteristic length (m)                     |
| LCLC        | Liquid chemical looping combustion            |
| $M$         | Molecular weight (kg/kmol)                    |
| MIEC        | Mixed ionic-electronic membrane               |
| $n$         | Refractive index of the medium                |
| OC          | Oxygen carrier                                |
| OCV         | Open circuit voltage (volt)                   |
| ODH         | Oxidative dehydrogenation                     |
| OCM         | Oxidative coupling of methane                 |
| OTM         | Oxygen transport membrane                     |
| $O_o^x$     | Indicate oxygen ions                          |
| POM         | Partial oxidation of methane                  |
| $P_{O_2}$   | Oxygen partial pressure (atm)                 |
| $P'_{O_2}$  | Oxygen partial pressure on rich side (atm)    |
| $P''_{O_2}$ | Oxygen partial pressure on lean side (atm)    |
| $Pr$        | Prandtl number $C_p \mu / k$                  |
| $\bar{q}$   | Heat flux ( $w/m^2$ )                         |
| $Q$         | Intensity of heat exchange between phases (w) |
| $R$         | Reaction rate ( $kmol/m^3.s$ )                |
| $\bar{R}$   | Interaction force (N)                         |
| $R^-$       | Universal gas (J/kmol.K)                      |
| $Re$        | Reynold number                                |
| $S$         | Heat source                                   |
| SOFC        | Solid oxide fuel cell                         |
| $t$         | Time (sec)                                    |
| $T$         | Temperature (K)                               |
| $\vec{v}$   | Velocity of phase (m/s)                       |

|               |                                                   |
|---------------|---------------------------------------------------|
| $V$           | Volume (m <sup>3</sup> )                          |
| $V_{\dot{O}}$ | Indicate oxygen vacancies                         |
| $X$           | Mass source                                       |
| $Y$           | Mass fraction                                     |
| ZEITMOP       | Zero emission ion transport membrane oxygen power |

### **Greek symbols**

|              |                                        |
|--------------|----------------------------------------|
| $\mu$        | Viscosity (kg/m.s)                     |
| $\tau$       | Share stress                           |
| $\sigma$     | Stefan-Boltzmann constant              |
| $\sigma_s$   | Scattering coefficient                 |
| $\sigma_i$   | Ion conductivity                       |
| $\sigma_e$   | Electronic conductivity                |
| $\alpha$     | Volume fraction                        |
| $\gamma$     | Stoichiometric coefficient             |
| $\rho$       | Density (Kg/m <sup>3</sup> )           |
| $\hat{\rho}$ | Effective density (Kg/m <sup>3</sup> ) |
| $\bar{\tau}$ | Stress-strain tensor                   |

### **Subscripts**

|      |                                          |
|------|------------------------------------------|
| $l$  | Liquid phase                             |
| $g$  | gas phase                                |
| $lg$ | Interphase between liquid and gas phases |
| $gl$ | Interphase between gas and liquid phases |
| $m$  | Mixture                                  |
| $i$  | Indicate for specie in mixture           |
| $r$  | Radiation                                |
| $c$  | Chemical                                 |
| $ri$ | Reactant of specie                       |
| $pi$ | Product of specie                        |
| $q$  | Indicate to describe a phase             |

## APPENDIX-B

### UDF

```
#include "udf.h"
#include "stdio.h"
#include "time.h"
#include "sg.h"
#include "sg_mphase.h"
#include "flow.h"
#include "mem.h"
#include "metric.h"

real mflow;
real vol_tot;
int ncells;

#define SMALL_S 1.e-29
/*#define UNIVERSAL_GAS_CONSTANT 8314.472 /*J/Kmol.K*/
/*#define rho_O2 0.3847 /*kg/m3*/
/*#define rho_CH4 0.3087 /*kg/m3*/
#define eps_g_small 0.99999
#define spe_small 1.e-8
#define TMAX 2500.

static cxboolean init_flag = TRUE;
/* Search the index for each species*/
static real mw[MAX_PHASES][MAX_SPE_EQNS];

static int INDEX_PHASE_SB = 0, INDEX_SPECIES_SB = 0, INDEX_PHASE_SB2O3 = 0,
INDEX_SPECIES_SB2O3 = 0, INDEX_PHASE_CO2 = 0, INDEX_SPECIES_CO2,

INDEX_PHASE_H2O = 0, INDEX_SPECIES_H2O = 0, INDEX_PHASE_CH4 = 0,
INDEX_SPECIES_CH4 = 0, INDEX_PHASE_O2 = 0, INDEX_SPECIES_O2 = 0;

DEFINE_ADJUST(rrr, domain)
{
    int n, ns;
```

```

Domain*subdomain;
/*int n_phases= DOMAIN_N_DOMAINS(domain);*/
if(init_flag)
{
#ifdef !RP_HOST
/*search all the species and saved the Molecular Weight*/
sub_domain_loop(subdomain,domain,n)
{
Material*m_mat,*s_mat;
if (DOMAIN_NSPE(subdomain)>0)
{
m_mat =
Pick_Material(DOMAIN_MATERIAL_NAME(subdomain),NULL);
mixture_species_loop(m_mat,s_mat,ns)
{
if (0 ==
strcmp(MIXTURE_SPECIE_NAME(m_mat,ns),"sb"))
{
INDEX_PHASE_SB = n;
INDEX_SPECIES_SB = ns;
}
else if (0 ==
strcmp(MIXTURE_SPECIE_NAME(m_mat,ns),"sb2o3"))
{
INDEX_PHASE_SB2O3 = n;
INDEX_SPECIES_SB2O3 = ns;
}
else if (0 ==
strcmp(MIXTURE_SPECIE_NAME(m_mat,ns),"co2"))
{
INDEX_PHASE_CO2 = n;

```

```

INDEX_SPECIES_CO2 = ns;
}

else if (0 == strcmp(MIXTURE_SPECIE_NAME(m_mat,
ns),"h2o"))
{
INDEX_PHASE_H2O = n;
INDEX_SPECIES_H2O = ns;
}

else if (0 == strcmp(MIXTURE_SPECIE_NAME(m_mat,
ns),"ch4"))
{
INDEX_PHASE_CH4 = n;
INDEX_SPECIES_CH4 = ns;
}

else if (0 == strcmp(MIXTURE_SPECIE_NAME(m_mat,
ns),"o2"))
{
INDEX_PHASE_O2= n;
INDEX_SPECIES_O2 = ns;
}

CX_Message("\n%d%d,%d%d,%d%d,%d%d,%d%d,%d%d,%d%d,%d%d,%d
%d%d,%d%d,%d%d,%d%d,%d%d,%d%d,%d%d,%d%d,%d%d,%d
%d%d,%d%d,%d%d\n",
INDEX_PHASE_SB, INDEX_SPECIES_SB, INDEX_PHASE_SB2O3,
INDEX_SPECIES_SB2O3, INDEX_PHASE_CO2, INDEX_SPECIES_CO2,
INDEX_PHASE_H2O, INDEX_SPECIES_H2O, INDEX_PHASE_CH4,
INDEX_SPECIES_CH4, INDEX_PHASE_O2, INDEX_SPECIES_O2);

mw[n][ns] = MATERIAL_PROP(s_mat,PROP_mwi);
}
}

else

```

```

    {
        s_mat = Pick_Material(DOMAIN_MATERIAL_NAME(subdomain),NULL);
        mw[n][0] = MATERIAL_PROP(s_mat,PROP_mwi);
    }

}

#endif

    init_flag = FALSE;
}
}
DEFINE_HET_RXN_RATE(oxidation, c, t, hr, mw, yi, rr, rr_t)
{
    Thread**pt = THREAD_SUB_THREADS(t);
    Thread*tp = pt[0]; /*Gas phase*/
    Thread*ts = pt[1]; /*Liquid phase*/
    real prod;
    real x0_star = 0, x_star = 0.;
        *rr = 0;
    prod = 0;
    {
        if (C_VOF(c, ts) <
eps_g_small&&yi[INDEX_PHASE_O2][INDEX_SPECIES_O2] > spe_small)
            {
                prod = (yi[INDEX_PHASE_O2][INDEX_SPECIES_O2] -
x_star)*0.3848/ mw[INDEX_PHASE_O2][INDEX_SPECIES_O2];/*kmol/m3*/

                *rr =1000*prod*C_VOF(c, tp);/*kmol/m3.s*/
            }
    }
}

```

```

}
DEFINE_HET_RXN_RATE(reduction, c, t, hr, mw, yi, rr, rr_t)
{
    Thread**pt = THREAD_SUB_THREADS(t);
    Thread*tp = pt[0]; /*gas phase*/
    Thread*ts = pt[1]; /*liquid phase*/
    real prod;
    real x0_star = 0, x_star = 0.;
        *rr = 0;
    prod = 0;
    {
        if (C_VOF(c, ts) <
eps_g_small&&yi[INDEX_PHASE_CH4][INDEX_SPECIES_CH4] > spe_small)
            {
                prod = (yi[INDEX_PHASE_CH4][INDEX_SPECIES_CH4] -
x_star)*0.3087 / mw[INDEX_PHASE_CH4][INDEX_SPECIES_CH4];/*kmol/m3*/
                *rr =1000*prod*C_VOF(c, tp);/*kmol/m3.s*/
            }
    }
}

```

## VITA

Graduate School

Southern Illinois University

Hussein M. Al-Mrayatee

[husseinxmsm@gmail.com](mailto:husseinxmsm@gmail.com)

Education:

B.Sc. in Mechanical Engineering, June 2000, University of Baghdad, Baghdad, Iraq.

M.Sc. in Mechanical Engineering, December 2003, University of Baghdad, Baghdad, Iraq.

Dissertation Title: Simulation of A Novel Mediated Oxycombustion System

Major Professor: Dr. Kanchan Mondal